

ADVERTIMENT. La consulta d'aquesta tesi queda condicionada a l'acceptació de les següents condicions d'ús: La difusió d'aquesta tesi per mitjà del servei TDX (www.tesisenxarxa.net) ha estat autoritzada pels titulars dels drets de propietat intel·lectual únicament per a usos privats emmarcats en activitats d'investigació i docència. No s'autoritza la seva reproducció amb finalitats de lucre ni la seva difusió i posada a disposició des d'un lloc aliè al servei TDX. No s'autoritza la presentació del seu contingut en una finestra o marc aliè a TDX (framing). Aquesta reserva de drets afecta tant al resum de presentació de la tesi com als seus continguts. En la utilització o cita de parts de la tesi és obligat indicar el nom de la persona autora.

ADVERTENCIA. La consulta de esta tesis queda condicionada a la aceptación de las siguientes condiciones de uso: La difusión de esta tesis por medio del servicio TDR (www.tesisenred.net) ha sido autorizada por los titulares de los derechos de propiedad intelectual únicamente para usos privados enmarcados en actividades de investigación y docencia. No se autoriza su reproducción con finalidades de lucro ni su difusión y puesta a disposición desde un sitio ajeno al servicio TDR. No se autoriza la presentación de su contenido en una ventana o marco ajeno a TDR (framing). Esta reserva de derechos afecta tanto al resumen de presentación de la tesis como a sus contenidos. En la utilización o cita de partes de la tesis es obligado indicar el nombre de la persona autora.

WARNING. On having consulted this thesis you're accepting the following use conditions: Spreading this thesis by the TDX (www.tesisenxarxa.net) service has been authorized by the titular of the intellectual property rights only for private uses placed in investigation and teaching activities. Reproduction with lucrative aims is not authorized neither its spreading and availability from a site foreign to the TDX service. Introducing its content in a window or frame foreign to the TDX service is not authorized (framing). This rights affect to the presentation summary of the thesis as well as to its contents. In the using or citation of parts of the thesis it's obliged to indicate the name of the author

PhD Thesis
MATERIALS SCIENCE AND ENGINEERING DOCTORAL
PROGRAM

**Effect of Doping Ions and Organic
Molecules on the Precipitation and
Biological Interactions of Nanostructured
Calcium Phosphates**

Zhitong Zhao

Supervised by:

Prof. Maria Pau Ginebra Molins

Dr. Montserrat Español Pons

**Department of Materials Science and Metallurgical Engineering
Technical University of Catalonia**

October 2015



Acta de calificación de tesis doctoral

Curso académico:

Nombre y apellidos

Programa de doctorado

Unidad estructural responsable del programa

Resolución del Tribunal

Reunido el Tribunal designado a tal efecto, el doctorando / la doctoranda expone el tema de la su tesis doctoral titulada _____

Acabada la lectura y después de dar respuesta a las cuestiones formuladas por los miembros titulares del tribunal, éste otorga la calificación:

NO APTO

APROBADO

NOTABLE

SOBRESALIENTE

(Nombre, apellidos y firma)		(Nombre, apellidos y firma)	
Presidente/a		Secretario/a	
(Nombre, apellidos y firma)	(Nombre, apellidos y firma)	(Nombre, apellidos y firma)	(Nombre, apellidos y firma)
Vocal	Vocal	Vocal	Vocal

_____, _____ de _____ de _____

El resultado del escrutinio de los votos emitidos por los miembros titulares del tribunal, efectuado por la Escuela de Doctorado, a instancia de la Comisión de Doctorado de la UPC, otorga la MENCIÓN CUM LAUDE:

SÍ

NO

(Nombre, apellidos y firma)	(Nombre, apellidos y firma)
Presidente de la Comisión Permanente de la Escuela de Doctorado	Secretario de la Comisión Permanente de la Escuela de Doctorado

Barcelona a _____ de _____ de _____

Acknowledgements

I would never have been able to finish the following dissertation without the guidance from my supervisors, help from my friends and supports from my family.

I would like to express my deepest gratitude to my supervisors Prof. Maria Pau Ginebra and Dr. Montserrat Español for their excellent guidance, caring, patience. Thank Prof. Maria Pau Ginebra for her enthusiasm which was always driving forces through my PhD career. The great knowledge and wisdom she imparted to me will be invaluable asset throughout my whole life. I am also extremely grateful to Dr. Montserrat Español for her patiently guiding me on the research and correcting my writings. I have really learned a lot from her as well as from all the corrections she made for my thesis.

I would like to thank Dr. Jordi Guillem who was always willing to help and give his best suggestions on the cell culture studies. Many thanks also sent to all the other members from BBT group for the help on my research work and the care about my life. It is a great experience to have three years working with you guys. I would never forget the time that we all spent together.

I would like to thank Chinese scholarship council to provide me with scholarship and offer me this great opportunity to study abroad and work with the outstanding researchers from outside China.

I would like to thank family. I thank my parents for them always supporting me and encouraging me with their best wishes. I also would like to thank my wife Wenqing He. She was always there cheering me up and stood by me through the good times and bad.

Abstract

From a chemical and structural point of view, hydroxyapatite (HA) is a strong candidate in biomedical applications owing to its similarity to the inorganic components of bones and teeth. HA bulk materials have been traditionally considered excellent candidates as synthetic substitutes of hard tissues due to their excellent biocompatibility, osteoconductivity, and bioactivity. In addition, HA nanoparticles (NPs) as colloidal suspensions are becoming a popular tool in biomedical applications such as gene/drug delivery, bio-imaging *etc.* One aspect of particular interest when working with apatite is their capacity to incorporate foreign ions in their crystal structure. Although it is widely acknowledged that ionic substitutions on bulk HA substrates have a strong impact on their biological performance, little is known of their effect on NPs with potential use in gene transfection or drug delivery. The chapters 3 and 4 of the thesis are devoted to the effect of ion doping in HA NPs on their physicochemical characteristics as well on the interaction of NPs with cells *in vitro*.

In chapter 3 carbonate (CO_3) and magnesium (Mg) ions, which are the major substitutions in biological apatite, have been explored in the synthesis of ion-doped HA NPs under similar reaction conditions to allow comparison of results. CO_3 and Mg ion were incorporated in the crystal lattice of hydroxyapatite and caused various changes mainly in the morphology and solubility of the different nanoparticles. In addition, the impact of ion doping on the interaction of HA NPs with cells was also evaluated under various cell culture conditions: 1) performing the cell culture study on citrate-dispersed NPs and on agglomerated NPs, 2) adding/excluding 10 % of foetal bovine serum (FBS) in the cell culture media and 3) using different types of cells, i.e. osteosarcoma MG-63 cells versus rat mesenchymal stem cells (rMSCs). The *in vitro* results indicated that Mg-doped HA NPs induced a profound impact on MG63 cells and, in the absence of citrate and

FBS these nanoparticles were clearly cytotoxic. However, Mg-doped HA NPs did not alter cell viability in rMSCs under the same conditions. Moreover, it was also found that the negative surface charge conferred by citrate and protein adsorption on the NPs prevented cellular internalization of NPs on MG63, but this effect was less critical for rMSCs.

In chapter 4, Sr, Zn, Si and Fe(III) ions, which are minor ionic substitutions in biological apatite, were introduced to synthesize additional ion-doped HA NPs. Physicochemical characterization demonstrated that as-synthesized NPs were phase pure and doped ions had little influence on the morphology of NPs as in all cases they kept needle-like structure. Moreover, the solubility of Sr-doped and Si-doped HA increased while the solubility of Zn-doped and Fe-doped HA NPs decreased with ion addition. Cytotoxicity studies performed using MG63 and rMSCs cells under the conditions of serum-containing and serum-free indicated that all NPs were non-cytotoxic if FBS was present. Interestingly, Zn-doped and Fe-doped HA NPs clearly stimulated MG63 cell proliferation in the absence of FBS. In addition, Zn-doped HA NPs with low NP doses (<250 µg/ml) were also found to enhance the proliferation of rMSCs cells even in the presence of serum. As a summary, doping ions in HA NPs can be exploited as a simple but powerful tool to tune the cell behavior.

In addition to exploring the effect of ion-doped HA NPs on cell behavior, it was also the interest of this thesis to investigate calcium phosphate (CaP) mineralization in the presence of organic molecules and also doping ions. This topic is of fundamental interest in understanding how nature designs its own materials and is today the focus of extensive research. Recent investigations in the group had already proved the feasibility of forming calcium phosphate neuron-like structures with the help of simple organic molecules. In the fifth chapter of this thesis the effect of various organic molecules on CaP precipitation is provided. As shown by transmission electron microscopic studies (TEM) neuron-like structured CaP could be created using organic molecules of diverse nature such as non-ionic surfactant (Tween 80), anionic polymers (sodium polyacrylate) and cationic polymers (polydiallyldimethylammonium chloride). TEM studies through EELS, EFTEM and

SAED proved that the neuron-like structures consisting of a dense core and thin filaments surrounding it had calcium, phosphorous and oxygen evenly distributed throughout the dense core as well as the filaments, and were amorphous in nature.

Additionally, the co-effect of inorganic additives (i.e. Mg and Sr) together with organic molecules on CaP was also evaluated. It was proved that the addition of small amounts of ions had diverse impact on the stability of the neuron-like structures Mg clearly disrupting them but not Sr. All the findings with organic molecules provide much inspiration not only for the synthesis of more advanced CaP materials with novel structures and useful properties, but also for a better understanding of biomineralization process in nature.

Resumen

Desde el punto de vista químico y estructural la hidroxiapatita se considera un gran candidato para aplicaciones biomédicas por su similitud con la fase mineral del hueso y los dientes. Los sustratos/andamios de hidroxiapatita representan pues un excelente sustituto del tejido óseo por su biocompatibilidad, osteoconductividad y bioactividad. Adicionalmente, la hidroxiapatita en forma de suspensión coloidal está emergiendo con fuerza en aplicaciones como la terapia génica, liberación de fármacos, y en aplicaciones para marcaje/visualización, etc. Un aspecto a destacar, intrínseco a la apatita, es su capacidad de incorporar diferentes iones en su estructura. Aunque el efecto del dopaje se ha investigado con detalle en la fabricación de implantes viéndose que su presencia tiene un gran impacto en el comportamiento celular, poco se sabe de su efecto en nanopartículas para su uso en terapia génica y liberación de fármacos. Los dos primeros capítulos abordan precisamente el efecto del dopaje en las propiedades físico-químicas de las nanopartículas así como el efecto de dichas NPs en cultivos celulares in vitro.

En concreto, el tercer capítulo se centra en el dopaje de la apatita con iones carbonato (CO_3) y magnesio (Mg) por ser éstas las sustituciones más importantes en la apatita biológica. Para ello todas las reacciones de síntesis se realizan bajo las mismas condiciones con la finalidad de poder comparar resultados. Los resultados muestran que ambas sustituciones acaban incorporando los iones dentro de la estructura del cristal causando diferentes impactos principalmente a nivel de morfología y solubilidad. Con respecto al impacto del dopaje en la caracterización celular, se llevaron a cabo diferentes ensayos: 1) utilizando suspensiones dispersadas con citrato o sin él, 2) en medio de cultivo con o sin 10 % v/v de suero fetal bovino y 3) utilizando dos tipos de células diferentes, células de osteosarcoma (MG63) y células de rata mesenquimales (rMSCs). Los resultados in vitro mostraron que las nanopartículas dopadas con Mg eran claramente citotóxicas a las células MG63 en ausencia de FBS. Sin embargo, las mismas NPs no alteraron la viabilidad celular en rMSCs bajo las mismas condiciones. Se observó además que la carga negativa superficial que confiere la adsorción de citrato y de proteínas

sobre las NPs evitó su internalización en MG63. Para las rMSCs el efecto de la carga negativa no resultó ser tan crítico.

El capítulo cuarto se centra en la síntesis y caracterización de NPs dopadas con iones Sr, Zn, Si y Fe(III), que representan sustituciones minoritarias en la apatita biológica. Su caracterización fisicoquímica mostró que todas las NPs eran puras con morfología acicular. Respecto a su solubilidad, se observó un aumento en la solubilidad con la cantidad de ion dopante para los iones Sr y Si, y el efecto contrario para las NPs dopadas con Zn y Fe. Los estudios de citotoxicidad con células MG63 y rMSCs, con y sin FBS, mostraron viabilidad en presencia de FBS para todas las NPs. Además, para las NPs dopadas con Zn y Fe se observó un aumento notable en la proliferación celular para las MG63 cultivadas sin FBS. Este efecto también se observó en células rMSCs con NPs dopadas con Zn (dosis por debajo de $<250 \mu\text{g/ml}$) incluso en presencia de serum. En resumen, el dopaje de la HA con diferentes iones es una herramienta sencilla y a la vez potente que permite modular el comportamiento celular.

Además de explorar el efecto del dopaje de iones en NP de HA, otro campo de interés en esta tesis ha sido investigar la mineralización de fosfatos de calcio (CaP) en presencia de moléculas orgánicas y de diferentes iones. Este tema es crucial para entender cómo la naturaleza diseña sus propios materiales y es hoy un gran campo de investigación. A través de estudios recientes en el grupo de investigación se ha visto que es posible formar fosfatos de calcio con estructura neuronal con la ayuda de simples moléculas orgánicas. En el quinto capítulo de esta tesis se estudia el efecto de varias moléculas orgánicas en la precipitación de CaP. Estudios por microscopía electrónica de transmisión (TEM) revelaron la presencia de estas estructuras neuronales formadas con la ayuda de moléculas orgánicas de diferente naturaleza: surfactante no iónicos (Tween 80), polímeros aniónicos (poliacrilato sódico) y polímeros catiónicos (cloruro de polidialildimetilamonio). Varios estudios por TEM como son EELS, EFTEM y SAED permitieron establecer que las estructuras neuronales consistían de un núcleo denso del cual se extendía una red de filamentos, que en estas estructuras el calcio, fósforo y oxígeno estaba homogéneamente distribuido y que eran de naturaleza amorfa.

Además se investigó el efecto simultáneo de añadir aditivos inorgánicos (iones Mg i Sr) junto con moléculas orgánicas. Se observó que la adición de pequeñas cantidades de iones afectaba la estabilidad de las estructuras neuronales. Con Mg las estructuras no eran estables pero sí con Sr. Estos estudios pueden ser fuente no sólo de inspiración en la síntesis de estructuras más avanzadas y con propiedades notablemente diferentes, sino que además proporcionan un mejor conocimiento de los procesos de biomineralización.

Publications

1. M. Español, **Z. Zhao**, J. Guillem-Marti, D. Kempf, A. Diez-Escudero and M.-P. Ginebra. Ion-doping as a strategy to modulate hydroxyapatite nanoparticle internalization. (Nanoscale, submitted, co-first author).
2. M. Español, **Z. Zhao**, J. Almunia and M.-P. Ginebra. Calcium phosphate neuron-like structures: a rare case or a common structure?. *J. Mater. Chem. B*, 2014, 2, 2020-2029.

Conferences participation

1. **Z. Zhao**, M. Español, M.P. Ginebra. Amorphous calcium phosphate (ACP): a Curse or a Blessing? Oral presentation at the Summer School held in Barcelona (Universitat Politècnica de Catalunya) and organized under the STINT Program. 10-12th June, 2013.
2. **Z. Zhao**, M. Español, M.P. Ginebra. Preparation and characterization of Sr, Zn, Si and Fe-doped hydroxyapatite nanoparticles. 26th Annual Conference of the European Society for Biomaterials (ESB 2014) August 31-September 3, Liverpool (poster presentation).
3. M. Español, **Z. Zhao**, D. Kempft, J. Guillem-Marti, M.P. Ginebra. Cytotoxicity of Mg-and carbonate-doped hydroxyapatite nanoparticles. 26th Bioceramics, Barcelona November 6-8, 2014. (Oral presentation, presenter)
4. **Z. Zhao**, M. Español, M.P. Ginebra. Ion-doped Hydroxyapatite Nanoparticles as Potential Vectors in Gene Therapy. 27th European Conference on Biomaterials ESB2015, August 30-September 3, Krakow, Poland. (Oral presentation)

Table of contents

Acknowledgements.....	I
Abstract.....	III
Resumen.....	VI
Publications.....	XI
Conferences participation	XI
Chapter 1 Objectives and structure of the thesis.....	1
1.1 Motivations	1
1.2 Overall objectives	2
1.3 Structure of thesis.....	4
1.4 Reference.....	5
Chapter 2 State of the art	7
2.1 Calcium phosphates: hydroxyapatite	7
2.1.1 Composition of structure of hydroxyapatite.....	9
2.1.2 Biological apatite	11
2.2 The potential of hydroxyapatite nanoparticles in biomedical applications. 14	
2.2.1 Gene delivery.....	16
2.2.2 Bio-imaging.....	20
2.2.3 Cancer therapy	21
2.3 Synthesis of hydroxyapatite nanoparticles	22
2.3.1 Wet chemical precipitation	24
2.3.2 Hydrothermal treatment	26
2.3.3 Micro-emulsion synthesis.....	26
2.4 Biomineralization	28
2.4.1 Crystal growth in biomineralization processes.....	31
2.4.2 Organic molecules in CaP mineralization.....	35
2.5 References.....	41

Chapter 3

Effect of Major Ions in Hydroxyapatite Nanoparticles: Magnesium and Carbonate .. 61

3.1 Introduction..... 61

3.2 Objectives 63

3.3 Materials and Methods 65

 3.3.1 Synthesis of ion-doped HA nanoparticles..... 65

 3.3.2 Characterization of ion-doped HA nanoparticles..... 66

 3.3.3 Preparation and characterization of nanoparticles 67

 suspension 67

 3.3.4 *In vitro* cell culture studies 68

3.4 Results and discussion..... 71

 3.4.1 Effect of ion doping on physicochemical properties 71

 3.4.2 Dispersion behavior and surface charge of the various ion doped NPs
..... 77

 3.4.3 Effect of ion doping on cell behavior..... 77

3.5 Conclusions 87

3.6 References..... 88

Chapter 4

**Effect of minority ions doping in HA nanoparticles: Strontium, Zinc, Silicon and Iron
..... 95**

4.1 Introduction..... 95

4.2 Objectives 97

4.3 Materials and methods 98

 4.3.1 Synthesis of ion-doped HA nanoparticles..... 98

 4.3.2 Characterization of ion-doped HA nanoparticles..... 99

 4.3.3 Preparation and characterization of NPs suspensions 101

 4.3.4 *In vitro* cell culture studies 101

4.4 Results and discussion..... 104

4.4.1 Effect of ion doping on physicochemical properties	104
4.4.2 Effect of ion doping on cell behaviour	114
4.5 Conclusions	125
4.6 References	127
Chapter 5	
Co-/effect of Organic Molecules and Ions in Calcium Phosphate Precipitation.....	133
5.1 Introduction.....	133
5.2 Objectives	135
5.3 Materials and methods	137
5.3.1 Setting up working system	137
5.3.2 CaP precipitation in presence of organic molecules	137
5.3.3 CaP precipitation in presence of organic molecules with foreign ions	139
5.3.4 Characterization of biominerals.....	139
5.4 Results and discussion.....	141
5.4.1 The calcium phosphate precipitation system.....	141
5.4.2 Effect of organic molecules on CaP precipitation.....	142
5.4.3 Neuron-like structures analysed by TEM-based techniques	154
5.4.4 Co-effect of ions and organic molecules on CaP precipitation.....	160
5.5 Conclusions	167
5.6 References	168
Chapter 6 General Conclusions and Future Directions.....	175
6.1 General conclusions	175
6.2 Future directions	178

Chapter 1

Objectives and structure of the thesis

1.1 Motivations

As nanotechnology developed rapidly, a huge number of nanomaterials such as nanoparticles and nanotubes *etc.* have been fabricated for medical or industrial purposes. Since nanomaterials display unique physical properties as a result of nano-scale size range commensurate with biomolecules and cellular systems, they are becoming attractive materials for therapeutic and diagnostic applications in clinics¹. A wide range of nanoparticles (e.g. iron oxide, gold, silica and quantum dots) have been investigated extensively in many current biomedical fields such as gene delivery, drug release, bio-imaging and tissue engineering². Among them, hydroxyapatite (HA) nanoparticles (NPs) are beginning to become more attractive for gene/drug delivery owing to its similarity to bone minerals and biodegradability³. Since biocompatibility is a prerequisite to safely deliver genes/drugs into the cell, assessment of the cellular response to HA NPs is the key of concern for their *in vitro* and *in vivo* applications. Although there have been numerous number of studies on this topic^{4,5}, ion doping in HA NPs as one aspect that has not been assessed with regards to their impact on cells behavior. Actually, biological apatite in bone tissue consists of ion-doped HA NPs and these foreign ions in biological apatite play very important roles in bone metabolism *via* tuning the biological effects on relevant cells. Ion doping in HA bulk materials has been exploited as a powerful tool to improve their biological performance for bone regeneration⁶. However, investigations targeting the effect of various ion-doped HA in nanoparticulate form on cell behavior for future use in gene/drug delivery are scarce. On the one hand, ion doping in HA NPs could provide more suitable

carriers for gene/drug delivery; on the other hand, cells effects could be mediated by HA NPs just through doping ions because various ions could induce different cell responses upon cell types.

Essentially, biological apatite in bone tissue is sort of ion-doped HA NPs which are formed with the help of organic molecules (e.g. proteins) in vertebrates. The process of bone formation is named biomineralization. Biomineralization refers to the processes by which minerals having unique morphologies and properties are formed in living organisms under ambient conditions with the help of organic molecules⁷. Calcium phosphate (CaP) mineralization in the presence of organic molecules (e.g. polymers) has been investigated extensively for the synthesis of intriguing inorganic or organic-inorganic materials with well-defined properties^{8,9}, because CaP materials are widely spread in nature and also occur within bone and teeth (i.e. biological apatite formation). Using organic molecules to regulate CaP precipitation is not only a very promising route in the understanding of CaP biomineralization process, but also could provide the powerful strategy for the design of novel CaP materials with delicate structure and special properties for industry and medical purposes. Besides organic molecules, inorganic ions such as Mg^{2+} and Sr^{2+} are also involved in CaP biomineralization processes and play very important roles. However, investigation on the co-effect of organic molecules with inorganic doping ions on the precipitation of CaP is complex and there are very limited studies on this topic¹⁰.

1.2 Overall objectives

The aims of the current thesis are twofold. One goal is to unveil how the presence of doping ions in HA NPs affects their physicochemical properties as well as the NPs-cells interaction. The second goal of the thesis focuses on exploring the potential of biomineralization by inducing precipitation of nanostructured CaP in the presence of organic molecules and foreign ions. To achieve these two goals the following specific objectives were tackled.

For the first goal:

- Synthesis of various ion-doped HA NPs using wet chemical precipitation method under identical conditions to allow comparison of results. Strontium, magnesium, zinc, iron (III), silicon as well as carbonate were introduced to substitute for calcium, phosphate or hydroxide ions in HA NPs.
- Morphological and physicochemical characterization of the various ion-doped HA NPs and paying attention on phase composition, morphology, solubility and surface charge among others.
- Investigation of various ion-doped HA NPs on cell behavior through *in vitro* cell culture experiments using different cell types: pre-osteoblastic and cancerous cells. Different studies were made to assess NPs cytotoxicity and the internalization of NPs in cells.

The second goal of this PhD Thesis mainly focuses on the effect of organic molecules-/foreign ions in CaP precipitation. And the issues tackled with this goal are:

- Understanding the role of small organic molecules, i.e. non-ionic surfactants, anionic polymers, cationic polymers in the nucleation and crystallization of calcium phosphates. In addition to the various organic molecules, the pH, concentration of salts and addition time of the reagents were investigated to gain insight into the mechanisms of interaction.
- Morphological and chemical characterization of the CaP materials that formed from aqueous solution in the presence of organic molecules using several analytical techniques based on transmission electron microscopy studies.

- Investigation of the co-effect of selected ions and organic molecules on the nucleation and precipitation of calcium phosphates.

The specific objectives of each goal are also discussed in the respective chapters of this thesis.

1.3 Structure of thesis

The present thesis begins with the state of the art including potential uses of HA NPs in medical field and biomineralization (**Chapter 2**). In **Chapter 3** the interaction of ion-doped HA NPs with cells is discussed, focusing on only major doping-ions found in bone i.e. magnesium and carbonate ions. This chapter is followed by **Chapter 4** in which the impact of minor ions (i.e. strontium, zinc, silicon and iron) presents in bone on HA NPs' properties as well as on cell behavior is evaluated. **Chapter 5** presents the investigation on the effect of organic molecules as well as foreign ions in the process of CaP precipitation. Finally, general conclusions and future directions are presented in **Chapter 6**.

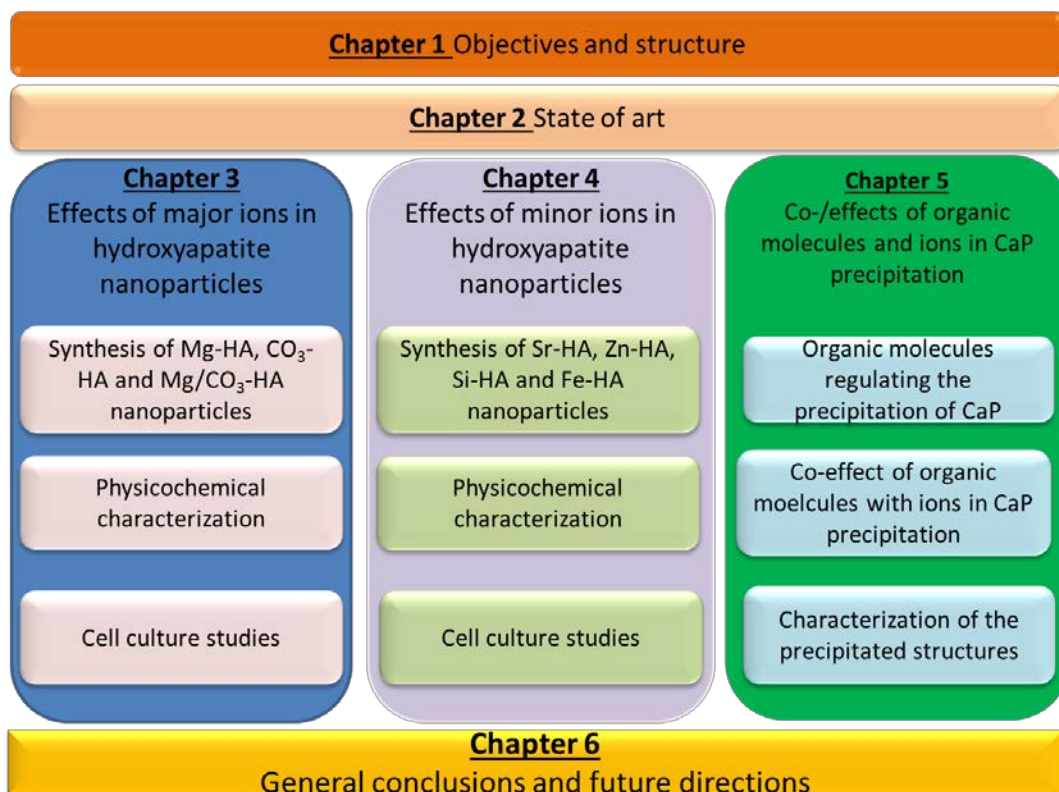


Figure 1.1 Schematic structure of the thesis.

1.4 Reference

1. Mout, R., Moyano, D. F., Rana, S. & Rotello, V. M. Surface functionalization of nanoparticles for nanomedicine. *Chem. Soc. Rev.* **41**, 2539–44 (2012).
2. Tonga, G. Y., Moyano, D. F., Kim, C. S. & Rotello, V. M. Inorganic nanoparticles for therapeutic delivery: Trials, tribulations and promise. *Curr. Opin. Colloid Interface Sci.* (2014).
3. Do, T. N. T., Lee, W.-H., Loo, C.-Y., Zavorodniy, A. V & Rohanizadeh, R. Hydroxyapatite nanoparticles as vectors for gene delivery. *Ther. Deliv.* **3**, 623–32 (2012).
4. Yuan, Y., Liu, C., Qian, J., Wang, J. & Zhang, Y. Size-mediated cytotoxicity and apoptosis of hydroxyapatite nanoparticles in human hepatoma HepG2 cells. *Biomaterials* **31**, 730–40 (2010).
5. Zhao, X. *et al.* Cytotoxicity of hydroxyapatite nanoparticles is shape and cell dependent. *Arch. Toxicol.* **87**, 1037–1052 (2013).
6. Boanini, E., Gazzano, M. & Bigi, a. Ionic substitutions in calcium phosphates synthesized at low temperature. *Acta Biomater.* **6**, 1882–94 (2010).
7. Weiner, S., Israel, R., Dove, P. M., Tech, V. & Virginia, U. S. A. An Overview of Biomineralization Processes and the Problem of the Vital Effect. *Rev. Mineral. geochemistry* **54**, 1–29 (2001).
8. Chi, C. *et al.* Biomineralization process of calcium phosphate: Modulation of the poly-amino acid with different hydroxyl/carboxyl ratios. *Mater. Chem. Phys.* **115**, 808–814 (2009).
9. Schweizer, S. & Taubert, A. Polymer-controlled, bio-inspired calcium phosphate mineralization from aqueous solution. *Macromol. Biosci.* **7**, 1085–99 (2007).
10. Yang, X. *et al.* Influence of magnesium ions and amino acids on the nucleation and growth of hydroxyapatite. *CrystEngComm* **13**, 1153–1158 (2011).

Chapter 2

State of the art

2.1 Calcium phosphates: hydroxyapatite

Calcium phosphate (CaP) is the name of a family of minerals that contain calcium ions (Ca^{2+}) together with orthophosphates (PO_4^{3-}), metaphosphates (PO_3^-) or pyrophosphates ($\text{P}_2\text{O}_7^{4-}$), some of them also containing hydrogen or hydroxide ions¹. In the present thesis the term calcium phosphate will be restricted to the calcium orthophosphate group.

Calcium phosphates are widely spread in nature both in geological and living systems. Among the various existing compounds (see Table 2.1) hydroxyapatite (HA, $\text{Ca}_{10}(\text{PO}_4)_6(\text{OH})_2$) is of great interest as it is present in the inorganic phase of the hard tissue of vertebrates such as human bones and teeth. From a chemical and structural point of view, biological apatite (i.e., the inorganic part of teeth and bone) is far from stoichiometry hydroxyapatite because of the presence of a wide range of foreign ions in the crystal lattice of HA as will be later reviewed. Besides the apatite phase, calcium phosphates also exist as amorphous (amorphous calcium phosphate, ACP) and other crystalline phases²⁻⁴ such as octacalcium phosphate (OCP), dicalcium phosphate dihydrate (DCPD, brushite), tricalcium phosphate (TCP), among others (Table 2.1).

The solubility and the calcium to phosphorous molar ratio (Ca/P) are the most important parameters to distinguish among calcium phosphate phases (Table 2.1). Normally, the lower the Ca/P molar ratio is, the more soluble the calcium phosphate becomes. Most calcium phosphates are sparingly soluble in neutral and basic pH, but all of them can dissolve in an acidic environment. As it is shown in Table 2.1, HA is the less soluble CaP phase and it can be synthesized under neutral or basic conditions (pH 9-12)⁷, while DCPD and OCP phases are often encountered

in acidic solutions⁸. It is now recognized that the crystallization process for many calcium phosphates involve the formation of metastable precursor phases^{3,9,10}. For example, during the process of apatite formation *in vitro*, DCPD and OCP have often been found and are considered as precursor phases that precipitate first and then transform to the apatitic phase^{8,11}. Additionally, *in vivo* studies on bone and enamel formation suggested the presence of a transient amorphous phase (ACP) and OCP phase followed by transformation to apatite¹²⁻¹⁷. ACPs are believed to serve as a reservoir of calcium and phosphate ions and they were also found in many other biological systems such as otoliths of blue sharks^{18,19}.

Table 2.1 Ca/P ratio, chemical formula, and solubility of calcium phosphate mineral^{5,6}

Abbreviation	Formula	Name (mineral)	Ca/P ratio	pK _{sp}	pH stability
HA	Ca ₁₀ (PO ₄) ₆ (OH) ₂	Hydroxyapatite	1.67	116.8	9.5-12
OCP	Ca ₈ (PO ₄) ₆ ·5H ₂ O	Octacalcium phosphate	1.33	96.6	5.5-7.0
β-TCP	Ca ₃ (PO ₄) ₂	β-Tricalcium phosphate (whitlockite)	1.5	28.9	<i>b</i>
α-TCP	Ca ₃ (PO ₄) ₂	α-Tricalcium phosphate	1.5	25.5	<i>b</i>
ACP	Ca _x (PO ₄) _y ·nH ₂ O	Amorphous calcium phosphate	1.2-2.2	<i>a</i>	5-12 ^c
MCPM	Ca(H ₂ PO ₄) ₂ ·H ₂ O	Monocalcium phosphate monohydrate	0.5	1.14	0-2
MCPA	Ca(H ₂ PO ₄) ₂	Anhydrous monocalcium phosphate	0.5	1.14	<i>b</i>
DCPD	Ca(HPO ₄) ₂ ·2H ₂ O	Dicalcium phosphate dehydrate (brushite)	1.0	6.59	2-6
DCPA	Ca(HPO ₄)	Anhydrous dicalcium phosphate (monetite)	1.0	6.90	<i>b</i>
TTCP	Ca ₄ (PO ₄) ₂	Tetracalcium phosphate	2.0	38-44	<i>b</i>
CDHA	Ca _{10-x} (HPO ₄) _x (PO ₄) _{6-x} (OH) _{2-x}	Calcium-deficient hydroxyapatite	1.5	85.1	6.5-9.5

a Cannot be measured precisely.

b Phases obtained by solid-state reaction or heat treatment of other phases.

c Always metastable.

Among the CaP family, synthetic HA has been the focus of extensive investigation in the biomedical field. On one hand, HA bulk materials have often been used for bone tissue regeneration, soft tissue repair and bone tissue engineering due to their excellent biocompatibility, osteoconductivity and similarity to the inorganic component of bone²⁰⁻²². Since 1980s when HA ceramic was first found to be osteoconductive and promote bone formation²³, extensive *in vivo* studies have been performed and suggested that HA bone grafts can form bioactive bonds with the host bone and integrate with new bone²⁴. HA synthetic bone grafts have also been widely used in clinics and showed good bone repair function. In clinical practice, HA materials are applied as (1) powders or granules as bone defect fillers²⁵; (2) particles as the component for tooth pastes and bone cements²⁶; (3) porous scaffolds acting as temporary substrates for cell in-growth and new bone development under non-loading sites²⁷; (4) bioactive coating on metal implants²⁸. In addition, HA is also employed as the inorganic phase in polymer-inorganic composites for bone tissue repair²⁹⁻³¹. The addition of HA in composites not only improves the bioactivity but also enhances the mechanical properties of materials for bone regeneration.

On the other hand, HA materials in nanoparticulate form can be used for gene/drug delivery applications, bio-imaging and cancer therapy³²⁻³⁵, and these applications will be described in detail in following sections. Additionally, HA is also exploited as a model compound to mimic biomineralization processes^{36,37}. Owing to the inherent interest of HA, the present thesis mainly focuses on this compound.

2.1.1 Composition and structure of hydroxyapatite

As already mentioned in the preceding section, HA with the chemical formula $\text{Ca}_{10}(\text{PO}_4)_6(\text{OH})_2$ is the most stable calcium phosphate phase at ambient temperature and neutral pH (Table 2.1). The Ca/P ratio of stoichiometric HA is 1.67. HA can crystallize in two different crystal systems: monoclinic, with space group $\text{P}2_1/\text{b}$, and hexagonal, with $\text{P}6_3/\text{m}$ space group. The hexagonal structure is typical for apatite precipitated at low temperature (biological apatite) while the

monoclinic form is mainly found in nearly stoichiometric and defect free (from impurities and vacancies) apatites synthesized at high temperature^{38,39}.

The lattice parameters for the hexagonal structure are $a=b=9.432$, $c=6.881\text{\AA}$ and $\gamma=120^\circ$. As it can be observed in Figure 2.1 the structure contains two different cation sites, Ca(I) ions are aligned in columns parallel to the OH ions and Ca(II) ions are arranged forming staggered equilateral triangles. There is only one environment for phosphates which forms tetrahedrons held together by Ca ions. Basically, the structure can be described as a phosphate assembly crossed by parallel channels filled by OH ions and parallel to the crystallographic c -axis (Figure 2.1).

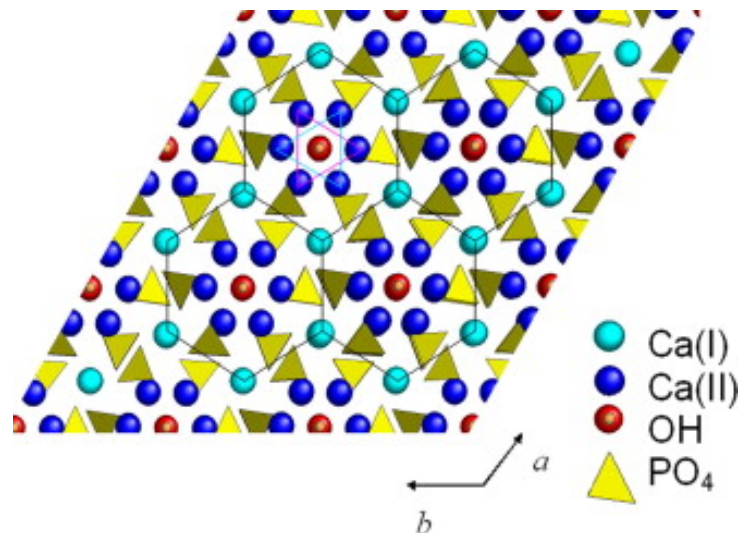


Figure 2.1 A view of the HA structure along the c -axis. Black lines connect Ca(I) columns in hexagonal networks. Cyan and magenta triangles connect staggered Ca(II) atoms lying in the same plane, but at different height with respect to the c -axis⁵.

The monoclinic structure has as lattice parameter $a = 9.421\text{\AA}$, $b=2a$ $c=6.881\text{\AA}$ and $\gamma=120^\circ$. The orientation of the hydroxyl groups is the key feature that distinguishes the monoclinic from the hexagonal structure. In the monoclinic HA all of the OH groups in a given column point in the same direction and the direction reverses in the next column. This change in the orientation is responsible for the doubling of the b -axis³⁸. In the hexagonal structure the hydroxyl ions are randomly oriented compensating each other thus preserving the hexagonal symmetry.

2.1.2 Biological apatite

Biological apatite is found in bone as a natural organic–inorganic nanocomposite²³. The main components of bone can be categorized in three groups: 1) inorganic mineral phase (65 wt%) consisting of apatite; 2) organic phases (25 wt%) including collagen and non-collagen proteins and cells; 3) water (10 wt%)⁴⁰. All these components are perfectly organized at several hierarchical levels ranging from the nanometer to the macroscopic scale in order to achieve excellent properties and performance (Figure 2.2).

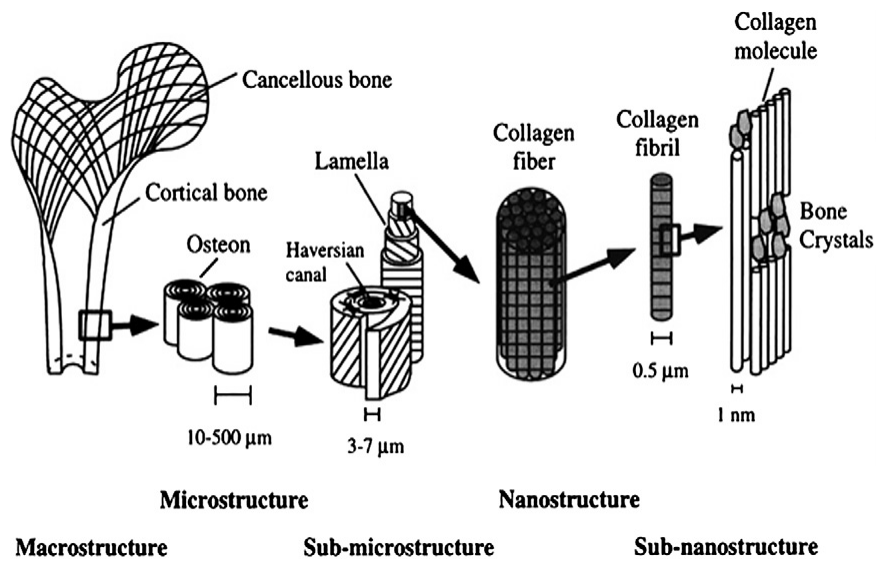


Figure 2.2 The hierarchical structure of bone at its various length scales. The microstructure of cortical bone consists of osteons with Haversian canals and lamellae, and at the nanoscale, the structural units are collagen fibers composed of bundles of mineralized collagen fibrils⁴¹.

The apatite crystals in bone have a plate-like habit and are nanosized with a length of ~20–50 nm, and a width of 12–20 nm, and a thickness of 2–5 nm⁴². These dimensions depend however on age and species⁴³. The presence of this mineral phase is crucial as imparts an appropriate strength and toughness. Additionally, apatite in bone tissue also acts as a reservoir of ions such as Ca^{2+} , PO_4^{3-} . Aside from their size the most distinct feature that distinguishes synthetic from biological apatite is the wide range of foreign ions that are either incorporated in the apatite crystal lattice or adsorbed on the crystal surface (Table 2.2). Various types of bivalent or monovalent cations in biological apatite can substitute Ca^{2+} ions, while PO_4^{3-} sites can be substituted by other anions such as CO_3^{2-} (type B, the major form

of biological apatite) and SiO_4^{4-} ions. Moreover, the OH^- site can be occupied by CO_3^{2-} and ions such as F.⁴⁴ Therefore, the chemical formula for biological apatites is better described as $\text{Ca}_{10-x}\text{M}_x(\text{PO}_4)_{6-y}(\text{HPO}_4, \text{CO}_3)_y(\text{OH})_{2-z}\text{N}_z$ where M and N stands for cationic metal ions and anionic ions, respectively, and x, y and z are the molar number of foreign ions ($0 < x, y, z < 2$)^{45,46}. To this already complex system one fact has to add that the chemical composition of biological apatite varies with the type of bone, age and gender⁴⁷.

Table 2.2 Comparative composition of human enamel, dentin and bone.⁵

	Enamel	Dentine	Bone
Ca (wt.%)	37.6	40.3	36.6
P (wt.%)	18.3	18.6	17.1
CO₂ (wt.%)	3.0	4.8	4.8
Na (wt.%)	0.70	0.1	1.0
K (wt.%)	0.05	0.07	0.07
Mg (wt.%)	0.2	1.1	0.6
Sr (wt.%)	0.03	0.04	0.05
Cl (wt.%)	0.4	0.27	0.1
F (wt.%)	0.01	0.07	0.1
Zn (ppm)	263	173	39
Ba (ppm)	125	129	
Fe (ppm)	118	93	
Al (ppm)	86	69	
Ag (ppm)	0.6	2	
Cr (ppm)	1	2	0.33
Co (ppm)	0.1	1	<0.025
Sb (ppm)	1	0.7	0.17
Mn (ppm)	0.6	0.6	
Au (ppm)	0.1	0.07	
Br(ppm)	34	114	
Si (ppm)			500
Ca/Pa	1.59	1.67	1.65

It is interesting to note that although the level for some of the ion substitutions in bone is small, these elements are of great importance for the properties of biological apatite and can influence bone, enamel and dentin formation. For example, Mg ions (making up less than 1 wt% of bone) play a key role in bone metabolism⁵ as it influences osteoblasts (cells which are responsible for bone production and mineralization) and osteoclasts (cells which are responsible for bone resorption) activity^{48,49}. Strontium ions have been indicated to promote bone formation *in vivo* by enhancing pre-osteoblasts (cells which are induced to differentiate to osteoblasts under the influence of growth factors) replication and osteoblasts differentiation⁵⁰⁻⁵². Zinc ions have also been found to stimulate the bone growth and bone mineralization due to the opposite effects on osteoblasts and osteoclasts cells (inhibiting osteoclast differentiation while promoting osteoblast activity)⁵³. Besides, Zinc is also known to be an essential trace element in enzyme activity, maintenance of membrane structure and function.⁵⁴

Since the presence of these ions in biological apatite even if in small amounts play such important role in bone formation, ionic substitutions into HA have been proposed as a tool to mimic the chemical composition of bone and improve the biological performance of HA-based materials for bone tissue repair^{55,56}. In fact, there have been numerous studies on this topic. Many of them have focused on cationic substitution of Ca using Mg, Sr, Zn, Fe ions among others⁵⁷⁻⁶¹, while other studies have focused on anionic substitutions targeting either the PO_4^{3-} or OH^- sites for F^- , CO_3^{2-} and SiO_4^{4-} *etc*^{44,62,63}. In addition, ion co-substitutions in HA (more than one ionic species) such as Mg with CO_3 , Sr with CO_3 , and Mg with Sr have also been investigated⁶⁴⁻⁶⁶. In any case one has to bear in mind that ionic substitutions do not only “adds in” the ion of interest but this often carries significant disturbances to the crystal influencing the physicochemical properties of HA such as particle morphology, crystallinity and solubility through inducing structural disorder^{56,67}. For example, substitution of carbonates in HA changes the morphology of the apatite crystals, from a plate-like or a needle-like to a spheroidal morphology with increasing carbonate content; the presence of carbonate in the apatite lattice also causes a decrease in crystallinity and an increase in solubility⁶⁸; Mg ions inhibit hydroxyapatite crystal nucleation and growth leading to a lower crystallinity^{5,69}.

Ion substituted HA materials in bulk form have been evaluated *in vitro and in vivo* suggesting that they could be excellent candidates for bone tissue regeneration. For example, CO₃ substituted HA materials have shown improved mechanical and biological properties⁴⁴; Mg substituted HA as bone fillers have been shown to significantly improve bone formation by improving adhesion, proliferation and metabolic activation of bone formation-related cells as compared to stoichiometric HA⁵⁷; silicate (SiO₄⁴⁻) in the HA structure significantly improved *in vivo* bioactivity and made this material attractive for bone substitute ceramics^{63,70,71}. In addition, *in vitro* studies using Sr substituted HA materials indicated that osteoblast activity and differentiation could be readily stimulated⁷².

2.2 The potential of hydroxyapatite nanoparticles in biomedical applications

Aside from the great use of hydroxyapatite as bulk materials in bone regenerative applications, the huge development that nanotechnology has been experiencing has led to the investigation of HA nanoparticles (NPs) in their dispersed form in various new-emerging biomedical fields such as gene/drug delivery, bio-imaging and cancer therapy^{34,35}. In any of these applications it is important that NPs fulfill very specific requirements:

- NPs should be **biocompatible**: non-cytotoxic, non-genotoxic and non-immunotoxic.
- They should have **affinity** for the cargo (gene/drug) whenever this is needed and be capable of **releasing** the cargo at the targeted site.
- They should **target specifically** the desired cell type or diseased site.
- They should be **biodegradable**. After fulfilling their function they should degrade without inducing any cytotoxicity.

- They should be easy to prepare in a reproducible manner.

Interestingly, the works published on the use of HA NPs are very promising and have proven that HA are capable of fulfilling all the above mentioned requirements:

- The fact that HA is the mineral phase of bone already ensures their **biocompatibility**.
- HA NPs have proven to have **much higher affinity** to proteins, DNA and many different drugs than bulk materials owing to their high surface area-volume ratio⁷³.
- HA nanoparticles could target specifically on desired cells or diseased sites by **surface functionalization** using specific molecules such as ligands and antibodies⁷⁴.
- As discussed above HA could **dissolve** in acidic conditions. For example, pH values in the extracellular environments of solid tumors (pH 6) are lower than that of normal tissues and this could enable a preferential active cargo release from apatite surface in the tumor region⁷⁵. On the other hand, the degradation products of HA, Ca^{2+} and PO_4^{3-} are non-toxic since they are already inherent to the body.

However, in spite of the potential offered by HA NPs there are many aspects from the NPs themselves that can affect their interaction with cells or the diseased site and need to be taken into account:

- **Particle size.** This factor is pivotal for nanoparticles to deliver their cargo to the targeted site. On the one hand, particle size can influence the circulation and bio-distribution of NPs in the body. If the administrated nanoparticles are too small (10-20 nm) they could be rapidly excreted in the urine through the kidney without any chance to reach the target sites⁷⁶,

however, when nanoparticles are too big ($> 1 \mu\text{m}$) they can be recognized by the immune system and given a rapid clearance by macrophages^{77,78}. However, when the particle size are among these two extremes ($20 \text{ nm} < d < 1 \mu\text{m}$), all of these clearance mechanisms are minimized, and circulation time is greatly prolonged⁷⁹. On the other hand, particle size also plays a key role dictating the mechanism of internalization in cells. Normally, NPs smaller than 200 nm are expected to enter cells via endocytosis (specifically by micro-pinocytosis) but if the size of the NPs is of several hundreds of nm, they could enter by macro-pinocytosis⁸⁰.

- **Surface charge.** In comparison to NPs with negative and neutral surface charge, positive surface charge favours internalization of the NPs in targeted cells owing to the negative surface charge exhibited by the cell membrane thus generating electrostatic attraction with the positively charged NPs⁸¹. It has shown by some research groups that HA NPs with positive zeta potentials have a higher cellular uptake compared to nanoparticles with a negative zeta potential⁸².
- **Particle shape.** Particle shape also plays an important role in various biological processes associated with therapeutic delivery. Recent studies showed that cellular uptake of NPs could be affected by their shapes^{83,84}.

The foreseen potential of HA NPs has yielded very positive results in various fields of applications as will be reviewed in the next sections.

2.2.1 Gene delivery

Theoretically, gene therapy is a simple approach that introduces therapeutic DNA into the nucleus of target cells, replacing the distorted gene by a healthy one, or completing a missing gene in order to express the desired protein⁸⁵, Figure 2.3 displays the schematic view of gene delivery using a cationic polymer as carrier. In spite of the potential that holds gene therapy, in practice it has yet to be applied

successfully to treat human diseases. The underlying problem is not associated to the genes themselves, but to the delivery of genes inside the desired cells⁸⁶⁻⁸⁸.

The process of DNA entry through the cell membrane all the way to the nucleus to produce the required protein is called transfection^{89,90}. Transfection efficiency is thus a key parameter in gene therapy. Nude DNA molecules are unable to give adequate transfection efficiencies, due to the negative charge of DNA which inhibits cellular internalization but also to the fact that naked DNA can easily be degraded by enzymes and subsequently be removed by the macrophage system⁸⁵. Thus, the need of carriers becomes imperative. Even when having good carriers the trajectory of DNA from the extracellular space to the cell nuclei still need to overcome various barriers to achieve transfection: (1) the physical and chemical stability of DNA needs to be preserved, (2) cells have to uptake the carrier by endocytosis⁷⁹, (3) the carrier will then need to escape from endosomes to the cytosol⁹¹ and, (4) from the cytosol DNA will need to be transported to the nucleus for transfection⁹².

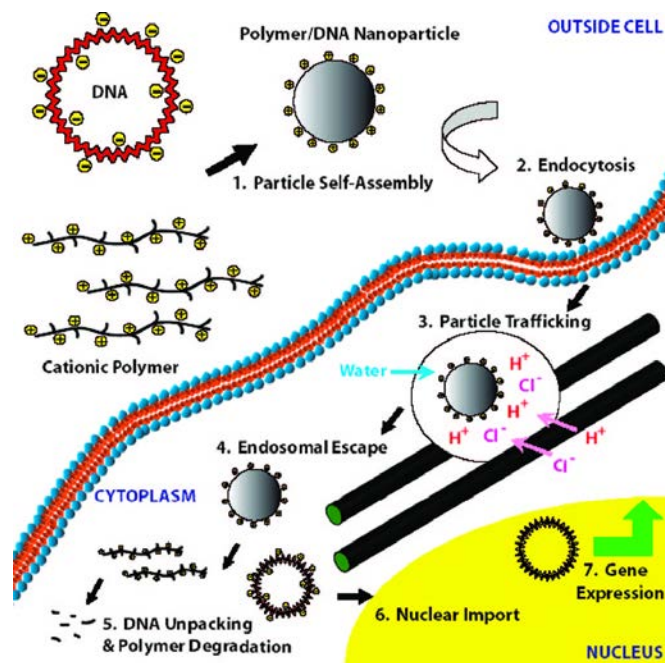


Figure 2.3 Schematic of non-viral gene delivery, cationic polymer is given as one sample of gene carrier⁹³.

Currently, there are two types of carriers for delivering genes into targeted cells: viral and non-viral carriers⁹⁰. Viruses have been playing a very important role in gene delivery due to their high gene transfection efficiencies⁹⁴. However, their major limitations with regards to immunogenicity and cytotoxicity have shifted their popularity towards synthetic non-viral gene delivery systems⁹⁵. Recently, various materials have been employed as potential non-viral gene carriers such as cationic polymers (*e.g.* polyethyleneimine (PEI), chitosan and poly-L-lysine)⁹⁶⁻⁹⁸, lipids (liposomes)⁹⁹ and inorganic materials (*e.g.* magnetic nanoparticles, gold and silica)¹⁰⁰. Cationic polymers and lipids are often used as gene carriers due to their high capacity of loading negatively charged DNA molecules and the ability to permeate cells membranes¹⁰¹, however, toxicity is still an obstacle for their application in gene therapy¹⁰². Some inorganic nanoparticles such as metallic nanoparticles, iron oxide and silica are also attractive candidates for gene delivery because they can be prepared and surface-functionalized in many different ways to obtain a wide array of physical and structural properties. However, they still have their own weakness, for example, several of them suffer from toxicity issues and several suffer from non-biodegradability^{100,103,104}.

In comparison to lipids, cationic carriers and other inorganic carriers, HA NPs display many advantages³⁵: (1) Affinity to DNA molecules as a result of the ionic interactions between Ca^{2+} and the negatively charged backbone in DNA⁷³. (2) Biocompatibility. The degradation products of HA, Ca^{2+} and PO_4^{3-} , are non-toxic since they are already inherent to the body¹⁰⁵. (3) Easy synthesis methods and low-cost¹⁰⁶. Importantly, HA carriers can help DNA molecules escape from endosomes. Unlike other non-viral carriers HA NPs can easily disrupt the endosome as they begin to dissolve in the acidic environment of the endosomal compartment and release Ca^{2+} ions which are the ones able to break down endosomes through osmotic imbalance thus delivering the gene into the cytosol^{91,107}.

Moreover, DNA molecules could entry into the cell nucleus facilitated by the elevated Ca^{2+} ions freed in the cytosol. As depicted in Figure 2.4, when excessive exogenous Ca^{2+} ions are present in cytoplasm, Ca^{2+} ions accumulated in the nuclear

membrane cisternae can open the nuclear pore complex (NPC) and allow the gene to easily enter the nucleus. In contrast, gene delivery through conventional non-viral vectors such as liposomes or polymers cannot enter the nucleus through the NPC without the help of nuclear localization signals¹⁰⁸. Additionally, the entrance of DNA into the nuclei can also take place during cell mitosis provided DNA is freed in the cytosol: during cell division the nuclear membrane breaks facilitating their entrance.

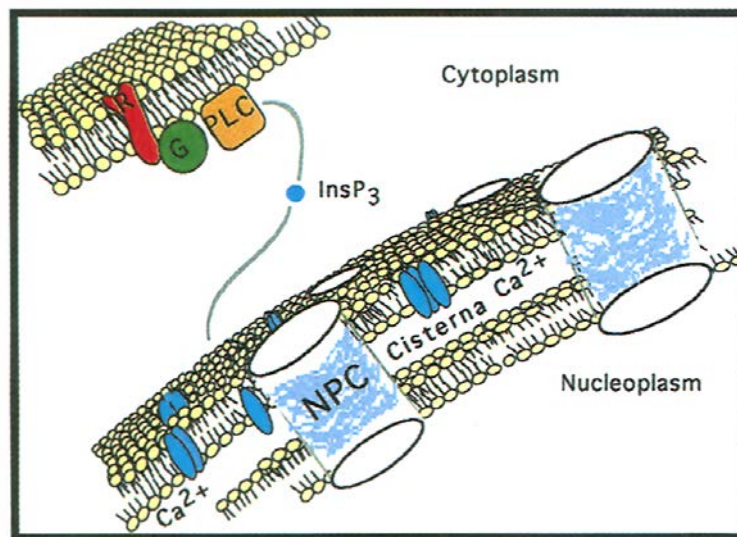


Figure 2.4 Schematic of the components of the nuclear membrane involved in Ca^{2+} regulated transport through the nuclear pore complex (NPC).¹⁰⁸

There are various studies that have tested the use of HA NPs in gene delivery applications *in vitro* and *in vivo*. For example, Zhu *et al.*¹⁰⁹ prepared HA NPs with 40-60nm particle size and used them to transfect a gastric cancer cell line (SGC-7901) with enhanced green fluorescent protein (EGFP)-N1. The use of EGFP is a common strategy that allows proving protein expression by exhibiting bright green fluorescence upon successful transfection. In this manner it was proved that the transfection efficiency was 80%. In addition, another research group confirmed the ability of HA NPs loaded with genes to overcome the barriers of endosomal escape and enzymatic degradation, and through *in vitro* studies revealed higher transfection activities for HA nanoparticles than the commercial agent (cationic polymer)¹¹⁰. To treat cancers, an *in vitro* study on the anti-tumor effect of pEGFP-C1-p53 gene-loaded on HA NPs was performed and indicated that the killing effect

was effective toward human hepatoma cells (Hep-3B) and hemochromatotic cell line (HuH-7)¹¹¹; *in vivo* experiments performed in mice indicated that the growth of tumor was inhibited. In the study by Wu *et al.* it was demonstrated that HA NPs had ultra-high DNA loading capacity if DNA was adsorbed in the presence of Ca²⁺ (0.2 mol/L). The loading capacity was enhanced by one or two orders of magnitude compared with the recently reported mesoporous silica¹¹².

2.2.2 Bio-imaging

Imaging of tissues or intracellular structures is an important topic in biomedicine¹¹³. HA NPs can be used for bio-imaging purposes by doping with lanthanide ions. Doping even with a small amount of these ions can display high fluorescence efficiency¹¹⁴. Different fluorescence colours can be made by doping with different lanthanide ions, for example, europium-doped nanoparticles can emit red light while terbium-doped particles emit green light³⁴. However, crystallinity plays a key role in the fluorescence efficiency of NPs being very weak in amorphous phases. In addition to the use of lanthanide ions, another possibility to use HA NPs in bio-imaging is by encasing fluorescent dyes *via* surface-functionalization or by co-precipitation methods. For example, Morgan *et al.* obtained 20-30 nm diameter HA nanoparticles in the presence of a variety of fluorescent dyes such as Cascade Blue and fluorescein sodium salt and these dyes were shown to be successfully encapsulated in HA¹¹⁵. In the study by Altinoglu *et al.*¹¹⁶ sub-50 nm and biocompatible CaP nanoparticles were also prepared for bio-imaging. In their study, indocyanine green (ICG) which is a deep-tissue imaging molecule was investigated and the results demonstrated that this nanoparticle-based system was readily taken up by desired cells, showing efficient bio-imaging efficiency *in vivo*. In addition, to gain insights into the fate of the NPs after they had crossed the cell membrane, Williams *et al.*¹¹⁷ engrafted a fluorescent dye (Fluorescein-5-Maleimide) on the HA NPs to facilitate real-time biological tracking. *In vitro* experiments showed that the nanoparticles with fluorescent dye could be discriminated from other biological debris following internalization by cells and the particles were shown to maintain fluorescence for 24 hours without quenching.

2.2.3 Cancer therapy

HA NPs can be applied in cancer therapy in two different directions. One way is to use the HA NPs as carriers to deliver anti-cancer drugs. This strategy has the advantage that the NP will dissolve either in the low pH of the lysosomes (pH 5) after the cellular uptake or in the environment of solid tumours (pH 5-6)¹¹⁸ releasing the incorporated anti-cancer drug. Besides, HA nanoparticles can be made to fluoresce through the incorporation of lanthanide ions or through the absorption of dyes as discussed above and this strategy can be used to track drugs release and its bio-distribution.

Palazzo *et al.* prepared biomimetic HA nano-materials with plate-like shape and investigated the adsorption mechanism of anti-cancer drugs (cisplatin) on them suggesting that adsorption was driven by electrostatic attraction¹¹⁹. Rodríguez *et al.* evaluated the efficiency of citrate-functionalized HA apatite as carriers for delivering doxorubicin (DOXO, common drug used in cancer therapy) *in vitro*. The results demonstrated that human carcinoma cells can easily take up the drug-nanoparticle complexes, and the released DOXO molecules from the HA NPs accumulated in the nucleus in short times and exerted cytotoxic activity⁷⁵. In addition, to enhance DOXO-loading capacity Yang *et al.*¹²⁰ synthesized HA NPs with a hollow core and mesoporous shell structure and they exhibited an excellent drug-loading efficiency as well as an enhanced anticancer efficacy compared with free DOXO.

Besides the loading of anticancer drugs on HA, another strategy is to use NPs with an inherent anti-cancer activity. This possibility emerged from the observance that certain NPs were found to significantly inhibit the proliferation of several types of cancer cells such as gastric cancer, colon cancer, melanoma, breast cancer and glioma cells, while having minimal side effects on normal cells. For example, Sangeeta *et al.*¹²¹ investigated the effect of particle size, morphology and crystallinity on human colorectal cancer cells (HCT116) and found that the decrease in crystallite size of the HA NPs significantly increased the inhibition of HCT116 cell growth. In addition, Liu *et al.* investigated the effect of HA NPs on the

behavior of human hepatoma cells and showed that HA NPs inhibited the cell growth in a dose-dependent manner¹²². Qing *et al.*¹²³ found that HA NPs caused apoptosis of human osteosarcoma (MG-63) cells, whereas no apoptosis could be found in normal osteoblasts. The *in vivo* study by Hu *et al.*¹²⁴ proved that HA NPs had a clear inhibitory action on rabbit implanted hepatic tumours. Regarding the mechanisms responsible for cells apoptosis, it was suggested that the increase in intracellular reactive oxygen species (ROS) and the elevated concentration of cytosolic calcium ions might have caused cell death after cellular internalization of HA¹²⁵. Another research group inferred that the location of nanoparticles inside cells also had a predominant effect on the HA NPs-induced cytotoxicity and the nuclear localization of the particles might be the main mechanism of growth inhibition by HA NPs in cancer cells¹²⁶.

Regardless of the promising results that have been put forward in the above mentioned examples, there are still many problems and challenges that need to be further investigated in detail before NPs can be used. For example, the characteristics of the nanoparticles play a critical role in their performance in these applications, and, unfortunately, not in all the works NPs have been well characterized. Additionally, the performance of HA nanoparticles in biomedical applications also depends on its chemical compositions, this aspect has not been well understood.

2.3 Synthesis of hydroxyapatite nanoparticles

From the literature it is readily visible that there are various preparation methods that can be used to synthesize well-defined HA nanoparticles having suitable physicochemical properties for their effective and safe use in biomedical applications^{34,106,127}. These methods can be classified into three main groups: dry methods, wet methods and high-temperature processes. Each group can further be divided into subgroups as shown in Table 2.3.

Table 2.3 Comparison of different methods for preparation of HA NPs¹⁰⁶

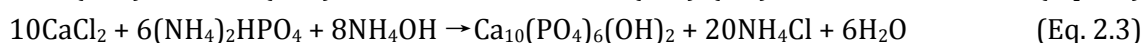
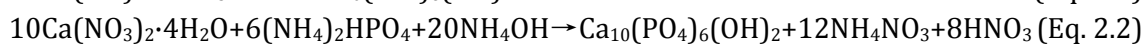
Method		Morphology	Crystallinity degree	Phase purity	Ca/P ratio	Size
Dry methods	Solid-state method	Diverse	Very high	Usually low	Variable	Usually micro
	Mechanochemical method	Diverse	Very high	Low	Usually Non-stoichiometric	Nano
Wet methods	Chemical precipitation	Diverse	Frequently low	Variable	Non-stoichiometric	Usually nano
	Hydrolysis method	Diverse	Variable	Usually high	stoichiometric	Variable
	Sol-gel method	Frequently needle-like	Variable	Variable	stoichiometric	Nano
	Hydrothermal method	Frequently need-like	Very high	Usually high	stoichiometric	nano or micro
	Emulsion	Diverse	Frequently low	Variable	Non-stoichiometric	Nano
High Temp. processes	Combustion method	Diverse	Variable	Usually high	Variable	Usually nano
	Pyrolysis method	Diverse	High	Variable	Usually stoichiometric	

Among the three main groups wet methods are the most commonly used and in particular, conventional chemical precipitation method is one of the most popular methods followed by hydrothermal synthesis method and emulsion method which are the next most well-known methods of preparing HA nanoparticles. In the following section, these popular wet methods of preparation of HA nanoparticles will be discussed.

Wet methods, in contrast to dry and high temperature methods have the advantages of simplicity, cost saving, ease of use and, in some cases do not even require the use of any especial equipment such as furnaces or mills which are essential in high temperature and dry methods, respectively.

2.3.1 Wet chemical precipitation

The wet chemical precipitation method is by far the most popular method and the prove of it is that has already been used for many years¹²⁸. It is based on the fact that, at room temperature and pH above 4.2, HA is the least soluble and usually the most stable CaP phase in an aqueous solution. Although there are many possible reactions to produce HA, two of the most typical reactions are: 1) the stoichiometric titration of calcium hydroxide slurry with phosphoric acid (Eq. 2.1); 2) precipitation following the drop-wise addition of a solution of ammonium or sodium monohydrogen phosphate to a calcium solution (generally calcium nitrate or calcium chloride) or vice versa⁵ (Eq. 2.2 and Eq. 2.3).



Among these two reactions, reaction **2.1** (Eq. 2.1) is very attractive as the only by-product is water and also the reaction is “self-controlled at high pH”, thus no addition of any other chemical (e.g. ammonia in reaction **2.2** and **2.3**) is needed to maintain the conditions necessary for the precipitation of the apatite phase instead of other calcium phosphates. The typical morphology for the NPs obtained via wet precipitation methods is usually needle-like as shown in Figure 2.5.

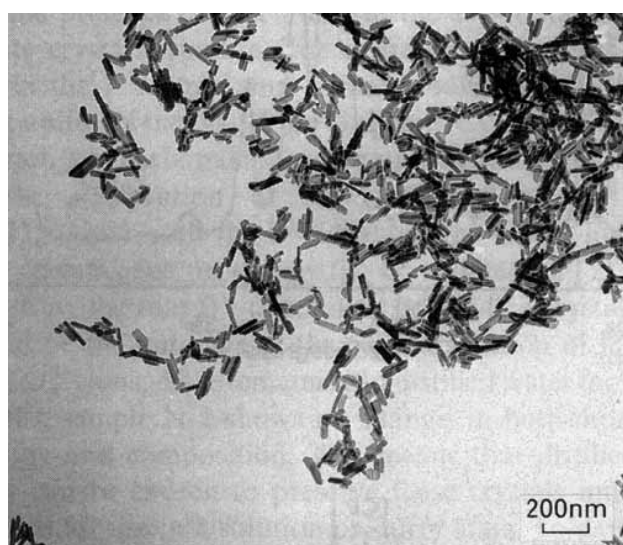


Figure 2.5 TEM image of HA needle-like crystals obtained by wet chemical precipitation¹²⁹.

Aside of the fact that wet processes are easy to conduct, the shape, size and specific surface area of the HA nanoparticles can be easily tuned adjusting reaction parameters such as the reactant addition rate and temperature during synthesis. The reactant addition rate determines the purity of the synthesized HA and is strongly linked to the pH during the synthesis. Thus if, phosphoric acid is added too fast in reaction 2.1 (Eq. 2.1) the likelihood of forming protonated species becomes too high and the resulting HA might end up containing HPO_4^{3-} groups in addition to PO_4^{3-} . Reaction temperature is also reported to affect particle size of HA and it does so in a linear manner as the driving force for the growth rate of HA NPs increases with temperature, which explains for the larger particle sizes at higher temperatures¹²⁹. The reaction temperature also determines whether the crystals are monocrystalline or polycrystalline. Usually, HA particles synthesized at low temperature ($T < 60$ °C) are monocrystalline, above this critical temperature nanocrystals become polycrystalline¹²⁷.

One additional advantage of this precipitation method is that HA NPs can be easily doped with many different ions by simply adding the salt of interest during precipitation. This strategy has been used to improve the biological performance of HA and has been the subject of increasing interest over the past decade⁵. In addition to altering NPs composition, doped ions can also affect NPs morphology, solubility, crystallinity and so on. With regards to morphology modifying strategies, it is important to point out that the morphology of HA NPs can further be modified -without necessarily affecting composition- by adding foreign molecules during synthesis¹³⁰.

The main disadvantage when using wet chemical precipitation methods is agglomeration. If dispersing agents are not added during synthesis, hydroxyapatite nanoparticles become agglomerated, resulting in increased particle size and irregular shapes¹³¹.

2.3.2 Hydrothermal treatment

In hydrothermal processes the reaction takes place at elevated temperatures and pressures. Hydrothermal synthesis can also simply be considered as a chemical precipitation in which the aging step is conducted at a high temperature—typically above the boiling point of water—inside an autoclave or pressure vessel. HA nanoparticles with high crystallinity and good stoichiometry can be obtained *via* this method¹³². Figure 2.6 displays one example of HA NPs prepared by hydrothermal methods¹³³.

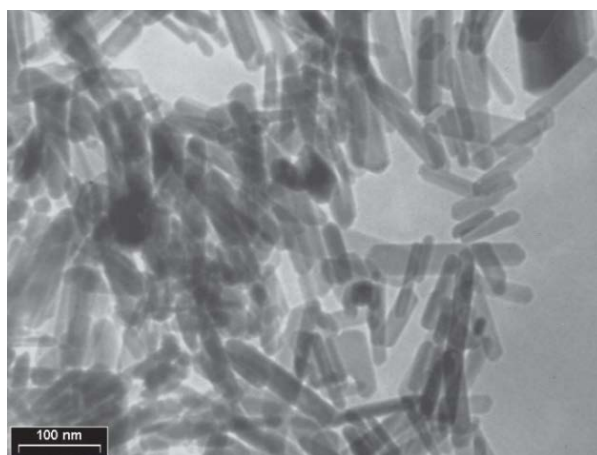


Figure 2.6 TEM image of HA needle-like crystals obtained by hydrothermal methods¹³³.

Additionally, organic additives such as ethylenediaminetetraacetic acid (EDTA), polyamidoamine dendrimer among others can be used to modify the morphology of the HA NPs during hydrothermal synthesis¹³⁴. These molecules act by binding to specific crystal faces inhibiting their growth and modulating the final morphology of the nanoparticle. Plate-like nanoparticles mimicking the morphology of apatite in bone tissue have been obtained through hydrothermal synthesis using sodium tripolyphosphate (STPP) as a modifying agent. The main limitations for the hydrothermal treatment are the harsh reaction conditions (high temperature and pressure).

2.3.3 Micro-emulsion synthesis

A micro-emulsion is a thermodynamically stable transparent solution of two immiscible liquids such as water and oil in which an amphiphilic surface-active

agent or surfactant is usually used to stabilize this two phases by controlling their interfacial tension. Taking the case of water-in-oil micro-emulsion for example (Figure 2.7), reverse micelles is firstly formed, and then the aqueous phase is dispersed as micro-droplets surrounded by a mono-layer of surfactant molecules in the continuous non-aqueous (oil) phase. These micro-droplets of water stabilized in a non-aqueous phase by a surfactant act as micro-reactors or nano-reactors in which chemical reactions are conducted and the formation of HA nanoparticles can be facilitated¹³⁵.

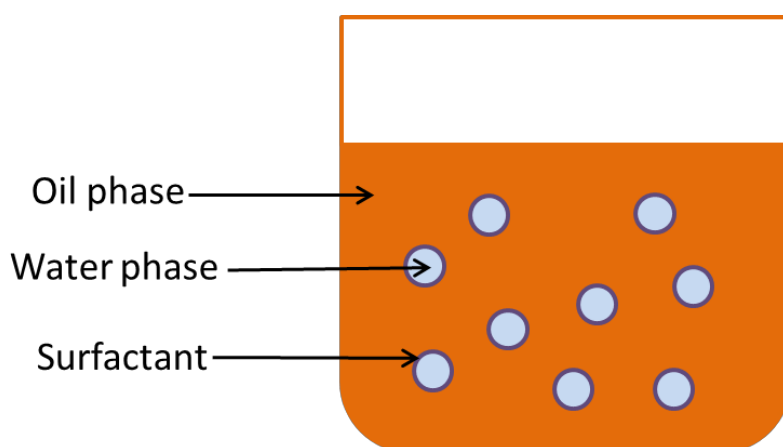


Figure 2.7 Water-in-oil micro-emulsion systems to prepare hydroxyapatite nanoparticles

Accordingly, synthesis of HA nanoparticles using micro-emulsions carries the main advantage of decreased aggregation¹³⁶. This technique is now a subject of great interest not only to prepare an agglomerate-free powder, but also to control the microstructure and morphology of the resulting particles. Indeed, among the many different wet processes developed for HA synthesis, emulsion method is suggested to be more efficient to reduce the particle size, to control the morphology, and to limit the agglomeration of HA particles. Experimental conditions such as aqueous/organic phase volume ratio, pH, aging time, temperature, and ion concentration in the aqueous phase can affect the crystalline phase, surface area, particle size and morphology of HA¹³⁷. Figure 2.8 shows typical micrographs of HA NPs synthesized through micro-emulsion. The main concern in this technique remains the removal of surfactants from the nanoparticles upon synthesis.

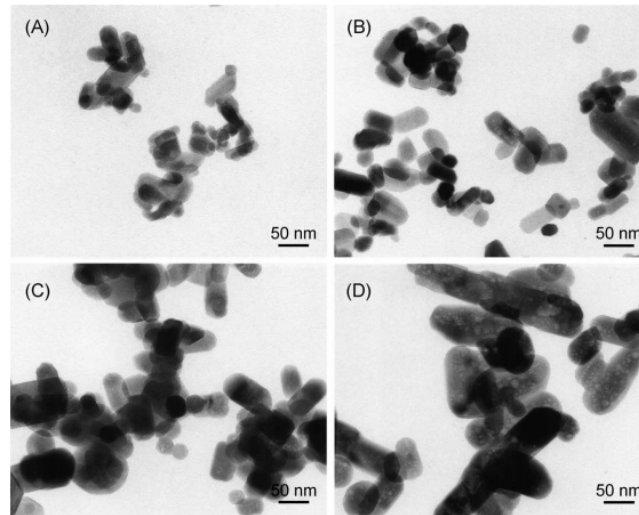


Figure 2.8 TEM micrographs of HA nanoparticles synthesized in emulsion: at (A) 25 °C, (B) 35 °C, (C) 50 °C, (D) 70 °C ¹³⁸.

2.4 Biomineralization

Regardless of the constant effort of mankind to develop more sophisticated yet functional biomaterials (refer to the preceding section), nature constantly teaches us that it is possible to produce minerals with beautiful morphologies and far greater functionality if we allow living systems to do so. Biominerals are minerals produced by living organisms and the process of mineral formation is called biomineralization. Typical examples of biominerals are apatite in bones and teeth of mammals, calcium carbonate (CaCO_3) in shells, amorphous silica (SiO_2) in marine sponges, and magnetite (Fe_3O_4) in chiton teeth¹³⁹. Figure 2.9 displays the example of a coccolithophore which is an algal plant that produces exoskeletons (coccospheres) consisting of a collection of minute calcite plates, called coccoliths¹⁴⁰.

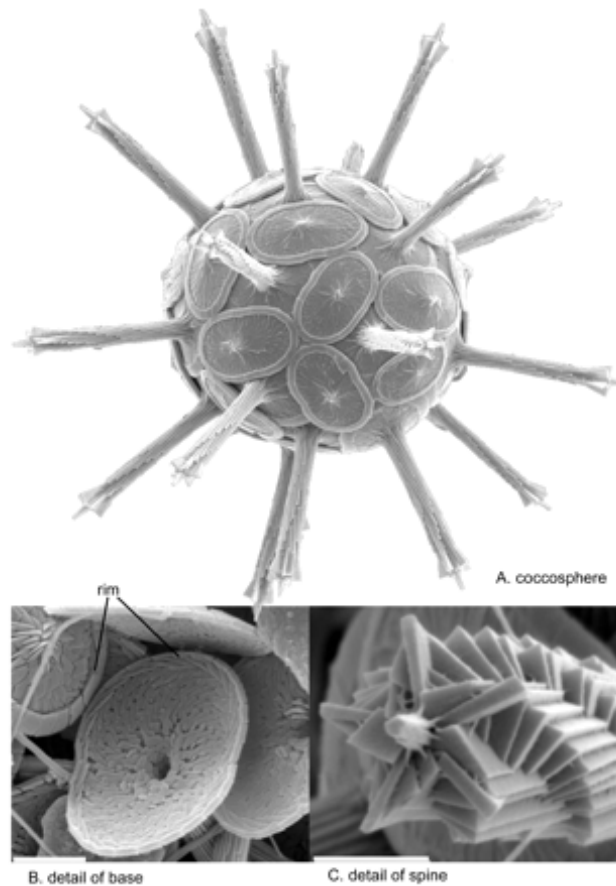


Figure 2.9 Coccospere with close-ups of (B) composite plates and (C) spines. Scale bars = 1 micron¹⁴⁰.

Biom mineralization processes have very unique features:

- They use very **common and abundant elements** from the earth's crust such as silicon, oxide, Ca, Fe, carbonate, phosphate *etc.*
- Synthesis is often carried out under very **mild conditions** such as near-neutral pH and ambient temperature^{141,142}.
- There is **no time constraint**: the precise morphology/functionality of biom minerals is acquired through years of evolution.
- There is however a key ingredient in biom mineralization processes: the involvement of **organic molecules** as soluble molecules or rigid templates¹⁴³⁻¹⁴⁶.

Without the help of organic molecules becomes impossible for living systems to form biominerals. Biomineralization processes usually occur in confined reaction environments which are constructed by biomolecules—of polymeric nature. A typical example of confined crystal growth is the case of magnetotactic bacteria. In Figure 2.10 it can be seen that magnetite crystals by growing in magnetosome vesicles adopt the final morphology of the vesicle. There are other examples in nature where insoluble biomolecule such as collagen and chitin, exert a “template effect” during biomineralization. In the particular case of bone formation, collagen is used as a template to direct apatite deposition to form oriented biominerals. However, the mineralization event itself is also highly controlled by soluble biomolecules (such as small and highly acidic non-collagenous proteins, NCPs). During the process of biomineralization, these soluble biomolecules seem to control the nucleation, crystal growth, polymorphism and the orientation of the inorganic minerals¹⁴⁷.

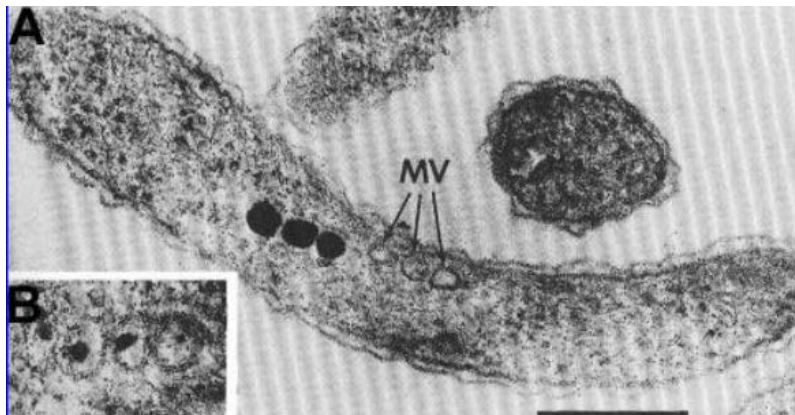


Figure 2.10 Section through a magnetotactic bacterial cell showing (A) three mature magnetite crystals and three empty magnetosome vesicles (MV); (B) vesicles containing immature magnetite particles. Scale bar = 250 nm¹⁴⁸.

The ability of nature to sculpture beautiful and functional biominerals seems to escape from the classical crystallization laws. Thus, single calcite crystals synthesized in the laboratory bear no resemblance with the calcite biomineral formed by echinoderms (Figure 2.11) that exhibit a very complicated but organized, repeating crystal pattern¹⁴¹.

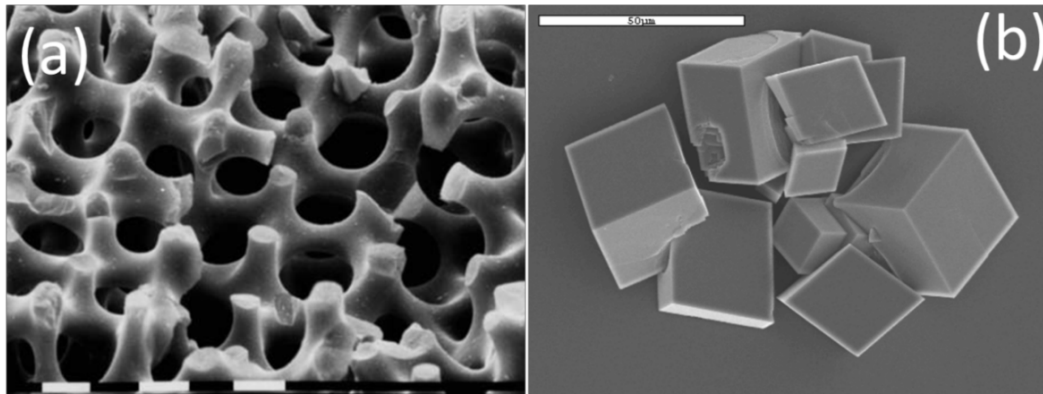


Figure 2.11 Comparison of calcite single crystals: **(a)** stereom of echinoderm and **(b)** synthetically produced rhombohedral forms¹⁴¹.

The great power that organic molecules exert in biomineralization processes has attracted much attention and many studies are being performed with the aim of fabricating new functional materials having more elaborated structures for medical and industrial purposes. In the following sections, it will be briefly discussed the crystallization pathways that underline biomineralization processes not only for understanding the mechanisms behind, but also for applying them to the synthesis of the next-generation of inorganic materials.

2.4.1 Crystal growth in biomineralization processes

2.4.1.1. Classical versus non-classical precipitation

To understand biomineralization processes it is important to recall the basics of crystallization and the differences between *classical* and *non-classical precipitation* processes -being this later one the preferred pathway for the precipitation of many biominerals.

Crystallization usually starts from ions in the case of inorganic minerals or molecules. These primary building units form clusters, which can grow or disintegrate till they eventually reach the so-called critical crystal nucleus, which is the smallest crystalline unit capable of further growing. The so-formed primary nanoparticles grow further *via* layer-by-layer adsorption of atoms or molecules onto an existing crystal face to finally form a single crystal (Figure 2.12a). Thus the final morphology of the crystal often becomes a reflection of the unit cell structure

that has simply grown propagating in the three dimensions. This growth process is called *classical crystallization*.

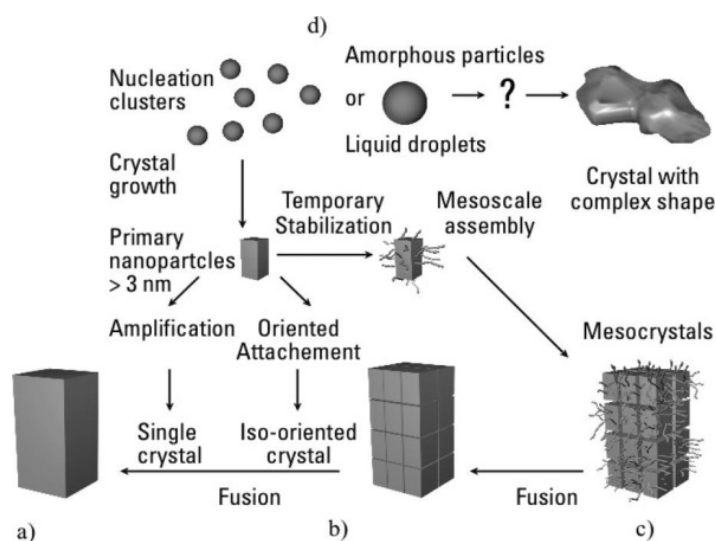


Figure 2.12 Schematic representation of classical and non-classical crystallization. (a) Classical crystallization pathway, (b) oriented attachment of primary nanoparticles forming an iso-oriented crystal upon fusing, (c) mesocrystal formation *via* self-assembly of primary nanoparticles covered with organics. Note: Mesocrystals can even form from pure nanoparticles. There is also the possibility that amorphous particles are formed, which can transform before or after their assembly to complicated morphologies (symbolized by the question mark in path d)¹⁴⁸.

The *non-classical precipitation* process relies instead in the self-assembly of nanoparticles rather than on the layer-by-layer adsorption of atoms in an already existing crystal surface¹⁴⁹. Via self-assembly a wide range of morphologies can be formed not necessarily resembling typical crystal precipitated by the classical precipitation pathway. Some examples of *non-classical precipitation* are also shown in Figure 2.12:

- Oriented attachment: this occurs when nanoparticles self-assemble in a way that they adopt a mutual orientation in crystallographic register, thus fusing together eliminating two neighbouring crystal surfaces (Figure 2.12b)¹⁴⁸.
- Mesoscale assembly: when the primary nanoparticles are coated with organic additives, they can form mesocrystals *via* mesoscale assembly

(Figure 2.12c). Mesocrystals can also transform into single crystals by fusion if the nanoparticles are not sufficiently stabilized by the additives. This makes mesocrystals very difficult to distinguish from classically precipitated crystals. The mesocrystal concept is nowadays been used to explain the formation of many minerals grown through bioinspired mineralization processes^{150,151}.

Non-classical precipitation pathways also encompass those crystallization processes that occur via formation of intermediate amorphous phases (Figure 2.12d). Amorphous minerals are the material of choice for many of the most morphologically exotic biominerals, such as the siliceous diatoms and radiolaria. With no preferred form, an amorphous material can be readily molded to give the desired product shape¹⁴⁸.

2.4.1.2. Thermodynamic versus kinetic precipitation pathway

Classical crystallization is usually under thermodynamic control which consists of one-step route from initial ions in solution to the final crystal formation (Figure 2.13A)^{148,152}. To achieve thermodynamic control in a crystallization reaction, a low supersaturation of the solution has to be maintained to avoid polynucleation. When controlling crystal morphologies using additives under a thermodynamic regime, it is important to use low concentration of additives, as high additive concentrations will lead to a surface coverage of the growing nucleus and, therefore, a quenching of its growth.

However, thermodynamic pathway is not very well suited to describe the crystallization process observed in biomineralization as well as in biomimetic mineralization. Instead, it can be stated that these systems are usually far from equilibrium so that kinetic-controlled crystallization (Figure 2.13B) prevails over thermodynamic-controlled crystallization during biomineralization. Therefore it is still almost impossible to predict the morphology of a crystal of biominerals with the currently existing thermodynamic equilibrium models¹⁵³.

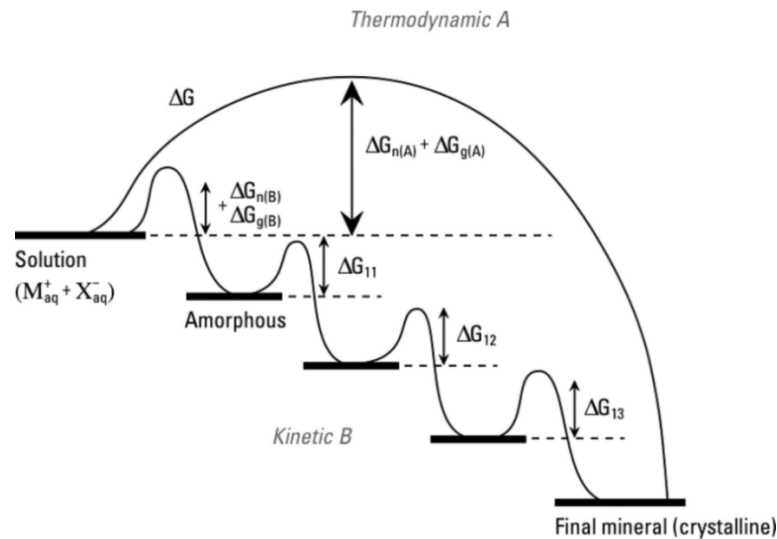


Figure 2.13 Crystallization pathways under thermodynamic and kinetic control. Whether a system follows a one-step route to the final mineral phase (pathway A) or proceeds by sequential precipitation (pathway B), depends on the free energy of activation (ΔG) associated with nucleation, growth, and phase transformation. Amorphous phases are common under kinetic conditions¹⁴⁸.

Crystallization under kinetic control is based predominantly on the modification of the activation-energy barriers on nucleation, growth and phase transformation. It is described as a sequential process that involves amorphous precursors and crystalline intermediates phases (Figure 2.13B). The initial amorphous phase during kinetic-controlled crystallization process is usually nonstoichiometric, hydrated, and, unless it is stabilized, it would transform into more stable phases rapidly. Phase transformation between a series of intermediates depends on the minerals' solubility and the free energies of activation of their inter-conversions in various environments¹⁴⁸. Kinetic control of crystallization is achieved in a high supersaturated solution, such that many crystal nuclei form simultaneously promoting a rapid particle nucleation of the kinetically favoured crystal modification. Kinetic control of crystallization can also be achieved by modifying the interactions of nuclei and developing crystals with solid surfaces and soluble molecules, which could influence the structure and composition of the nuclei, particle size, aggregation, and stability of intermediate phases¹⁵⁴. The unusual shapes of many biominerals and their often amorphous nature are an indication that crystallization *via* kinetic pathways is common in biomineralization processes.

2.4.2 Organic molecules in CaP mineralization

Synthetic polymers have been widely used to regulate the bio-inspired synthesis of CaP^{155–158}, inspired by the known roles of many biomolecules in biomineralization. The principle of controlled mineralization in the presence of a soluble polymer is entirely different from the template effect provided by the pre-designed artificial polymer matrices and relies on a synergistic effect of the mutual interactions between functionalities of the polymers and inorganic species in aqueous solution. In the following sections, using small organic molecules (i.e. surfactants), homopolymers and specialized block copolymers—double hydrophilic block copolymers (DHBCs) to regulate crystallization of CaP will be reviewed.

2.4.2.1 Surfactants

Surfactants are amphiphilic molecules which contain hydrophilic (ionic head group) and hydrophobic (tail) parts. Surfactants usually exhibit a specific behavior in aqueous solutions. At low concentrations surfactants can adsorb at various interfaces to reduce their free energy while at higher concentrations surfactants self-assemble into supramolecular aggregates such as micelles and vesicles when all available interfaces are filled. The surfactant concentration at which aggregation starts is called critical micelle concentration (cmc). Owing to their ready availability in many different designs, surfactants are often used as ideal model systems for the investigation of the effect of organic molecules on the formation of inorganic minerals¹³⁰.

The abilities of surfactants to affect CaP crystallization by promoting or inhibiting crystal growth and aggregation have been studied extensively. For example, Bujan and co-workers introduced single-chained sodium η -dodecyl sulfate (SDS) and asymmetric double-chained sodium bis(2-ethylhexyl) sulfosuccinate (AOT) into dibasic calcium phosphate dihydrate (DCPD) precipitation system, respectively¹⁵⁹. They showed that when the concentration of surfactant was below the cmc crystal growth was inhibited and crystal morphology also changed due to the surfactant anions being absorbed on lateral crystal faces. If the concentration was above the cmc, SDS and AOT induced the precipitation of a mixture of DCPD and octacalcium

phosphate. Nobuaki *et al.* synthesized meso-structural CaPs using palmitic and N-lauroyl-L-glutamic acids as anionic surfactants and 4-dodecyldiethylenetriamine as a cationic surfactant in a mixed solvent system of ethanol and water. They proposed that the most important aspect for the formation of mesostructured calcium phosphate was the interaction of carboxyl and primary amino groups of the surfactants with the inorganic species¹⁶⁰.

2.4.2.2 Homopolymers

Homopolymers are a naturally simple choice from the toolbox of synthetic polymers, as many homopolymers e.g. poly(acrylic acid) and poly(aspartic acid) are commercially available and are also easily synthesized in the laboratory. These polymers can not only be used as stabilizing agents for inorganic colloids, but also as structure-directing agents to control crystal growth.

Bigi *et al.* performed the structural and morphological investigation on OCP that was synthesized from aqueous solution in the presence of different concentrations of sodium polyacrylate^{161,162} and it was reported to reduce the nucleation efficiency of OCP. They also investigated the effect of poly (acrylic acid) (PAA) on the crystallinity and morphology of HA crystals and the results demonstrated that the dimensions of the crystals were reduced as PAA content increased. Furthermore, the morphology of HA crystals changed from plate-like to acicular, probably as a result of the adsorption of carboxylate-rich molecules on the hydrated layer of the OCP face¹⁶³. Liou *et al.*¹⁶⁴ manipulated apatite-PAA composites which had needle-like or nano-sphere structure showing that the PAA was successfully acting as a structural-directing agent upon the synthesis of the HA nanoparticles.

Since poly (amino acid)s can be synthesized resembling the acidic proteins often found in bone, poly (amino acid)s have been used to investigate mineralization of CaP from aqueous solution¹⁵⁵. For example, Bigi *et al.* have synthesized HA in the presence of poly (aspartic acid) and observed that the crystallinity of HA decreased and particle morphology became longer and thinner¹⁶¹. In addition, Furedi *et al.*¹⁶⁶ explored the influence of poly-L-lysine, and poly-L-glutamic acid on the formation

and phase transformation of amorphous calcium phosphate and all these poly (amino acid)s inhibited growth of the crystalline phase in a nonspecific way. Gower *et al.*¹⁶⁷ used poly-L-aspartic acid, poly-L-glutamic acid as the directing agents to mimic acidic non-collagenous proteins associated with bone formation. They found that the combination of these poly (amino acid)s can form amorphous precursor phase having liquid-like characteristics in solution. Due to their high fluidity, these precursors have been observed to penetrate the interstices of collagen fibrils and yielded nano-structured composites with a very high mineral content.

2.4.2.3 Copolymers

Besides homopolymers, copolymers with complex architectures have also been investigated for calcium phosphate mineralization. Among them, double hydrophilic block copolymers (DHBCs) are probably the most effective polymers used in the control of crystallization of polycrystalline minerals for mineralization purposes¹⁶⁸. These polymers are designed by inspiration of known active proteins involved in biomineralization and contain parts consisting of acidic or basic amino acid units which are commonly believed to interact with a mineral surface, and other parts consisting of hydrophilic amino acid residues which keep the protein dissolved in the aqueous environment in which biomineralization occurs. Thus, DHBC consists of two blocks: one hydrophilic block designed to interact with inorganic minerals and surfaces, and another hydrophilic block that keeps the polymer soluble. DHBCs turn out to be extraordinarily effective for controlling the crystallization of inorganic minerals in comparison with homopolymers, and have shown remarkable effects in synthesis, stabilization, and crystallization of various inorganic or inorganic-organic hybrids. The interactions of DHBCs with mineral surfaces offer many possibilities for particle stabilization and/or self-assembly, are schematically presented in Figure 2.14.

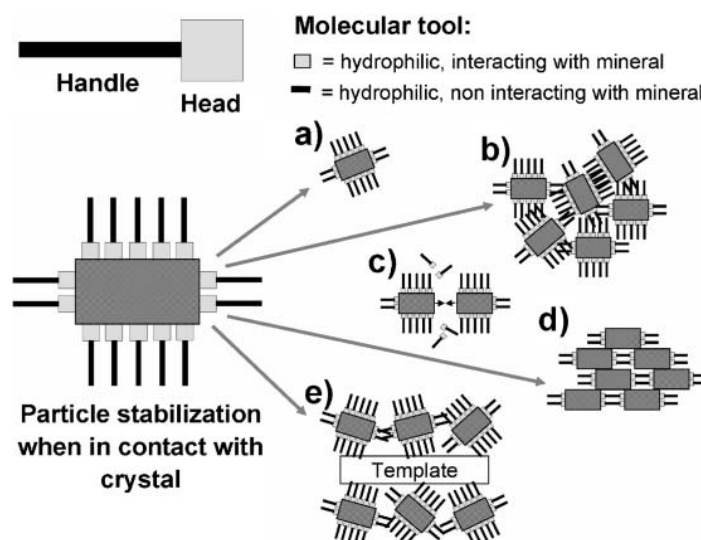


Figure 2.14 Concept of DHBCs, their interaction with mineral surfaces, and possibilities for particle stabilization or self-assembly. (a) either steric particle stabilization or only temporary steric nanoparticle stabilization can be achieved by tailoring the block length of a DHBC. DHBC stabilized nanoparticles can self-assemble by (b) unordered nanoparticle aggregation; (c) oriented attachment of nanoparticles by displacement or face-selective adsorption; (d) ordered, programmed self-assembly by face-selective adsorption; or (e) arrangement of temporarily stabilized nanoparticles around a template¹⁵³.

Either steric stabilization of large particles (Figure 2.14a) or temporary steric stabilization of nanoparticles can be achieved by tailoring the block length of the stabilizing block, leading to the formation of nanoparticle building blocks for constructing complex architectures. There are several modes for the self-assembled nanoparticles as shown in Figure 2.14b–e: disordered nanoparticle aggregation (Figure 2.14b); oriented attachment of nanoparticles by DHBC displacement or face-selective DHBC adsorption (Figure 2.14c); ordered and programmed self-assembly by face-selective DHBC adsorption (Figure 2.14d); or arrangement of temporarily stabilized nanoparticles around a template (Figure 2.14e).¹⁵³

For example, Antonietti and co-workers employed poly(ethylene oxide)-block-alkylated poly(methacrylic acid) (PEO-*b*-PMAA-*C*₁₂) as additive to synthesize calcium phosphates materials¹⁶⁹. The structural formula for the DHBC polymer employed in their study is shown in Figure 2.15.

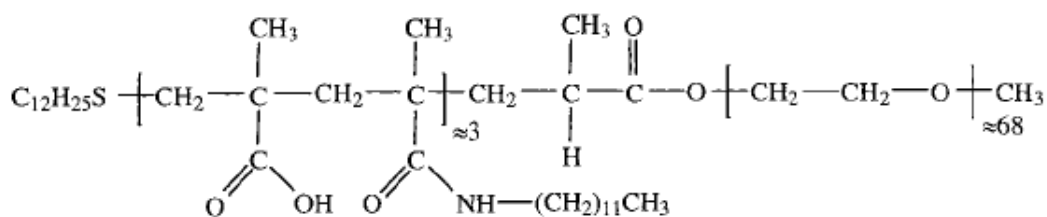


Figure 2.15 structural formula of PEO-b-PMAA-C₁₂

This polymer with functional carboxyl-groups in the immediate neighbourhood of the hydrophobic chains is special in the way that the three hydrophobic chains attached to the functional methacrylic acid block induce a weak aggregate formation. These aggregates sequester Ca²⁺ ions and thus serve as localized mineralization centers. Through controlling the pH of the Ca²⁺-loaded polymer solution and thus the crystal modification, interconnected CaP nano-filaments with neuron-like structure and more complex nested forms were created as shown in Figure 2.16.

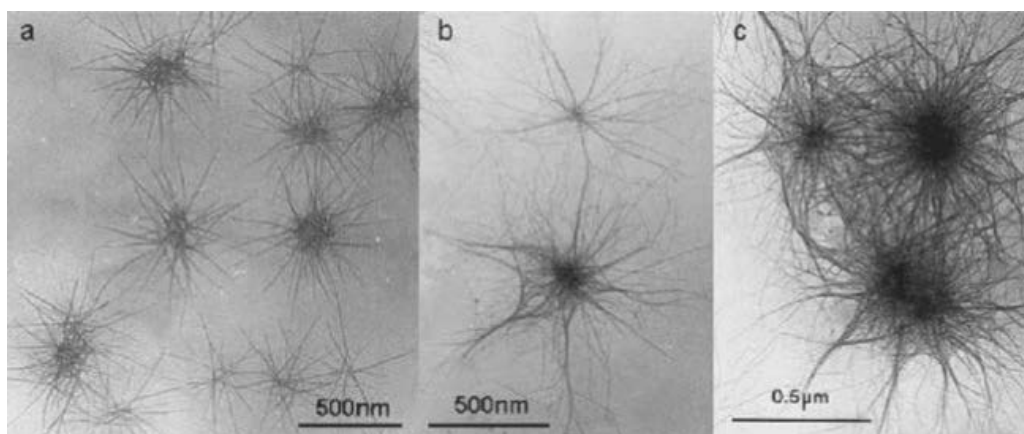


Figure 2.16 TEM images of calcium phosphate block copolymer nested colloids. (a) Star-like form at an early stage at pH 4.5; (b) later stage showing a complex central core, and very long and thin (2-3 nm) filaments; (c) neuron-like tangles produced at pH 5¹⁶⁹.

The similar structure were replicated by Tjandra and co-workers using a similar design of DHBC (PEO-block-PMAA) but with a longer PMAA chain¹⁷⁰. They believed that the neuron-like particles represent the early stages in the development of the complex architecture, and with time, the filaments become interconnected to give extended neural network structures. Although this structure has been reported several times in the literature, their crystal structure and chemical composition

have not been assessed. To establish the understanding of formation mechanisms of this unique structure, Junginger *et al.*¹⁷¹ detected crystal structures and chemical compositions of the fibers using a couple of techniques such as scanning transmission electron microscopy and energy-filtered transmission electron microscopy. They proposed that the fibers were crystalline calcium phosphate and they were not a single phase material.

The above specific example of complex neuron-like structure directed by DHBCs provide much inspiration toward designing new DHBCs for the synthesis of more advanced materials with novel structures and complexity. In this way, not only will a better understanding of the biominerals be achieved but also sophisticated materials with useful properties and functionalities can be created.

2.5 References

1. Dorozhkin, S. V. Calcium orthophosphates. *Journal of Materials Science* **42**, 1061–1095 (2007).
2. Dorozhkin, S. V. Calcium Orthophosphates in Nature, Biology and Medicine. *Materials* **2**, 399–498 (2009).
3. Wang, L. & Nancollas, G. H. Calcium orthophosphates: crystallization and dissolution. *Chemical reviews* **108**, 4628–69 (2008).
4. Bohner, M. Calcium orthophosphates in medicine : from ceramics to calcium phosphate cements. *Injury, Int. J. Care Injured* **31**, 37 (2000).
5. Boanini, E., Gazzano, M. & Bigi, a Ionic substitutions in calcium phosphates synthesized at low temperature. *Acta biomaterialia* **6**, 1882–94 (2010).
6. Dorozhkin, S. V & Epple, M. Biological and Medical Significance of Calcium Phosphates. *Angew. Chem. Int. Ed.* **41**, 3130–3146 (2002).
7. Brown, P. W. & Fulmer, M. Kinetics of Hydroxyapatite Formation at low Temperature. *J. Am. Ceram. Soc.* **40**, 934–940 (1991).
8. Johnsson, M. S. & Nancollas, G. H. The Role of Brushite and Octacalcium Phosphate in Apatite Formation. *Critical Reviews in Oral Biology and Medicine* **3**, 61–82 (1992).
9. Wang, L. & Nancollas, G. H. Pathways to biomineralization and biodemineralization of calcium phosphates: the thermodynamic and kinetic controls. *Dalton transactions* 2665–72 (2009).
10. Wang, L., Lu, J., Xu, F. & Zhang, F. Dynamics of crystallization and dissolution of calcium orthophosphates at the near-molecular level. *Chinese Science Bulletin* **56**, 713–721 (2011).

11. Procter, T., Company, G., Laboratories, M. V. & Hampshire, N. Hydroxyapatite Formation from a Hydrated Calcium Monohydrogen Phosphate Precursor. *Calc. Tiss. Res.* **342**, 335–342 (1971).
12. Dorozhkin, S. V Amorphous calcium (ortho)phosphates. *Acta biomaterialia* **6**, 4457–75 (2010).
13. Combes, C. & Rey, C. Amorphous calcium phosphates: synthesis, properties and uses in biomaterials. *Acta biomaterialia* **6**, 3362–78 (2010).
14. Hwang, E. T., Tatavarty, R., Chung, J. & Gu, M. B. New functional amorphous calcium phosphate nanocomposites by enzyme-assisted biomineralization. *ACS applied materials & interfaces* **5**, 532–7 (2013).
15. Tao, J. *et al.* Evolution of Amorphous Calcium Phosphate to Hydroxyapatite Probed by Gold Nanoparticles. *Journal of Physical Chemistry C* **112**, 14929–14933 (2008).
16. Li, Y. & Weng, W. In vitro synthesis and characterization of amorphous calcium phosphates with various Ca/P atomic ratios. *Journal of materials science. Materials in medicine* **18**, 2303–8 (2007).
17. Grynopas, M. D. & Omelon, S. Transient precursor strategy or very small biological apatite crystals? *Bone* **41**, 162–4 (2007).
18. Mahamid, J. *et al.* Mapping amorphous calcium phosphate transformation into crystalline mineral from the cell to the bone in zebrafish fin rays. *Proceedings of the National Academy of Sciences of the United States of America* **107**, 6316–21 (2010).
19. Mahamid, J., Sharir, A., Addadi, L. & Weiner, S. Amorphous calcium phosphate is a major component of the forming fin bones of zebrafish: Indications for an amorphous precursor phase. *PNAS* **105**, 12748–12753 (2008).
20. *Hydroxyapatite (HAp) for Biomedical Applications.* (Elsevier: 2015).

21. Xia, L. *et al.* Enhanced osteogenesis through nano-structured surface design of macroporous hydroxyapatite bioceramic scaffolds via activation of ERK and p38 MAPK signaling pathways. *Journal of Materials Chemistry B* **1**, 5403–5403 (2013).
22. Flautre, B., Descamps, M., Delecourt, C. & Blary, M. C. Porous HA ceramic for bone replacement: Role of the pores and interconnections-experimental study in the rabbit. *Journal of Materials Science: Materials in Medicine* **12**, 679–682 (2001).
23. Yuan, H., Groot, K. D. E. & Sa, I. Calcium phosphate biomaterials: an overview. *NATO Science Series II: Mathematics, Physics and Chemistry* **171**, 37–57 (2005).
24. Yoshikawa, H., Tamai, N., Murase, T. & Myoui, A. Interconnected porous hydroxyapatite ceramics for bone tissue engineering. *Journal of the Royal Society, Interface* **6 Suppl 3**, S341–8 (2009).
25. Mendelson, B. C., Jacobson, S. R., Lavoipierre, A. M. & Huggins, R. J. The fate of porous hydroxyapatite granules used in facial skeletal augmentation. *Aesthetic plastic surgery* **34**, 455–61 (2010).
26. Morita, S., Furuya, K., Ishihara, K. & Nakabayashi, N. Performance of adhesive bone cement containing hydroxyapatite particles. *Biomaterials* **19**, 1601–1606 (1998).
27. Ramay, H. R. & Zhang, M. Preparation of porous hydroxyapatite scaffolds by combination of the gel-casting and polymer sponge methods. *Biomaterials* **24**, 3293–3302 (2003).
28. Ong, J. L. & Chan, D. C. N. Hydroxyapatite and Their Use As Coatings in Dental Implants: A Review. *Critical Reviews™ in Biomedical Engineering* **28**, 667–707 (1999).

29. Rizzi, S. C. *et al.* Biodegradable polymer/hydroxyapatite composites : Surface analysis and initial attachment of human osteoblasts. *J Biomed Mater Res* **55**, 475–86. (2001).
30. Wang, T., Mitchell, J. W. & Engineering, C. Improve the Strength of PLA/HA Composite Through the Use of Surface Initiated Polymerization and Phosphonic Acid Coupling Agent. *J Res Natl Inst Stand Technol* **116**, 785–796 (2012).
31. Albano, C., Gonza, G. & Palacios, J. PLLA-HA vs . PLGA-HA Characterization and Comparative Analysis. *Polymer Composites* **34**, 1433–1442 (2013).
32. Uskoković, V. & Uskoković, D. P. Nanosized hydroxyapatite and other calcium phosphates: chemistry of formation and application as drug and gene delivery agents. *Journal of biomedical materials research. Part B, Applied biomaterials* **96**, 152–91 (2011).
33. Dorozhkin, S. V. Nanodimensional and Nanocrystalline Apatites and Other Calcium Orthophosphates in Biomedical Engineering, Biology and Medicine. *Materials* **2**, 1975–2045 (2009).
34. Loo, S. C. J., Moore, T., Banik, B. & Alexis, F. Biomedical applications of hydroxyapatite nanoparticles. *Current pharmaceutical biotechnology* **11**, 333–42 (2010).
35. Do, T. N. T., Lee, W.-H., Loo, C.-Y., Zavgorodniy, A. V & Rohanizadeh, R. Hydroxyapatite nanoparticles as vectors for gene delivery. *Therapeutic delivery* **3**, 623–32 (2012).
36. Wang, J. *et al.* Remineralization of dentin collagen by meta-stabilized amorphous calcium phosphate. *CrystEngComm* **15**, 6151–6158 (2013).
37. Sun, J. *et al.* Biomimetic promotion of dentin remineralization using l-glutamic acid: inspiration from biomineralization proteins. *Journal of Materials Chemistry B* **2**, 4544 (2014).

38. Ma, G. & Liu, X. Y. Hydroxyapatite : Hexagonal or Monoclinic? *Crystal Growth & Design* **9**, 2991–2994 (2009).
39. Koutsopoulos, S. Synthesis and characterization of hydroxyapatite crystals : A review study on the analytical methods. *J Biomed Mater Res* **62**, 31–34 (2002).
40. Currey, J. D. Role of collagen and other organics in the mechanical properties of bone. *Osteoporosis international* **14 Suppl 5**, S29–36 (2003).
41. Zhou, H. & Lee, J. Nanoscale hydroxyapatite particles for bone tissue engineering. *Acta biomaterialia* **7**, 2769–81 (2011).
42. Boskey, A. L. Mineralization of Bones and Teeth. *Elements* **3**, 387–393 (2007).
43. Rey, C., Combes, C., Drouet, C. & Glimcher, M. J. Bone mineral: update on chemical composition and structure. *Osteoporosis International* **20**, 1013–1021 (2009).
44. Landi, E., Celotti, G., Logroscino, G. & Tampieri, a. Carbonated hydroxyapatite as bone substitute. *Journal of the European Ceramic Society* **23**, 2931–2937 (2003).
45. Lec-eros, R. Z. Apatites in biological systems. *Prog. Cryatal Growth Charact.* **4**, 3535 (1980).
46. Liu, Q., Huang, S., Matinlinna, J. P., Chen, Z. & Pan, H. Insight into Biological Apatite : Physiochemical Properties and Preparation Approaches. *BioMed Research International* **2013**, 1–13 (2013).
47. Boskey, a L. & Coleman, R. Aging and bone. *Journal of dental research* **89**, 1333–48 (2010).
48. Bigi, a *et al.* The role of magnesium on the structure of biological apatites. *Calcified tissue international* **50**, 439–44 (1992).

49. Landi, E. *et al.* Biomimetic Mg-substituted hydroxyapatite: from synthesis to in vivo behaviour. *Journal of materials science. Materials in medicine* **19**, 239–47 (2008).
50. Reginster, J. Y. *et al.* Long-term treatment of postmenopausal osteoporosis with strontium ranelate: results at 8 years. *Bone* **45**, 1059–64 (2009).
51. Pors Nielsen, S. The biological role of strontium. *Bone* **35**, 583–8 (2004).
52. Boanini, E., Torricelli, P., Fini, M. & Bigi, a Osteopenic bone cell response to strontium-substituted hydroxyapatite. *Journal of materials science. Materials in medicine* **22**, 2079–88 (2011).
53. Thian, E. S. *et al.* Zinc-substituted hydroxyapatite: a biomaterial with enhanced bioactivity and antibacterial properties. *Journal of materials science. Materials in medicine* **24**, 437–45 (2013).
54. Molokwu, C. O. Zinc Homeostasis and Bone Mineral Density. *Ohio Research and Clinical Review Fall* **15**, 7–15 (2006).
55. Shepherd, J. H., Shepherd, D. V & Best, S. M. Substituted hydroxyapatites for bone repair. *Journal of materials science. Materials in medicine* **23**, 2335–47 (2012).
56. Cox, S. C., Jamshidi, P., Grover, L. M. & Mallick, K. K. Preparation and characterisation of nanophase Sr, Mg, and Zn substituted hydroxyapatite by aqueous precipitation. *Materials Science and Engineering: C* **35**, 106–114 (2014).
57. Laurencin, D. *et al.* Magnesium incorporation into hydroxyapatite. *Biomaterials* **32**, 1826–37 (2011).
58. Ziani, S., Meski, S. & Khireddine, H. Characterization of Magnesium-Doped Hydroxyapatite Prepared by Sol-Gel Process. *International Journal of Applied Ceramic Technology* **11**, 83–91 (2014).

59. Pan, H. B. *et al.* Solubility of strontium-substituted apatite by solid titration. *Acta biomaterialia* **5**, 1678–85 (2009).
60. Li, Y., Nam, C. T. & Ooi, C. P. Iron(III) and manganese(II) substituted hydroxyapatite nanoparticles: Characterization and cytotoxicity analysis. *Journal of Physics: Conference Series* **187**, 012024 (2009).
61. GRANDJEAN-LAQUERRIERE Alexia Influence of the zinc concentration of zinc substituted hydroxyapatite on cytokines production by human monocytes in vitro. *Biomaterials* **27**, 3195–3200 (2006).
62. Russo, L. *et al.* Carbonate hydroxyapatite functionalization : a comparative study towards (bio) molecules fixation. *Interface Focus* **4**, 1–7 (2014).
63. Balas, F., Pérez-Pariente, J. & Vallet-Regí, M. In vitro bioactivity of silicon-substituted hydroxyapatites. *Journal of biomedical materials research. Part A* **66**, 364–75 (2003).
64. Aina, V. *et al.* Magnesium- and strontium-co-substituted hydroxyapatite: the effects of doped-ions on the structure and chemico-physical properties. *Journal of materials science: Materials in medicine* **23**, 2867–2879 (2012).
65. Iafisco, M., Ruffini, A., Adamiano, A., Sprio, S. & Tampieri, A. Biomimetic magnesium–carbonate-apatite nanocrystals endowed with strontium ions as anti-osteoporotic trigger. *Materials Science and Engineering C* **35**, 212–219 (2014).
66. Landi, E., Sprio, S., Sandri, M., Celotti, G. & Tampieri, A. Development of Sr and CO₃ co-substituted hydroxyapatites for biomedical applications. *Acta biomaterialia* **4**, 656–63 (2008).
67. Sprio, S. *et al.* Physico-chemical properties and solubility behaviour of multi-substituted hydroxyapatite powders containing silicon. *Materials Science and Engineering: C* **28**, 179–187 (2008).

68. Gibson, I. R. & Bonfield, W. Novel synthesis and characterization of an AB-type carbonate-substituted hydroxyapatite. (2001).doi:10.1002/jbm.10044
69. Ziani, S., Meski, S. & Khireddine, H. Characterization of Magnesium-Doped Hydroxyapatite Prepared by Sol-Gel Process. *International Journal of Applied Ceramic Technology* **11**, 83–91 (2014).
70. Gibson, I. R., Best, S. M. & Bonfield, W. Chemical characterization of silicon-substituted hydroxyapatite. *Journal of biomedical materials research* **44**, 422–428 (1999).
71. Patel, N. *et al.* A comparative study on the in vivo behavior of hydroxyapatite and silicon substituted hydroxyapatite granules. *Journal of Materials Science: Materials in Medicine* **13**, 1199–1206 (2002).
72. Aina, V. *et al.* Sr-containing hydroxyapatite: morphologies of HA crystals and bioactivity on osteoblast cells. *Materials science & engineering. C, Materials for biological applications* **33**, 1132–42 (2013).
73. Del Valle, L. J. *et al.* DNA adsorbed on hydroxyapatite surfaces. *J. Mater. Chem. B* **2**, 6953–6966 (2014).
74. Iafisco, M. *et al.* Cell surface receptor targeted biomimetic apatite nanocrystals for cancer therapy. *Small* **9**, 3834–44 (2013).
75. Isaac Rodríguez-Ruiz pH-Responsive Delivery of Doxorubicin from Citrate–Apatite nanocrystals with tailored carbonate content. *Langmuir* (2013).
76. Choi, H. S. *et al.* Renal clearance of quantum dots. *Nature biotechnology* **25**, 1165–70 (2007).
77. Foged, C., Brodin, B., Frokjaer, S. & Sundblad, A. Particle size and surface charge affect particle uptake by human dendritic cells in an in vitro model. *International Journal of Pharmaceutics* **298**, 315–322 (2005).

78. Decuzzi, P. *et al.* Size and shape effects in the biodistribution of intravascularly injected particles. *Journal of controlled release: official journal of the Controlled Release Society* **141**, 320–7 (2010).
79. Duan, X. & Li, Y. Physicochemical characteristics of nanoparticles affect circulation, biodistribution, cellular internalization, and trafficking. *Small* **9**, 1521–32 (2013).
80. Shang, L., Nienhaus, K. & Nienhaus, G. U. Engineered nanoparticles interacting with cells: size matters. *Journal of nanobiotechnology* **12**, 5 (2014).
81. Fröhlich, E. The role of surface charge in cellular uptake and cytotoxicity of medical nanoparticles. *International journal of nanomedicine* **7**, 5577–91 (2012).
82. Chen, L., Mccrate, J. M., Lee, J. C.-M. & Li, H. The role of surface charge on the uptake and biocompatibility of hydroxyapatite nanoparticles with osteoblast cells. *Nanotechnology* **22**, 105708 (2011).
83. Harvey, S. Polymer Particle Shape Independently Influences Binding and Internalization by Macrophages. *J Control Release. 2010* **147**, 408–412 (2010).
84. Huang, X., Teng, X., Chen, D., Tang, F. & He, J. The effect of the shape of mesoporous silica nanoparticles on cellular uptake and cell function. *Biomaterials* **31**, 438–448 (2010).
85. Verma, I. M. & Somia, N. Gene therapy –promises , problems and prospects. *Nature* **389**, 239–242 (1997).
86. Zhang, H., Lee, M., Hogg, M. G., Dordick, J. S. & Sharfstein, S. T. Gene Delivery in Three- Dimensional Nanoparticles. *ACS nano* **4**, 4733–4743 (2010).

87. Jin, L., Zeng, X., Liu, M., Deng, Y. & He, N. Current progress in gene delivery technology based on chemical methods and nano-carriers. *Theranostics* **4**, 240–55 (2014).
88. Luo, D. & Saltzman, W. M. Synthetic DNA delivery systems. *Nature biotechnology* **18**, 33–37 (2000).
89. El-Aneid, A. An overview of current delivery systems in cancer gene therapy. *Journal of Controlled Release* **94**, 1–14 (2004).
90. Ibraheem, D., Elaissari, A. & Fessi, H. Gene therapy and DNA delivery systems. *International journal of pharmaceutics* **459**, 70–83 (2014).
91. Varkouhi, A. K., Scholte, M., Storm, G. & Haisma, H. J. Endosomal escape pathways for delivery of biologicals. *Journal of controlled release : official journal of the Controlled Release Society* **151**, 220–8 (2011).
92. Guo, X. & Huang, L. Recent advances in nonviral vectors for gene delivery. *Accounts of chemical research* **45**, 971–9 (2012).
93. Green, J. J., Langer, R. & Anderson, D. G. Yields Insight into Nonviral Gene Delivery. **41**, (2008).
94. Robbins, P. D. & Ghivizzani, S. C. Viral Vectors for Gene Therapy. *Pharmacol. Ther.* **80**, 35–47 (1998).
95. Lundstrom, K. Latest development in viral vectors for gene therapy. *Trends in biotechnology* **21**, 117–22 (2003).
96. Godbey, W. T., Wu, K. K. & Mikos, A. G. Poly (ethylenimine) and its role in gene delivery. *Journal of Controlled Release* **60**, 149–160 (1999).
97. Kirtane, A. R. & Panyam, J. Polymer nanoparticles: Weighing up gene delivery. *Nature nanotechnology* **8**, 805–6 (2013).

98. Yeh, P.-H., Sun, J.-S., Wu, H.-C., Hwang, L.-H. & Wang, T.-W. Stimuli-responsive HA-PEI nanoparticles encapsulating endostatin plasmid for stem cell gene therapy. *RSC Advances* **3**, 12922 (2013).
99. Martin, B. *et al.* The design of cationic lipids for gene delivery. *Current pharmaceutical design* **11**, 375–94 (2005).
100. Malmsten, M. Inorganic nanomaterials as delivery systems for proteins, peptides, DNA, and siRNA. *Current Opinion in Colloid & Interface Science* **18**, 468–480 (2013).
101. Yeagle, L. Lipid regulation of cell membrane structure and function. *The FASEB Journal* **3**, 1833–1842 (1989).
102. Lv, H., Zhang, S., Wang, B., Cui, S. & Yan, J. Toxicity of cationic lipids and cationic polymers in gene delivery. *Journal of Controlled Release* **114**, 100–109 (2006).
103. Tonga, G. Y., Moyano, D. F., Kim, C. S. & Rotello, V. M. Inorganic nanoparticles for therapeutic delivery: Trials, tribulations and promise. *Current Opinion in Colloid & Interface Science* (2014).doi:10.1016/j.cocis.2014.03.004
104. Sokolova, V. & Epple, M. Inorganic nanoparticles as carriers of nucleic acids into cells. *Angewandte Chemie (International ed. in English)* **47**, 1382–95 (2008).
105. Bose, S. & Tarafder, S. Calcium phosphate ceramic systems in growth factor and drug delivery for bone tissue engineering: a review. *Acta biomaterialia* **8**, 1401–21 (2012).
106. Sadat-Shojai, M., Khorasani, M.-T., Dinpanah-Khoshdargi, E. & Jamshidi, A. Synthesis methods for nanosized hydroxyapatite with diverse structures. *Acta biomaterialia* **9**, 7591–621 (2013).

107. Maitra, A. Calcium phosphate nanoparticles: second-generation nonviral vectors in gene therapy. *Expert review of molecular diagnostics* **5**, 893–905 (2005).
108. Lee, M. A., Dunn, R. C., Clapham, D. E. & Stehno-bitte, L. Calcium regulation permeability of nuclear pore. *Cell Calcium* **23**, 91–101 (1998).
109. Zhu, S. H. *et al.* Hydroxyapatite Nanoparticles as a Novel Gene Carrier. *Journal of Nanoparticle Research* **6**, 307–311 (2004).
110. Bisht, S., Bhakta, G., Mitra, S. & Maitra, A. pDNA loaded calcium phosphate nanoparticles: highly efficient non-viral vector for gene delivery. *International journal of pharmaceutics* **288**, 157–68 (2005).
111. Zhao, R. *et al.* The anti-tumor effect of p53 gene-loaded hydroxyapatite nanoparticles in vitro and in vivo. *Journal of Nanoparticle Research* **16**, 2353 (2014).
112. Wu, G.-J. *et al.* Hydroxylapatite nanorods: an efficient and promising carrier for gene transfection. *Journal of colloid and interface science* **345**, 427–32 (2010).
113. Liong, M. *et al.* Multifunctional Inorganic Nanoparticles for Imaging, Targeting, and Drug Delivery. *ACS nano* **2**, 889–896 (2008).
114. Yan-Zhong, Z. *et al.* Characteristics of functionalized nano-hydroxyapatite and internalization by human epithelial cell. *Nanoscale research letters* **6**, 600 (2011).
115. Morgan, T. T. *et al.* Encapsulation of Organic Molecules in Calcium Phosphate Nanocomposite Particles for Intracellular Imaging and Drug Delivery. *Nano letters* **8**, 4108–4115 (2008).
116. Russin, T. J. *et al.* Near-Infrared Emitting Fluorophore-for In Vivo Imaging of Human Breast. *ACS nano* **2**, 2075–2084 (2008).

117. Williams, R. L. *et al.* Thiol modification of silicon-substituted hydroxyapatite nanocrystals facilitates fluorescent labelling and visualisation of cellular internalisation. *Journal of Materials Chemistry B* **1**, 4370–4379 (2013).
118. Wang, M. & Thanou, M. Targeting nanoparticles to cancer. *Pharmacological research* **62**, 90–9 (2010).
119. Palazzo, B. *et al.* Biomimetic Hydroxyapatite–Drug Nanocrystals as Potential Bone Substitutes with Antitumor Drug Delivery Properties. *Advanced Functional Materials* **17**, 2180–2188 (2007).
120. Yang, Y.-H., Liu, C.-H., Liang, Y.-H., Lin, F.-H. & Wu, K. C.-W. Hollow mesoporous hydroxyapatite nanoparticles (hmHANPs) with enhanced drug loading and pH-responsive release properties for intracellular drug delivery. *Journal of Materials Chemistry B* **1**, 2447–2450 (2013).
121. Dey, S., Das, M. & Balla, V. K. Effect of hydroxyapatite particle size, morphology and crystallinity on proliferation of colon cancer HCT116 cells. *Materials Science and Engineering: C* **39**, 336–339 (2014).
122. Liu, Z.-S., Tang, S.-L. & Ai, Z.-L. Effects of hydroxyapatite nanoparticles on proliferation and apoptosis of human hepatoma BEL-7402 cells. *World journal of gastroenterology : WJG* **9**, 1968–71 (2003).
123. Qing, F. *et al.* Selective effects of hydroxyapatite nanoparticles on osteosarcoma cells and osteoblasts. *Journal of materials science. Materials in medicine* **23**, 2245–51 (2012).
124. Hu, J., Liu, Z., Tang, S. & He, Y. Effect of hydroxyapatite nanoparticles on the growth and p53/c-Myc protein expression of implanted hepatic VX 2 tumor in rabbits by intravenous injection. *World journal of gastroenterology* **13**, 2798–2802 (2007).

125. Tang, W., Yuan, Y., Wu, Y. & Lu, X. Differential cytotoxicity and particle action of hydroxyapatite nanoparticles in human cancer cells. *Nanomedicine* **9**, 397–412 (2013).
126. Han, Y. *et al.* Different inhibitory effect and mechanism of hydroxyapatite nanoparticles on normal cells and cancer cells in vitro and in vivo. *Scientific reports* **4**, 7134 (2014).
127. Dogan, O. & Oner, M. Biomimetic mineralization of hydroxyapatite crystals on the copolymers of vinylphosphonic acid and 4-vinylimidazole. *Langmuir : the ACS journal of surfaces and colloids* **22**, 9671–5 (2006).
128. Cunniffe, G. M. *et al.* The synthesis and characterization of nanophase hydroxyapatite using a novel dispersant-aided precipitation method. *Journal of biomedical materials research. Part A* **95**, 1142–9 (2010).
129. Ferraz, M. P., Monteiro, F. J. & Manuel, C. M. Hydroxyapatite nanoparticles : A review of preparation methodologies. *Journal of Applied Biomaterials & Biomechanics* **2**, 74–80 (2004).
130. Sikirić, M. D. & Füredi-Milhofer, H. The influence of surface active molecules on the crystallization of biominerals in solution. *Advances in colloid and interface science* **128-130**, 135–158 (2006).
131. Afshar, A., Ghorbani, M., Ehsani, N., Saeri, M. . & Sorrell, C. . Some important factors in the wet precipitation process of hydroxyapatite. *Materials & Design* **24**, 197–202 (2003).
132. Loo, S. C. J., Siew, Y. E., Ho, S., Boey, F. Y. C. & Ma, J. Synthesis and hydrothermal treatment of nanostructured hydroxyapatite of controllable sizes. *Journal of materials science. Materials in medicine* **19**, 1389–97 (2008).
133. Manafi, S. & Rahimpour, M. R. Synthesis of Nanocrystalline Hydroxyapatite Nanorods via Hydrothermal Conditions. *Chemical Engineering & Technology* **34**, 972–976 (2011).

134. Yan, L., Li, Y., Deng, Z., Zhuang, J. & Sun, X. Surfactant-assisted hydrothermal synthesis of hydroxyapatite nanorods. *International Journal of Inorganic Materials* **3**, 633–637 (2001).
135. Sun, Y., Guo, G., Tao, D. & Wang, Z. Reverse microemulsion-directed synthesis of hydroxyapatite nanoparticles under hydrothermal conditions. *Journal of Physics and Chemistry of Solids* **68**, 373–377 (2007).
136. Bose, S. & Saha, S. K. Synthesis and Characterization of Hydroxyapatite Nanopowders by Emulsion Technique. *Chem. Mater.* **15**, 4464–4469 (2003).
137. Mésoscopiques, M. & Pierre, U. The role of soft colloidal templates in controlling the size and shape of inorganic nanocrystals. *Nature materials* **2**, 145–150 (2003).
138. Kensaku Sonoda, Tsutomu Furuzono, Dominic Walsh, Kimiyasu Sato, J. T. Influence of emulsion on crystal growth of hydroxyapatite. *Solid State Ionics* **151**, 321–327 (2002).
139. Arakaki, A. *et al.* Biom mineralization-inspired synthesis of functional organic/inorganic hybrid materials: organic molecular control of self-organization of hybrids. *Organic & biomolecular chemistry* **13**, 974–89 (2015).
140. Young, J. R. & Henriksen, K. Biom mineralization Within Vesicles : The Calcite of Coccoliths. *Reviews in mineralogy and geochemistry* **54**, 189–215 (2003).
141. Weiner, S., Israel, R., Dove, P. M., Tech, V. & Virginia, U. S. A. An Overview of Biom mineralization Processes and the Problem of the Vital Effect. *Reviews in mineralogy and geochemistry* **54**, 1–29 (2001).
142. Jiang, W. *et al.* Biomimetically triggered inorganic crystal transformation by biomolecules: a new understanding of biom mineralization. *The journal of physical chemistry. B* **113**, 10838–44 (2009).

143. Mann, S. Biomineralization: a novel approach to crystal engineering. *Endeavour* **15**, 120–125 (1991).
144. Estroff, L. a Introduction: Biomineralization. *Chemical reviews* **108**, 4329–31 (2008).
145. Nudelman, F. & Sommerdijk, N. a J. M. Biomineralization as an inspiration for materials chemistry. *Angewandte Chemie (International ed. in English)* **51**, 6582–96 (2012).
146. Mohammad Hafiz Uddin, Takuya Matsumoto, Masayuki Okazaki, A. N. and T. S. Biomimetic fabrication of apatite related biomaterials. *Biomimetics Learning from Nature* 289–305 (2008).
147. Nudelman, F., Bomans, P. H. H., George, A., De With, G. & Sommerdijk, N. a J. M. The role of the amorphous phase on the biomimetic mineralization of collagen. *Faraday Discussions* **159**, 357 (2012).
148. Meldrum, F. C. & Cölfen, H. Controlling mineral morphologies and structures in biological and synthetic systems. *Chemical reviews* **108**, 4332–4432 (2008).
149. Dove, P. M., Han, N. & Yoreo, J. J. De Mechanisms of classical crystal growth theory explain quartz and silicate dissolution behavior. *PNAS* **102**, 15357–15362 (2005).
150. Niederberger, M. & Cölfen, H. Oriented attachment and mesocrystals: non-classical crystallization mechanisms based on nanoparticle assembly. *Physical chemistry chemical physics : PCCP* **8**, 3271–87 (2006).
151. Cölfen, H. & Antonietti, M. Mesocrystals: inorganic superstructures made by highly parallel crystallization and controlled alignment. *Angewandte Chemie (International ed. in English)* **44**, 5576–91 (2005).

152. Cölfen, H. & Mann, S. Higher-order organization by mesoscale self-assembly and transformation of hybrid nanostructures. *Angewandte Chemie (International ed. in English)* **42**, 2350–65 (2003).
153. Xu, A.-W., Ma, Y. & Cölfen, H. Biomimetic mineralization. *Journal of Materials Chemistry* **17**, 415 (2007).
154. Gower, L. B. Biomimetic Model Systems for Investigating the Amorphous Precursor Pathway and Its Role in Biomineralization. *Chem. Rev.* **108**, 4551–4627 (2008).
155. Chi, C. *et al.* Biomineralization process of calcium phosphate: Modulation of the poly-amino acid with different hydroxyl/carboxyl ratios. *Materials Chemistry and Physics* **115**, 808–814 (2009).
156. Nonoyama, T., Ogasawara, H., Tanaka, M., Higuchi, M. & Kinoshita, T. Calcium phosphate biomineralization in peptide hydrogels for injectable bone-filling materials. *Soft Matter* **8**, 11531 (2012).
157. Bleek, K. & Taubert, A. New developments in polymer-controlled, bioinspired calcium phosphate mineralization from aqueous solution. *Acta biomaterialia* **9**, 6283–321 (2013).
158. Schweizer, S. & Taubert, A. Polymer-controlled, bio-inspired calcium phosphate mineralization from aqueous solution. *Macromolecular bioscience* **7**, 1085–99 (2007).
159. Filipovic, N. & Garti, N. Effect of Anionic Surfactants on Crystal Growth of Calcium Hydrogen Phosphate Dihydrate. *Langmuir* 6461–6470 (2001).
160. Ikawa, N., Hori, H., Kimura, T., Oumi, Y. & Sano, T. Templating route for mesostructured calcium phosphates with carboxylic acid-and amine-type surfactants. *Langmuir* **24**, 13113–13120 (2008).
161. A.Bigi Interaction of Sodium Polyacrylate with Octacalcium Phosphate. *Advances in crystal growth inhibition technologies* **17**, 29/41 (2000).

162. Bigi, A. *et al.* Synthesis and hydrolysis of octacalcium phosphate: effect of sodium polyacrylate. *Journal of Inorganic Biochemistry* **75**, 145–151 (1999).
163. Bertoni, E., Bigi, A., Falini, G., Panzavolta, S. & Roveri, N. Hydroxyapatite/polyacrylic acid nanocrystals. *J. Mater. Chem.* **9**, 779–782 (1999).
164. Liou, S.-C., Chen, S.-Y. & Liu, D.-M. Manipulation of nanoneedle and nanosphere apatite/poly(acrylic acid) nanocomposites. *Journal of biomedical materials research. Part B, Applied biomaterials* **73**, 117–22 (2005).
165. Bigi, A., Boanini, E., Gazzano, M., Kojdecki, M. a. & Rubini, K. Microstructural investigation of hydroxyapatite-polyelectrolyte composites. *Journal of Materials Chemistry* **14**, 274–279 (2004).
166. Pazit Bar-Yosef Ofir, Ruti Govrin-Lippman, Nissim Garti, and H. F.-M. The Influence of Polyelectrolytes on the Formation and Phase Transformation of Amorphous Calcium Phosphate. *Crystal Growth & Design* **4**, 177–183 (2004).
167. Jee, S.-S., Thula, T. T. & Gower, L. B. Development of bone-like composites via the polymer-induced liquid-precursor (PILP) process. Part 1: influence of polymer molecular weight. *Acta biomaterialia* **6**, 3676–86 (2010).
168. Colfen, H. Double-Hydrophilic Block Copolymers : Synthesis and Application as Novel Surfactants and Crystal Growth Modifiers. *Macromol. Rapid Commun.* **22**, 219–252 (2001).
169. Antonietti, M. *et al.* Inorganic/Organic Mesostructures with Complex Architectures: Precipitation of Calcium Phosphate in the Presence of Double-Hydrophilic Clock Copolymers. *Chme. Eur. j.* **4**, 2493–2500 (1998).
170. Tjandra, W., Yao, J., Ravi, P., Tam, K. C. & Alamsjah, A. Nanotemplating of Calcium Phosphate Using a Double-Hydrophilic Block Copolymer. *Chemistry of Materials* **17**, 4865–4872 (2005).

171. Junginger, M., Kübel, C., Schacher, F. H., Müller, A. H. E. & Taubert, A. Crystal structure and chemical composition of biomimetic calcium phosphate nanofibers. *RSC Advances* **3**, 11301 (2013).

Chapter 3

Effect of Major Ions in Hydroxyapatite Nanoparticles: Magnesium and Carbonate

In **Chapter 2** the great potential that offers the use of hydroxyapatite nanoparticles in the biomedical field for applications in gene delivery, cancer therapy and bio-imaging was introduced. Although extensive studies have been performed on this topic, there are still many aspects that are not well understood and some others that have not been fully explored. In this regards this chapter aims at investigating how the chemical composition of hydroxyapatite nanoparticles influences cell behavior in views of providing alternative nanoparticles/carriers for the safer and more effective delivery of drugs and genes into the cells. For this purpose in this chapter we will particularly focus at the investigation of how major doping ions found in bone apatite can affect the nanoparticle physicochemical properties and their interaction with cells.

3.1 Introduction

With the rationale that the mineral phase of bone consists of hydroxyapatite-like crystals, hydroxyapatite (HA) based materials have long been considered as potential materials in the repair, regeneration and substitution of bone tissue. There has been a long trajectory since HA began to be used and still now this material is the focus of extensive research in the area¹. In addition to the use of HA as bulk material in bone regeneration applications, HA in the form of nanoparticles

(NPs), is emerging as potential candidate in gene delivery applications²⁻⁸. Its inherent biocompatibility, biodegradability, inorganic nature and ease of fabrication makes it very attractive in front of the classical viral vehicles which, in spite of their widely spread use for their high transfection efficacy, are under debate because of their immunogenic and cytotoxic effects. Aside from gene delivery, HA-NPs by themselves or in combination with drugs have been used with success to target specific cells showing promising results, for instance, in treating tumors⁹⁻¹⁵. In addition, the feasibility of rendering HA-NPs fluorescent and also magnetic opens a wide range of possibilities in imaging and tumor ablation applications^{4,16-20}.

The two most attractive aspects of HA-based NPs are their inherent biocompatibility and biodegradability. Biocompatible carriers are essential to safely deliver genes/proteins/drugs into the cell without impairing the targeted site and this aspect is as crucial as their degradability, a point of particular interest to overcome the side effects of long-term cytotoxicity. Although these advantages have spurred numerous studies on the use of HA-NPs there are contradictory results which arise from a poor characterization of the material and their interaction with the target cells/site. Nevertheless, active research in this area is helping to build a more solid ground unveiling key aspects in the understanding of NPs-cell interaction.

It is well understood now that NP features such as size, morphology, dose, surface charge and agglomeration state affect cell behavior and therefore should be taken into account when using NPs in gene/protein/drug delivery applications. Along the same line it is clear too that the response of NPs is cell dependent. Results pertaining to the analysis of such characteristics on HA-NPs are available²¹⁻²⁹. However, it is important to stress that in some cases conclusions have been drawn from incomplete characterization studies. One aspect that remains to be investigated is how changes in the composition of HA-NPs influence cell behavior. The crystal lattice of HA is well known for accommodating a wide range of ionic substitutions among which carbonate (making up 4.8 wt% of bone) and Mg (making up 0.72 wt% of bone) stand as one of the major anionic and cationic

elements found in bone mineral³⁰⁻³². These two types of ions play very important roles in bone formation and metabolism³⁰. Mg ions for instance influence osteoblast and osteoclast activities and it is well known that the depletion of this ion in growing bone can impair the strength and firmness of bones and contribute to osteoporosis³³. Carbonate ions are recognized as inhibitors of apatite crystal growth and it is well known that their incorporation leads to a reduction of the crystal order and increase of solubility³⁴.

The ionic substitutions in HA-NPs is well documented^{30,35} but, unfortunately, in many cases cell culture studies are lacking³⁶⁻³⁹, or they focus in one type of substituting ion not allowing comparison of results, or the studies are performed on bulk samples prepared by compressing the NPs in molds^{18,40-42}. In bulk systems such as coatings, granulates and solid pieces, the effect of magnesium and carbonate substitution in HA on bone-related cells has been investigated extensively. For example, Brandy *et al.*⁴³ evaluated the effect of carbonate substituted HA on cell response and showed a decrease in differentiation of osteoblast-like cells with increasing carbonate content. Many studies have also been performed preparing apatite implant materials containing Mg and had demonstrated improved bioactivity. *In vivo* studies further proved that the use of Mg-doped HA enhanced its osteoconductivity and resorption compared to commercial stoichiometric HA granulate⁴⁴. Moreover, co-doping of carbonate and Mg ions in HA with biological-like amounts (6 wt% and 1 wt%, respectively) was achieved. The doped powders enhanced mesenchymal stem cells and osteoblast-like cells behavior in terms of adhesion, proliferation and metabolic activation compared to stoichiometric HA³⁴. However, these results cannot be used to explain the interaction of individual NPs with cells as, in the bulk form, NPs cannot be internalized (endocytosed or phagocytosed).

3.2 Objectives

The goal of this chapter is to investigate if NP composition affects cell behavior to ensure optimal design of HA-NPs for future cellular internalization applications. To

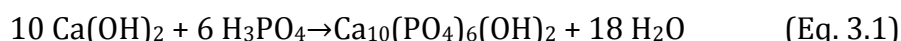
allow comparison of results all NPs were synthesized following the same protocol and thoroughly characterized. More specifically this chapter tackles:

- Preparation and exhaustive characterization of NPs doped with various doses of carbonate, magnesium and the co-doping of both, carbonate and magnesium ions.
- Cell culture studies using two different cell types (osteosarcoma cells MG-63 and rat mesenchymal stem cells, rMSCs) under various conditions: 1) on citrate-dispersed NPs and on agglomerated NPs and 2) in cell culture media containing or excluding 10 v/v% of foetal bovine serum (FBS).

3.3 Materials and Methods

3.3.1 Synthesis of ion-doped HA nanoparticles

All HA-NPs were synthesized by neutralization of $\text{Ca}(\text{OH})_2$ with H_3PO_4 (Eq. 3.1) at 40 °C in air atmosphere. The temperature was controlled by means of a thermal bath (Huber Kältemaschinenbau GmbH, Germany) and the reaction was performed on thermo-jacketed vessels connected to the bath. The pH was continuously monitored throughout the reaction.



The synthesis reaction of the non-doped NPs was carried out as follows. 100 mL of 0.334 mol/L $\text{Ca}(\text{OH})_2$ (Fluka, 96 wt% pure) was first prepared and then a 0.2 M H_3PO_4 (Panreac, 85 wt% pure) solution was added dropwise into the system at the constant rate of 1ml/min under constant stirring. The reaction was stopped when the pH reached 8. Next, the suspension was left stirring for 20-30 min and was then transferred into a glass bottle where it was left maturing overnight at room temperature. On the next day the suspension was rinsed with Milli-Q water till constant conductivity following cycles of 5 min centrifugation at 800 g (Beckman Allegra 21 Benchtop Centrifuge)/re-suspension. Afterwards the product was frozen at -80°C and lyophilized (Telstar Cryodos). Once lyophilized the powder was kept in a desiccator.

For the preparation of carbonate doped HA-NPs, different amounts of sodium hydrogen carbonate (NaHCO_3 , Sigma-Aldrich, ReagentPlus®, ≥99.5 wt% pure) were added to the $\text{Ca}(\text{OH})_2$ suspension prior to addition of the phosphoric acid. The amount of CO_3^{2-} added was calculated so as to have 5, 10 and 20 wt% of carbonate. In a similar manner the synthesis of the Mg doped NPs was achieved mixing the calcium hydroxide suspension with $\text{MgCl}_2 \cdot 6\text{H}_2\text{O}$ (Panreac, 99 wt% pure) to get 5, 10 and 20 wt% of Mg^{2+} . Co-substitution of carbonate and Mg was accomplished with a slight modification in the protocol⁴⁵. The $\text{Ca}(\text{OH})_2$ powder was suspended in 80 mL (instead of 100 mL) and the desired amount of Mg salt was dissolved into it. The carbonate salt was dissolved separately in 20 mL of water

and added dropwise (1mL/min) into the basic suspension prior to the addition of the phosphoric acid. For this particular reaction the addition of acid was stopped at pH 7. All other parameters were kept constant. Maturation, rinsing and drying of the NPs was performed as stated above. The different NPs were designated as follows:

HA: non-doped NPs,

5C, 10C, 20C: carbonate doped HA-NPs (5, 10 and 20 wt% respectively)

5M, 10M: magnesium doped HA-NPs (5 and 10 wt% respectively)

4M/7C: 4 wt% magnesium and 7 wt% carbonate co-doped HA-NPs.

3.3.2 Characterization of ion-doped HA nanoparticles

The phase composition was determined by X-ray powder diffraction (XRD), using a D8 Advance Diffractometer (Bruker, Karlsruhe, Germany) with CuK α radiation at 40 kV and 40 mA. XRD spectra were recorded in the range 10–80°, with a step size of 0.02° and a counting time of 1 s.

Fourier transform infrared spectroscopy (FTIR) in the ATR mode (Attenuated Total Reflectance mode, Nicolet 6700 spectrometer, Thermo Scientific) was used to check the typical functional groups present in apatite and, in particular, the presence of carbonate bands in the powders. All the spectra were obtained by averaging 32 scans collected in the range 500–4000 cm⁻¹, with a spectral resolution of 4 cm⁻¹.

To quantitatively measure the content of carbonate in the powders elemental carbon determination analysis (Thermo EA 1108 CHNS-O Thermo Scientific, Milan, Italy) was performed on 10 mg of sample previously dehydrated at 120 °C. The sample was pyrolyzed and combusted using vanadium oxide (V₂O₅) as an oxidant at 1000 °C in an oxygen atmosphere and the resulting gaseous products were chromatographically separated and quantified to yield the concentration of carbon. Quantitative inductively coupled plasma–optical emission spectrometry analysis (ICP-OES, Perkin Elmer Optima 3200RL), was applied to determine the overall

content of Ca, P, Na and Mg. Samples were prepared dissolving 100 mg of powder in 5 mL of 10 wt% HNO₃ (Panreac, 69 wt% pure) which was then 10 or 20-fold diluted.

The specific surface area (SSA) of the NPs was determined from the nitrogen adsorption data in the relative pressure range (P/P_0) from 0.05 to 0.35 by using the Brunauer-Emmett-Teller (BET) method with the ASAP2020 physisorption analyzer (Micromeritics, Norcross, GA, USA). The sample was outgassed at 120 °C before analysis.

Densities of samples were measured by helium pycnometry (Micromeritics' AccuPyc II 1340 Gas Pycnometer). The samples have to be dried in oven at 120 °C for 8 hour prior to submitting to the equipment.

The morphology of the NPs was assessed by transmission electron microscopy (TEM, JEOL 1010). Samples for TEM examination were prepared by soaking a 300 mesh carbon-coated copper grid in the solution of interest, blotted to remove the excess liquid and air dried.

The apparent solubility of the NPs was evaluated by monitoring the conductivity changes (Crison MM41) of a 0.1 mol/L acetate buffer solution (25 °C, pH=5.5) containing 1 mg/mL of NPs with time.

3.3.3 Preparation and characterization of nanoparticles suspension

NPs dispersion was achieved mixing 0.1 g of the NPs with 10 ml of 1 wt% sodium citrate solution (C₆H₅Na₃O₇·xH₂O, Sigma-Aldrich, ReagentPlus®, purity ≥99%). To improve dispersion, the suspension was sonicated with a high frequency ultrasound probe sonicator (Branson Digital, Model 250W) to separate the agglomerates and facilitate citrate adsorption. The following settings/conditions were applied: 3 mm diameter tip, 40 % amplitude (~50 Watts) and 2 minutes of sonication (with cycles of 15 sec sonication followed by 10 sec pause to prevent

excessive heating) in an ice bath. Suspensions without citrate were also prepared following the exact same protocol but replacing the 10 mL of 1 wt% sodium citrate solution by 10 mL of MilliQ water (18.2 M Ω /cm).

The surface charge of samples was determined by measuring the zeta potential of the NPs in Milli-Q water at a concentration of 250 μ g/mL of NPs (Zetasizer Nano-ZS from Malvern Instruments Ltd., UK). Prior to measurement the stock suspensions of 1 wt% NPs dispersed in either 1 wt% citrate or water were first diluted in cell culture media (DMEM, Dulbecco's Modified Eagle medium) containing or excluding 10 v/v% foetal bovine serum (FBS) to achieve a final concentration of 1000 μ g/mL of NPs, the mixture was then allowed to interact for a couple of hours and afterwards the NPs were centrifuged, rinsed with Milli-Q water and resuspended with Milli-Q water to make the final concentration of 250 μ g/mL prior to measurement.

3.3.4 *In vitro* cell culture studies

3.3.4.1 Cell culture

Human osteosarcoma MG-63 cell line and rat mesenchymal stem cells rMSCs were cultured in Dulbecco's Modified Eagle medium (DMEM) or advanced DMEM, respectively, containing 10 v/v% FBS, penicillin/streptomycin (50 U/mL and 50 μ g/mL, respectively), 2 mmol/L L-glutamine and 20 mmol/L HEPES buffer at 37 °C in a humidified atmosphere at 5 % CO₂. When cells attained confluence, they were detached using 0.25 % Trypsin and seeded onto standard polystyrene tissue culture plates (96 wells) at a cell density of 1×10^4 cells/well. The seeded cells were incubated overnight to allow cell adhesion prior to adding the NPs.

3.3.4.2 Exposure of cells to doped and non-doped NPs

Cells were exposed to all NPs (dispersed in citrate or in water) in two different scenarios: in cell culture media supplemented with 10 v/v% FBS and without FBS. The appropriate volume of NPs from the stock (1 wt% NPs in either 1 wt% of sodium citrate or water) was added to the corresponding cell culture media to make a final concentration of 100 μ g/mL. Before adding the suspensions to the

cells the mixture was vortexed to homogenise it. The incubation period was set to 24 h. For selected compositions (i.e., HA and 10M) the same experiment was repeated but working simultaneously at 37 °C and 4 °C.

To study the effect of NPs dose on cytotoxicity, the amount of 10M NPs in cell culture media was increased following the concentrations: 100, 250, 500, 1000 µg/mL. Non-doped HA was also included as control.

3.3.4.3 Cytotoxicity test

For the cytotoxicity evaluation of the various NPs the cell culture medium was removed after the 24 h incubation time and then viable cells attached on the surface of polystyrene tissue culture plates were lysed adding 100 µL of mammalian protein extraction reagent (M-PER, Thermo Scientific Inc., USA). Upon lysis cells released lactate dehydrogenase (LDH) that was measured using a commercially available kit (Cytotoxicity Detection Kit^{PLUS}, Roche, USA) following the manufacturer instructions. The absorbance at 492 nm was quantified on a micro spectrophotometer (PowerWave XS, Bio-Tek Instruments, USA) and the percentage of viability was calculated by the following equation:

$$\text{viability}\% = \frac{\text{exp. value} - \text{negative control}}{\text{positive control} - \text{negative control}} \times 100 \quad (\text{Eq. 3.2})$$

Where the 'positive control' was the absorbance value of cells incubated in cell culture medium under the same conditions of the experimental value but without NPs and the 'negative control' corresponded to the absorbance of the well without NPs and without cells. The studies done in triplicate were expressed as mean ± standard deviation. Statistical significance was accepted at a level of p<0.05.

3.3.4.4 Cellular uptake of NPs

TEM was used to visualize cellular uptake of HA and 10M NPs dispersed in Milli-Q water by MG63 cells. Cells were exposed for 24 h to the NPs in cell culture media excluding FBS. Briefly, the cultured cells were fixed with 2.5 wt% glutaraldehyde in 0.1 mol/L phosphate buffer for 1 h 30 min at room temperature and, both the

media and the film formed at the bottom of the well was detached and centrifuged to form a pellet. The pellet was then rinsed prior to adding 1 wt% osmium tetroxide and dehydrated in an ascending series of acetone solution up to 100 % and infiltrated with EPON12 resin. Upon resin polymerization (48 h, 60 °C) blocks were sectioned using an ultramicrotome (Ultracut UCT, Leica Microsystems GmbH, Vienna, Austria). The sections were stained with 2 wt% uranyl acetate, and thereafter observed with optical microscope (Leica DM2000 LED, Leica Microsystems GmbH, Vienna, Austria) and transmission electron microscopy (Tecnai Spirit FEI, Eindhoven, The Netherlands).

3.4 Results and discussion

3.4.1 Effect of ion doping on physicochemical properties

3.4.1.1 Characterization of carbonate-doped nanoparticles

Figure 3.1 shows the XRD and FTIR patterns of the NPs synthesized with various concentrations of carbonate, i.e. 0, 5, 10 and 20 wt%. XRD results (Figure 3.1a) showed that all synthesized NPs were phase pure as there were no peaks other than those assigned to HA (ICDD No. 9-432). A detailed examination of the XRD data for the different NPs revealed additional characteristics. Carbonation caused a marked decrease in the intensity of the (00x) reflections and their shift towards lower 2θ angles. The first of these two features was indicative of a change in the crystal morphology, while the later served to prove the incorporation of carbonate in the apatite lattice replacing phosphate groups (B-type substitution)⁴³. FTIR results (Figure 3.1c) further confirmed the B-type substitution, typical of hydroxyapatites precipitated at low temperature, through the presence of specific bands: the asymmetric stretch vibration, ν_3 , at around 1430 and 1450 cm^{-1} and the out-of-plane bend vibration, ν_2 , close to 870 cm^{-1} .⁴⁶

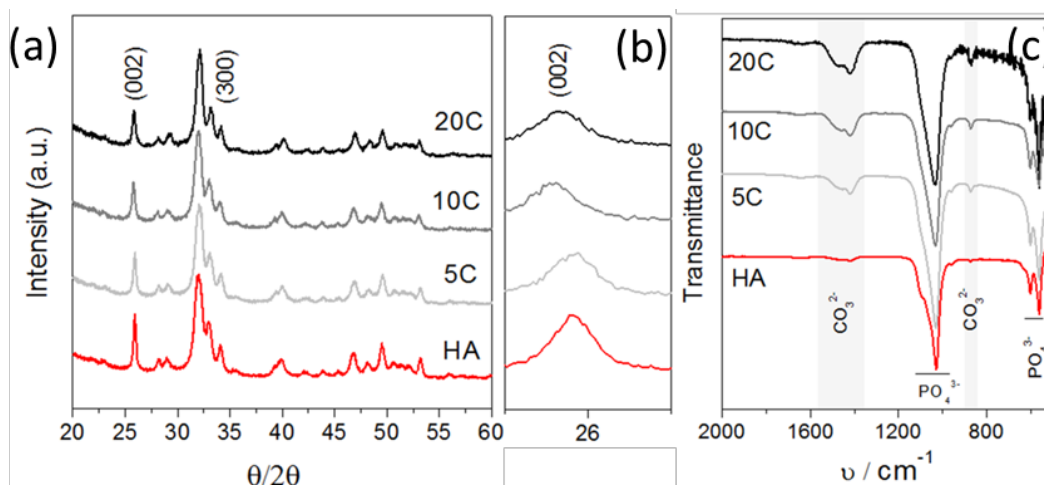


Figure 3.1 (a) X-Ray diffraction data for the different NPs: non-doped (HA) and NPs doped with various carbonate contents, (b) detail of the peak shift corresponding to the (002) reflection with carbonate content and, (c) FTIR spectra of the various compositions.

An additional feature observed from both, XRD and FTIR was the loss in the resolution of the peaks and bands which was explained from the crystal distortion provoked by carbonate incorporation. In spite of the fact that during synthesis

specific amounts of carbonate salt were added, the exact amount incorporated in the NPs measured by elemental carbon determination analysis differed from the nominal value as can be seen from the results summarized in Table 3.1. The 2.46 wt% of carbonate observed in NPs prepared without adding any carbonate salt is attributed to the traces of carbonate present in the $\text{Ca}(\text{OH})_2$ powder and also to the dissolution of carbon dioxide in the solution reaction during precipitation.

Table 3.1 Compilation of various characteristics of the different NPs.

	CO_3^{2-} wt %	Mg^{2+} wt %	Na^+ wt %	Ca/P Atomic	$(\text{Ca}+\text{Mg})/\text{P}$ atomic	SSA m^2/g	Density (g/cm^3)
HA	2.46 ± 0.03	0.27	0	1.76 ± 0.03	1.78 ± 0.03	93.6	2.80 ± 0.02
5C	6.63 ± 0.42	0.26	0.31	1.85 ± 0.04	1.89 ± 0.06	87.0	2.72 ± 0.02
10C	10.1 ± 0.20	0.26	0.43	1.92 ± 0.03	1.94 ± 0.02	74.6	2.70 ± 0.02
20C	11.4 ± 0.40	0.26	0.54	2.07 ± 0.03	2.10 ± 0.03	48.4	2.70 ± 0.01
5M	n.d.	1.23	0	1.68 ± 0.06	1.77 ± 0.04	103.3	2.77 ± 0.04
10M	n.d.	2.17	0	1.57 ± 0.02	1.77 ± 0.01	85.2	2.69 ± 0.04
4M7C	7.8	1.52	0.04	1.77 ± 0.03	1.91 ± 0.03	59.8	n.d.

Another point to note is the limited increase in carbonate uptake by the NPs when adding 20 wt% of NaHCO_3 as compared to the 10 wt% one. For the 10 wt% reaction condition a 10 wt% was incorporated but for the 20 wt% only 11 wt% of carbonate became incorporated. Such behavior pointed out that saturation of the apatite structure might have occurred. ICP-OES results (Table 3.1) showed that the incorporation of carbonate was accompanied by the incorporation of Na too in the lattice. This co-substitution is very common as it helps balancing the charges in the exchange of PO_4^{3-} by CO_3^{2-} .³⁹ The skeletal density evaluated by He pycnometry decreased with the addition of CO_3 as well as with Mg addition due to the replacement of a lighter ions for PO_4^{3-} and Ca, respectively.

The incorporation of carbonate in the apatite lattice had a marked effect on the morphology of the NPs (Figure 3.2a). From a needle-like shape the NPs changed to a more isotropic shape with the increase in the content of carbonate as was also noticed by other authors⁴⁵. Such a change in shape was already hinted in the XRD data from the decrease in intensity of the (00x) reflections for the higher carbonate containing NPs. Indeed, it is known that needle-like HA crystals exhibit preferential

growth along the c axis, which translates in the selective increase of the (00 x) diffraction peaks. It is then not surprising to find that more isotropic crystals should result in an “intensity” decrease of such peaks as observed with the increase in carbonation (Figure 3.1). Not only has the shape tended to become more isotropic but also the SSA has decreased owing to the decrease in the aspect ratio of the NPs with carbonation (Table 3.1). The incorporation of carbonate in the structure of HA was further proved from the increase in their solubility, as indicated by the increase in conductivity (Figure 3.2b).

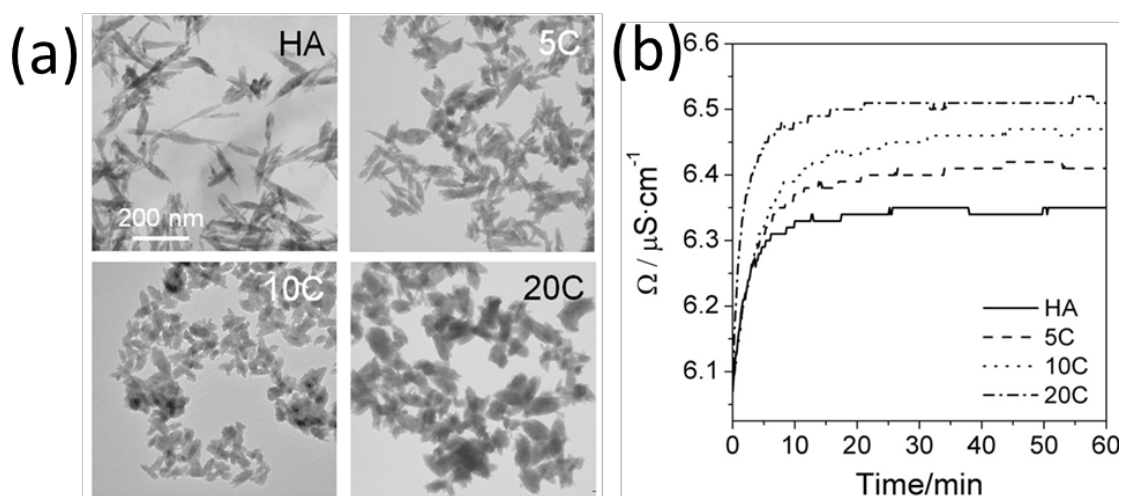


Figure 3.2 (a) TEM micrographs of the non-doped (HA) and carbonate-doped NPs and (b) apparent solubility curves determined through conductivity measurements for the various NPs.

3.4.1.2 Characterization of magnesium-doped nanoparticles

XRD and FTIR results pertaining to the synthesis of Mg doped NPs are summarized in Figure 3.3. Similar to what was achieved for the carbonate doped NPs, Mg containing NPs can be considered phase pure as no peaks of foreign phases were detected by XRD. The addition of Mg salt during synthesis led to slightly broader peaks in the XRD pattern, which accounted for a decrease in the crystallinity of the NPs with increasing Mg content. The slight shift of the (002) diffraction peak observed (Figure 3.3b) for Mg substituted samples has been reported to be due to contraction of the cell lattice parameters of HA caused by the smaller ionic radius of the Mg cation compared to calcium⁴⁶. XRD thus proved that at least part of the Mg cations was indeed incorporated in the HAP structure. Similarly to what was

observed for the carbonate-doped NPs, not all Mg that was added in the synthesis reaction became incorporated into the crystal structure. Substitution of Mg for Ca in the structure of HA has been reported to occur over a limited composition range up to about 10 at.%³⁰. In the present work Mg incorporation was further confirmed by ICP-OES analysis (Table 3.1). The fact that the atomic ratio (Ca+Mg)/P was maintained regardless of the Mg content could be used to point that Mg was replacing Ca rather than becoming adsorbed on the surface of the nanocrystals. Furthermore, it has been reported that the incorporation of low Mg contents in the HA structure preserves the (Ca+Mg)/P stoichiometry⁴⁵.

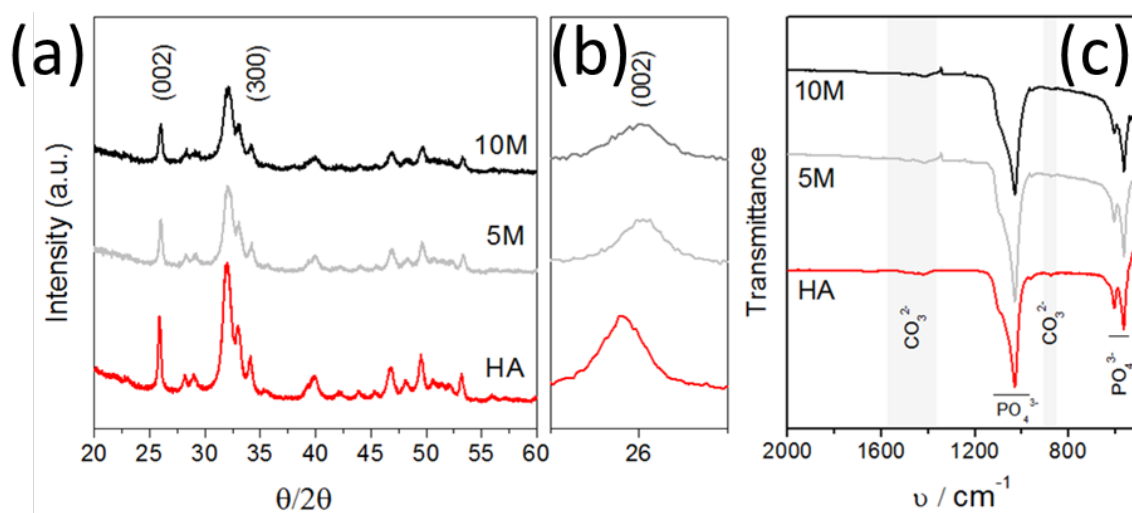


Figure 3.3: a) X-Ray diffraction data for the different NPs: non-doped (HA) and NPs doped with various magnesium contents, b) detail of the peak shift corresponding to the (002) reflection with magnesium content and, c) FTIR spectra of the various compositions.

Mg incorporation slightly influenced the FTIR spectra as observed from a loss in the resolution of the bands (Figure 3.3c). Carbonate was also present in the Mg doped NPs as can be detected from the FTIR analyses. The level of carbonate was similar to that found in the “non-doped” HA. As explained earlier, carbonation was caused by the presence of carbonate in the $\text{Ca}(\text{OH})_2$ reagent and also to dissolution of carbon dioxide from the atmosphere during the synthesis reaction.

In spite of the incorporation of Mg inside the crystal lattice, the morphology of the Mg-doped NPs was not altered as shown by the identical size and needle-like shape

to the non-doped ones (Figure 3.4). This was probably caused by the low content of Mg incorporated. The solubility of the Mg doped NPs slightly increased when compared to the non-doped HA NPs but no significant differences were observed between 5M and 10M probably due to the similar values of Mg measured in both compositions (Table 3.1). Similar SSA values were also obtained for the Mg-doped and non-doped HA (Table 3.1).

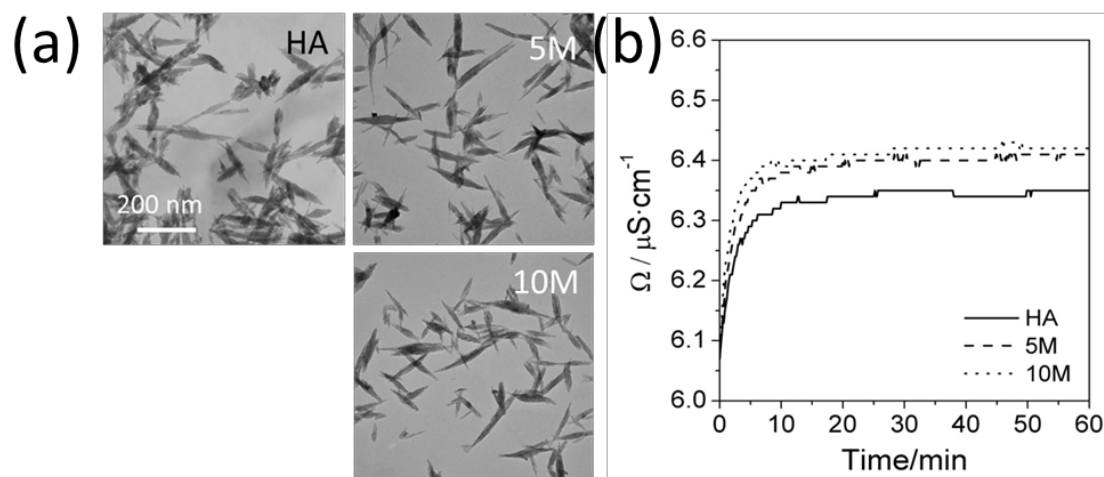


Figure 3.4: a) TEM micrographs of the non-doped (HA) and carbonate-doped NPs and b) solubility curves for the various NPs.

3.4.1.3 Characterization of magnesium/carbonate-doped nanoparticles

Co-doping of both, Mg and carbonate, led to NPs sharing characteristics from both types of substitutions. The presence of Mg and carbonate was verified by ICP and elemental carbon determination respectively. Co-doping seemed to slightly facilitate the introduction of Mg into the crystal lattice of HA as observed from the 1.52 wt% content which was superior to that found for non-carbonated Mg-NPs. This could be explained from the more open and distorted crystal lattice that results after carbonate incorporation.

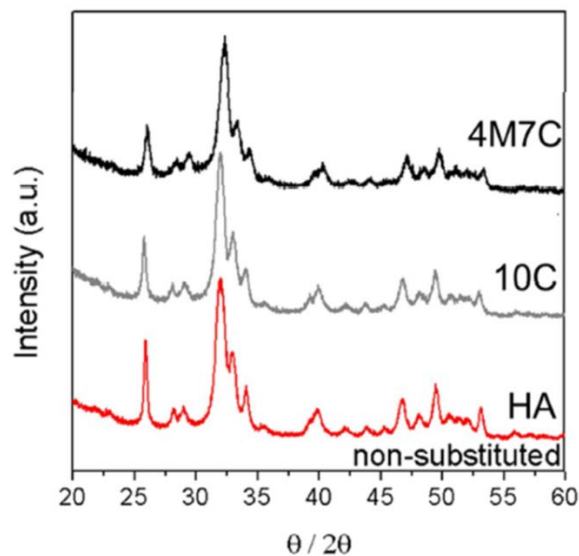


Figure 3.5 X-ray diffraction of various NPs: non-doped (HA), 10C and co-doped Mg/carbonate NPs

One uncertainty that often exists in the synthesis of doped hydroxyapatite NPs is whether ions get incorporated into the crystal structure or they simply adsorb on the surface of the NPs belonging to the so called hydrated layer⁴⁷. The simultaneous incorporation of carbonate and magnesium makes it very difficult to ascertain this point. The fact that ion-substitution is often associated to a loss in crystallinity prevents the accurate evaluation of crystal lattice parameters by conventional XRD (Figure 3.5) making difficult to get any conclusion from this technique. No conclusion could thus be drawn in this regard. The morphology of co-doped HA NPs were shown in Figure 3.6 indicating that ions co-doped in HA made need-like structure short which was similar to that did by carbonate ions alone.

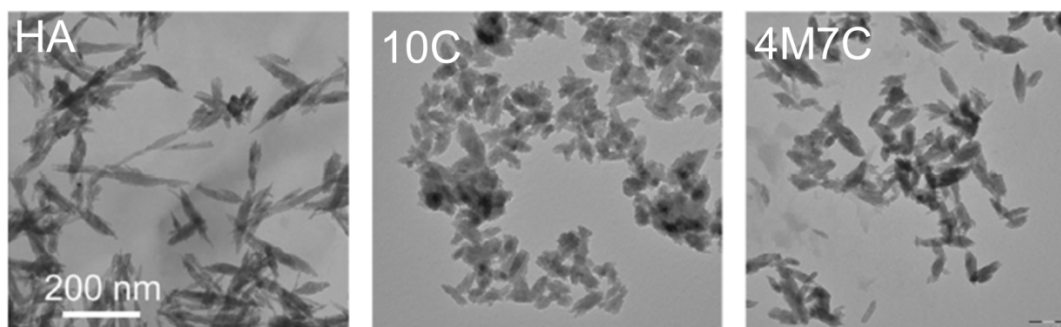


Figure 3.6 TEM images of different NPs: non-doped (HA), 10C and co-doped Mg/carbonate NPs

3.4.2 Dispersion behavior and surface charge of the various ion doped NPs

The surface charge of the NPs pre-incubated in various conditions and subsequently centrifuged and re-suspended in water prior to measurement (removal of salts was required to minimize damage of the electrodes) is summarized in Table 3.2. Pre-incubation of citrate dispersed and non-dispersed NPs were done in cell culture media (DMEM) including/excluding 10 v/v% of FBS. As can be seen, the surface charge of the bare NPs (without citrate and without FBS) was low in absolute value but when FBS, citrate or a mixture of both was added the surface charge became clearly negative due to the adsorption of proteins and citrate on the surface of the NPs⁴⁸. No significant differences in surface charge were detected among the different NPs compositions regardless of the pre-incubation condition.

Table 3.2 Surface charge of the NPs under various conditions.

	SURFACE CHARGE			
	ζ (H ₂ O) mV	ζ (FBS/H ₂ O) mV	ζ (citr.)* mV	ζ (FBS/citr.) mV
HA	+4.0 ± 0.1	-20.1 ± 0.3	-13.3 ± 0.5	-23.3 ± 1.5
5C	+1.4 ± 0.1	-19.8 ± 1.0	-14.2 ± 0.6	-22.4 ± 0.6
10C	+1.3 ± 0.1	-19.2 ± 0.7	-13.6 ± 0.3	-21.9 ± 0.6
5M	+1.0 ± 0.1	-17.9 ± 0.3	-15.5 ± 0.4	-23.9 ± 0.3
10M	-1.7 ± 0.1	-17.1 ± 0.2	-13.3 ± 0.4	-19.8 ± 0.5
4M7C	-1.7 ± 0.1	-20.3 ± 0.3	-11.2 ± 0.5	-20.3 ± 0.4

*Values might be slightly underestimated due to the rinsing step applied prior to measurement. Rinsing might have partially desorbed citrate from the NPs surface.

3.4.3 Effect of ion doping on cell behavior

The main goal of the present work was to investigate the cell response to ion-doped HA-NPs in views of exploring how the presence of foreign ions could affect cellular internalization. Unfortunately, doping, besides incorporating the foreign ion/s can cause morphological and physicochemical changes in the structure as it has just been shown in the preceding sections. All this has to be taken into account in the interpretation of the results.

3.4.3.1 Cytotoxicity on MG63 cells

Figure 3.7 shows the percentage of cell viability after incubating MG63 cells with 100 µg/mL NPs for 24h. Four different conditions were explored. On the one hand the effect of using well dispersed (+NaCit) versus as-prepared (-NaCit) NPs was investigated, and on the other hand it was explored the effect of adding or excluding 10 v/v% FBS (+FBS or -FBS respectively) during cell culture. Both, the adsorption of dispersant and proteins from FBS on the surface of the NPs can substantially change the surface properties of the NPs which can affect cell internalization⁴⁹. It was thus interesting to investigate in an environment free of dispersant and protein the real effect of the bare NPs even though this would cause NPs agglomeration. Albeit agglomeration/aggregation could presumably affect the reproducibility of experiments and even hamper the targeting efficiency of nanoparticles to cells, influencing the degree of uptake and toxicity by cells,^{50,51} studies performed on the bare material can provide unique information.

Results in Figure 3.7 clearly showed that for MG63 cells the use of NPs dispersed in sodium citrate, regardless of the presence of FBS in the cell culture media, were not cytotoxic as shown by the high percentage in cell viability. Visual inspection of the experiments conducted without the addition of dispersant revealed NPs sedimentation, forming a layer on top of the cells after 24 h of cell culture. This occurred regardless of the presence of FBS (Figure 3.7). Interestingly, under these circumstances, when NPs were cultured in the presence of FBS viability was preserved for all NPs compositions but when the experiments were carried out on the bare NPs, 10M and 4M7C NPs became clearly cytotoxic. Experiments performed using different batches of NPs consistently confirmed the results. The experiments pointed that a specific content of Mg, which in 10M and 4M7C was 2.2 and 1.5 wt% respectively, was needed to trigger such response. However, it is not very clear why 5M with properties very close to that of 4M7C except for the slightly lower content in Mg (1.2 versus 1.5 wt%) was not cytotoxic. Unfortunately the synthesis of Mg doped NPs with higher doping contents did not result in a phase pure compound, impeding corroboration of the cytotoxic effect using HA-NPs with even higher contents of Mg.

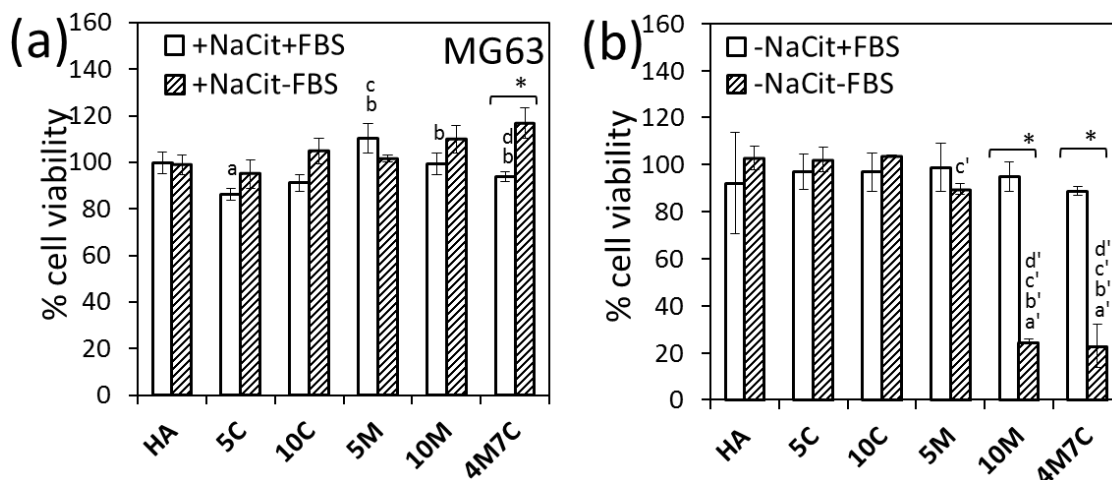


Figure 3.7 Viability of MG63 cells exposed to 100 µg/mL of the various NPs for 24 h. (a) cells exposed to NPs dispersed in citrate in the presence or absence of 10 v/v% FBS and (b) cells exposed to NPs dispersed in water in the presence or absence of 10 v/v% FBS. Letters indicate significant differences among NPs cultured with FBS: a- indicates differences with HA, b- differences with 5C, c-differences with 10C, d-differences with 5M and e-differences with 10M. Letters with (') indicate significant differences among NPs cultured without FBS ($P < 0.05$, $N = 3$). (*) indicates significant differences for the same type of NPs cultured with and without FBS ($P < 0.05$, $N = 3$).

It is interesting to discuss all cell culture results taking into account the specific conditions associated to each study and each NP. Since 10M and 4M7C NPs induced cytotoxicity in a specific scenario (in absence of sodium citrate and FBS), it seems reasonable to think that these particular NPs in all other scenarios (with FBS and/or citrate) were probably non cytotoxic simply because they could not be internalized (or they were less internalized). A very straightforward explanation to this could be the surface charge. It is very well known the high affinity of citrate and proteins for hydroxyapatite. Upon adsorption both render a negative charge on the surface of the NPs (Table 3.1) which could then prevent or minimize internalization owing to electrostatic repulsion with the cell membrane²⁶. From the results it is however not clear whether for the rest of the bare NPs (HA, 5C, 10C and 5M cultured without citrate and FBS) the lack of cytotoxicity was due to a lack of internalization or to a non-toxic response upon internalization.

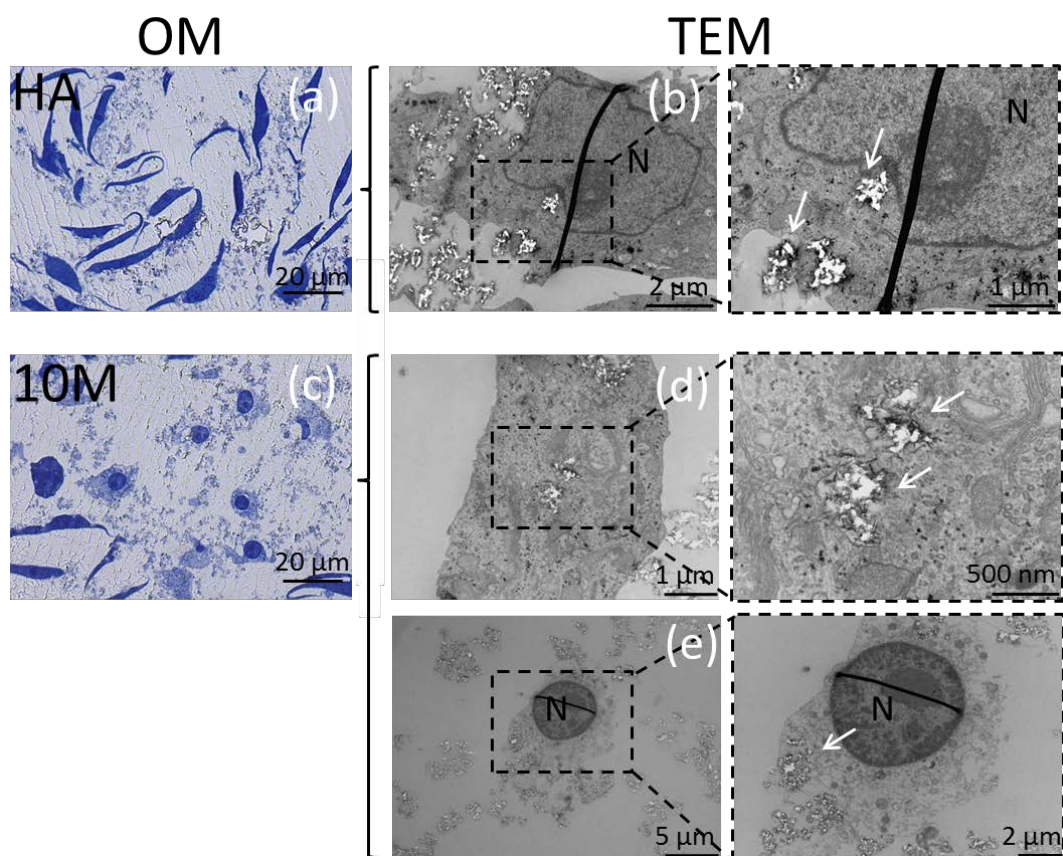


Figure 3.8 (a, c) Low magnification optical micrographs (OM) of stained MG63 cell sections that had been cultured in the presence of bare HA and 10M NPs for one day showing normal morphologies for the non-doped HA NPs (a) and damaged cell membrane for the Mg-doped 10M NPs (c). (b,d,e) TEM micrographs of stained sectioned cells proving NPs internalization in both, HA (b) and 10M NPs (d, e). The presence of NPs is pointed with arrows. White regions in the TEM micrographs correspond to regions where NPs were present but became detached during sectioning. Close to these regions elongated NPs can still be distinguished. N denotes cell nucleus.

To prove if NPs internalization in the absence of dispersant and FBS was indeed occurring, MG63 cells that had been in contact with bare HA and 10M NPs were examined under TEM (Figure 3.8). The results not only proved that in both cases there were NPs entering the cells, but it also showed that 10M NPs caused considerable damage to the cell cytoplasm. Two additional experiments were then performed to corroborate that for the case of 10M the NPs needed to enter the cell to become cytotoxic (Figure 3.9). In the first experiment NPs were cultured with cells at 4 °C to minimize endocytosis (NPs uptake). This strategy, adopted from other published works,²⁷ is based on the fact that endocytosis is an energy driven

process and lowering the temperature should impede internalization. In the second experiment cells were cultured in media supplemented with different concentrations of Mg^{2+} (without NPs) corresponding to the amounts of Mg doped in the 10M (2.2 wt%) formulation to assess if Mg ions released from the NPs could be the source of cytotoxicity. The fact that the viability of cells was preserved at 4 °C and that the addition of Mg did not affect cell viability suggested that the cytotoxicity of 10M NPs resulted from internalization of the NPs.

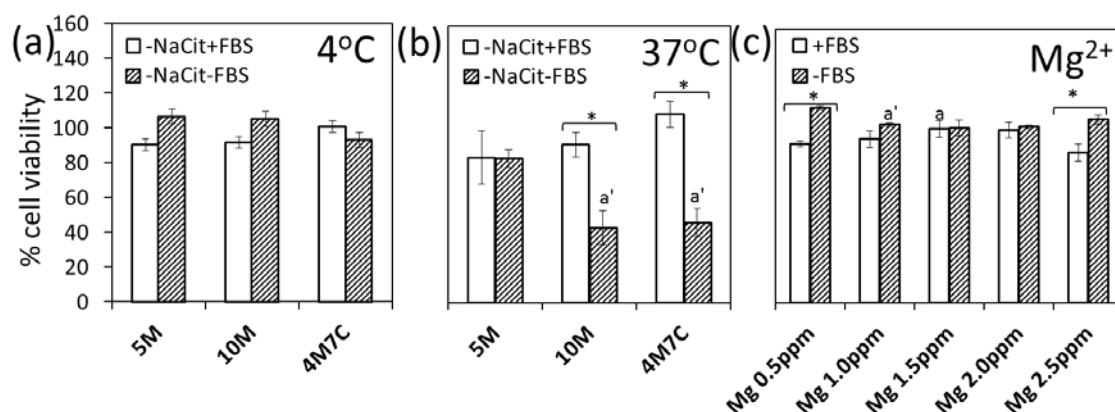


Figure 3.9 (a) and (b) viability of MG63 cells exposed to 100 $\mu\text{g}/\text{mL}$ NPs for 24 h at 4 °C and 37 °C respectively, and, (c) viability of MG63 cells exposed to cell culture media supplemented with various concentrations of $MgCl_2$. Letters a and a' in graphs (a) and (b) indicate differences with 5M NPs in the presence or absence of 10 v/v% FBS respectively. Letters a and a' in graph (c) indicate differences with 0.5 ppm of $MgCl_2$ in the presence or absence of 10 v/v% FBS respectively. (*) compares significant differences between the same pair of sample cultured with or without 10 v/v% FBS ($P < 0.05$, $N = 3$).

It is interesting to notice that unlike for 10M and 4M7C, internalization of HA-NPs (Figure 3.8) did not induce any toxic response; at least, in the conditions the experiment was performed (Figure 3.7). To further investigate this point cells were cultured with increasing amounts of NPs for the HA and 10M formulations to enhance internalization (Figure 3.10). The results revealed that the bare HA-NPs (i.e., when citrate and FBS was excluded in the cell culture) induced cytotoxicity in a dose dependent manner (Figure 3.10) and, for 10M, cytotoxicity was also evident though no trend could be detected with NPs dose. The hypothesis that even after increasing NPs dose only the “bare” NPs, and never the NPs adsorbed with citrate and/or FBS became cytotoxic reinforced the fact that citrate and FBS might be

hampering internalization. This finding reveals how critical surface charge is for this particular cell type and reinforces the need of undergoing studies specifically targeting the cell of interest. Certainly to further promote NPs internalization surface modification with natural cationic molecules could be made but this was not the objective of the work.

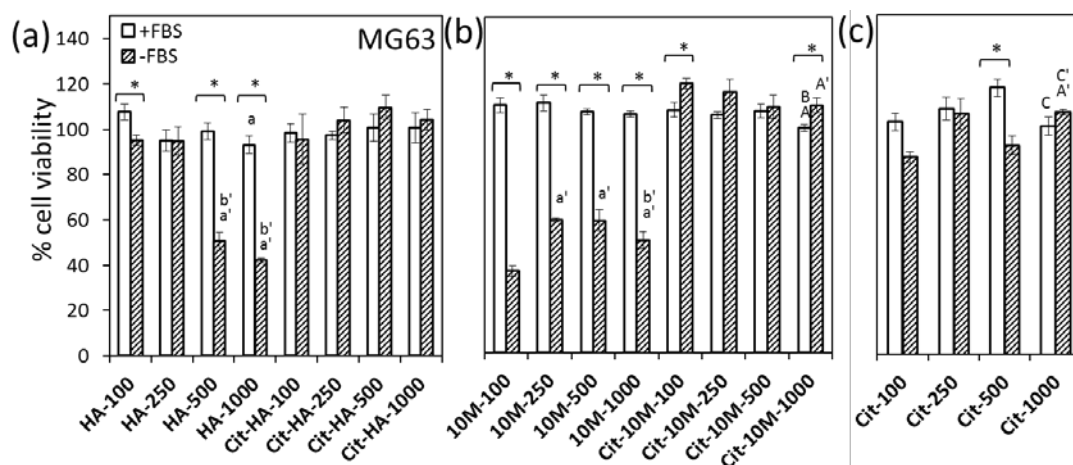


Figure 3.10 Dose dependent cytotoxicity of HA (a) and Mg-doped HA (10M) (b) for MG63 cells in the presence or absence of 10 v/v% FBS. NPs dispersed in citrate and in water (control) were tested. To discard any effect of citrate in the media cytotoxicity was also performed supplementing to the cell culture media the same concentration of citrate added for the dispersion of the NPs (c). Letters in the graphs indicate significant differences between NPs doses cultured with FBS: a- indicates differences with 100 µg/mL, b-differences with 250 µg/mL, c- differences with 500 µg/mL and, d-differences with 1000 µg/mL. Letters with () indicate significant differences between NPs doses cultured without FBS ($P < 0.05$, $N = 3$). Independent analyses were done for the samples containing citrate (capital letters) versus those without citrate (lower case letters). (*) compares significant differences between the same pair of NPs cultured with or without FBS ($P < 0.05$, $N = 3$).

It is out of the scope of the present work to elucidate the reason why 10M NPs are more cytotoxic than HA. However, it is worth stressing that morphologically and physicochemically speaking both NPs are very alike. It has been widely reported that properties such as NPs size, morphology and solubility can affect internalization, yet, this was not observed for instance in the series of carbonate substituted NPs where shape and solubility varied greatly with carbonate content (Figure 3.2). The similar features shared by HA and 10M NPs points to the doping ion as the factor responsible for their difference in cytotoxicity on MG63 cells. Although one could interpret the results speculating that if both NPs were equally

internalized then Mg would be pointed as the responsible ion for cell cytotoxicity, other explanations should be considered. The role of Mg in cancer cells is now better understood⁵³ and the fact that in cancer cells Mg channels are overexpressed could be related to a more active uptake of Mg doped NPs. An excess of NPs might then be the cause of their cytotoxicity. Interestingly, additional cell culture studies performed using concentrations as low as 25 $\mu\text{g}/\text{mL}$ of NPs already revealed the cytotoxic behavior of 10M NPs thus proving that only a very limited amount is needed to become cytotoxic (Figure 3.11).

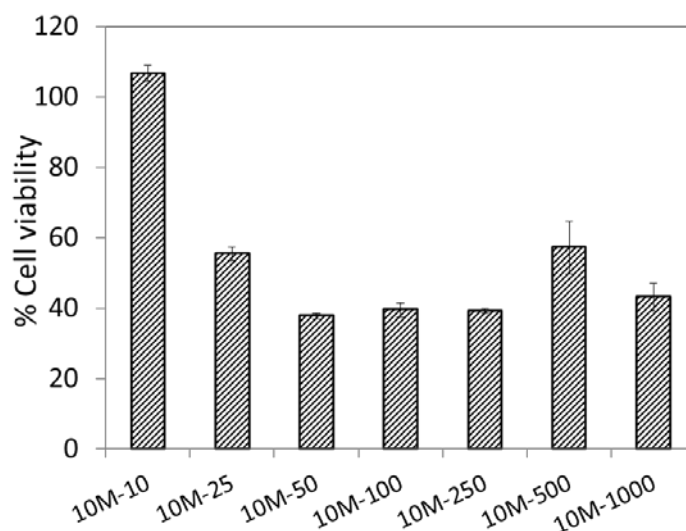


Figure 3.11 Dose dependent cytotoxicity of Mg-doped HA (10M) for MG63 cells in the absence of 10 v/v% FBS: from 10 $\mu\text{g}/\text{mL}$ to 1000 $\mu\text{g}/\text{mL}$.

Although it may be a bit premature, the results thus far obtained point to doping as a potential tool to modify cell behavior. In this regards, the simple incorporation of Mg into HA could be used to kill cancer cells without the need of conjugating any anticancer drug onto the NPs, thus eliminating all problems associated to the toxicity and side effects of such drugs.

3.4.3.2 Cytotoxicity on rMSCs cells

Besides the potential that doped NPs may have, it is well known that NPs interaction is cell dependent. In this regards it was very important to test how NPs reacted towards other cell types such as rMSCs. Identical cell culture conditions to those used for MG63 were applied to test the cytotoxicity of the various NPs on rMSCs (Figure 3.12).

Thus, rMSCs were incubated with 100 $\mu\text{g}/\text{mL}$ NPs either as-prepared (-NaCit) or well dispersed (+NaCit) in cell culture media containing or excluding 10 v/v% FBS (+/-FBS, respectively). The results differed substantially from those observed for MG63 cells. On the one hand, it is clear that using bare NPs regardless of whether FBS was added or not, cell viability was not compromised. The scenario however changed when using NPs dispersed in citrate. In the absence of FBS, viability increased in all doped NPs above 120 % while the non-doped HA-NPs remained at 100 %. In the presence of 10% FBS the opposite trend was observed: all doped NPs showed 80% viability while 100% was maintained for HA. Studies performed increasing NPs dose on HA and 10M NPs showed that viability slightly decreased for all cases in a dose dependent manner, which could be taken as an indicator for a higher degree of internalization (Figure 3.13). Taking altogether the results from Figure 3.12 and 3.13, it is interesting to see that unlike for MG63 cells the negative charge that surrounded the NPs upon citrate adsorption did not seem to prevent NPs internalization on rMSCs.

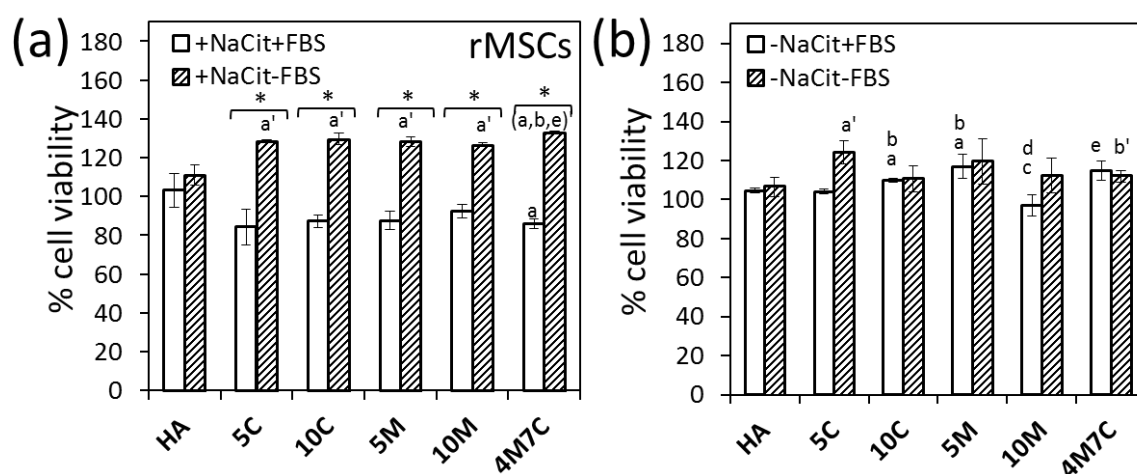


Figure 3.12 Viability of rMSCs cells exposed to 100 $\mu\text{g}/\text{mL}$ of the various NPs for 24 h. (a) cells exposed to NPs dispersed in citrate in the presence or absence of 10 v/v% FBS and (b) cells exposed to NPs dispersed in water in the presence or absence of 10 v/v% FBS. Letters indicate significant differences among NPs cultured with FBS: a- indicates differences with HA, b- differences with 5C, c- differences with 10C, d- differences with 5M and e-differences with 10M. Letters with (') indicate significant differences among NPs cultured without FBS ($P < 0.05$, $N = 3$). (*) indicates significant differences for the same type of NPs cultured with or without FBS ($P < 0.05$, $N = 3$).

With regards to the effect of the various formulations of doped NPs on rMSCs, there were no significant differences that could be attributed to the presence of the

different ions (Figure 3.12). These findings clearly contrasted with the results obtained for MG63 cells where 10M and 4M7C NPs reacted differently from the rest (Figure 3.7). Although Mg and carbonate apparently did not play any major role on rMSCs this cannot be used to prove that this cell type is not sensitive to NPs composition. Other ions might be more critical than the ones chosen herein. Nevertheless it is worth mentioning that the results on the dose dependent cytotoxicity for HA and 10M formulations did reveal a more pronounced cytotoxic behavior for HA than for 10M at high NPs doses.

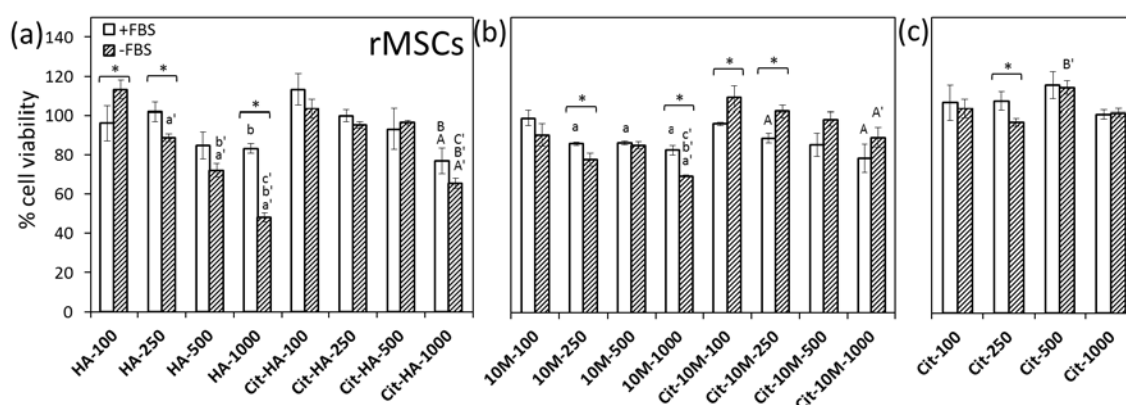


Figure 3.13 Dose dependent cytotoxicity of HA (a) and Mg-doped HA (10M) (b) for rMSCs in the presence or absence of 10 v/v% FBS on rMSCs. NPs dispersed in citrate or in water (control) were tested. To discard any effect of citrate in the media cytotoxicity was also performed supplementing to the cell culture media the same concentration of citrate added for the dispersion of the NPs (c). Letters in the graphs indicate significant differences between NPs doses cultured with FBS: a-indicates differences with 100 µg/mL, b- differences with 250 µg/mL, c- differences with 500 µg/mL and, d- differences with 1000 µg/mL. Letters with (') indicate significant differences between NPs doses cultured without FBS ($P < 0.05$, $N = 3$). Independent analyses were done for the samples containing citrate (capital letters) versus those without citrate (lower case letters). (*) compares significant differences between the same pair of NPs cultured with or without FBS ($P < 0.05$, $N = 3$).

This distinct behavior shown by MG63 and rMSCs in contact with NPs has also been reported by other authors for similar non-doped HA-NPs. It is not new that HA-NPs can be cytotoxic to cancerous cells but not to normal cells⁵⁴. In fact, the dose dependent assay in the present work (Figure 3.10) evidenced that also the non-doped NPs can become cytotoxic provided we use high NPs doses (500 µg/mL). This anti-tumor activity is generally explained by the higher metabolic activity of cancerous cells versus non-cancerous cells causing a higher degree of

NPs internalization. Moreover, for specific cancerous cells (such as human gastric cancer cells, human cervical adenocarcinoma epithelial cells and human hepatoma cells) higher levels of apoptosis have been detected owing to selective accumulation of NPs in the cell nuclei while no translocation was detected for normal cells (e.g. human normal liver cells) ⁵⁵. Once in the nuclei NPs are supposed to strongly interact with DNA or DNA-related proteins disrupting cell functions and triggering apoptosis. Another reported feature distinguishing the behavior between cancerous and normal cells was the level of intracellular Ca²⁺ measured in both cell types upon NPs internalization. It was observed that the Ca²⁺ level in cancerous cells was anomalously high but in normal cells the initially high Ca level could soon level off which explained preservation of cell viability⁵⁴. Interestingly, although our results supported the anti-tumor activity of HA-NPs, we have further proved that for MG63 this effect can be greatly enhanced by simply doping the NPs with Mg. In fact, concentrations much lower than the ones reported in the literature are needed to have a cytotoxic effect if using Mg-doped NPs. The most critical aspect is however to have the right surface charge to enable NPs internalization. rMSCs on the contrary showed good viability as only at very high doses cytotoxicity was observed.

Summing up, this work has addressed the effect of ion doping on HA in views of using doped-NPs as drugs by themselves, or as carriers of drugs or genes for cell internalization purposes. The overall results evidenced that ion doping has indeed a potential effect on cells and can be used to trigger specific cell responses. The results were however, cell dependent. The fact that a simple action such as doping could be used to selectively kill osteosarcoma cells without compromising the viability of mesenchymal stem cells can provide new means to modulate cell behavior. Although further studies are needed to understand the mechanism behind, 10M-NPs and 4M7C NPs can be foreseen to have great potential in bone cancer treatment.

3.5 Conclusions

The present work has proved that ion doping in hydroxyapatite nanoparticles has a strong impact on cell behavior. Although from a physicochemical point of view minute doping caused various changes mainly in the morphology and solubility of the different nanoparticles, none of these two characteristics affected significantly the cell behavior. In contrast, the nature of the doping ion was critical especially for MG63 cells. Minute amounts of Mg in the NPs (>1.5 wt%) led to a marked cytotoxicity on MG63 cells, but did not have any major effect on the viability of rMSCs. Although further studies would be needed to overcome specific shortcomings, this selectivity seems particularly interesting in the treatment of cancer where simple ion-doping could be exploited in replacement of current toxic drugs. Another aspect that was also put forward in the present work was the importance of the surface charge of the NPs with regards to internalization. Stabilization of a negative surface charge on the surface of the NPs was believed to prevent NPs internalization in MG63. This behavior was again cell dependent and not such an effect was observed for rMSCs. All these findings are foreseen to have great potential guiding in the design of new NPs with improved biological performance.

3.6 References

1. Monroe, E. A., Votava, W., Bass, D. B. & McMullen, J. New Calcium Phosphate Ceramic Material for Bone and Tooth Implants. *Journal of Dental Research* **50**, 860–861 (1971).
2. Fox, K., Tran, P. a & Tran, N. Recent advances in research applications of nanophase hydroxyapatite. *Chemphyschem : a European journal of chemical physics and physical chemistry* **13**, 2495–506 (2012).
3. Sokolova, V. *et al.* Calcium phosphate nanoparticles as versatile carrier for small and large molecules across cell membranes. *Journal of Nanoparticle Research* **14**, 910 (2012).
4. Epple, M. *et al.* Application of calcium phosphate nanoparticles in biomedicine. *Journal of Materials Chemistry* **20**, 18 (2010).
5. Uskoković, V. & Uskoković, D. P. Nanosized hydroxyapatite and other calcium phosphates: chemistry of formation and application as drug and gene delivery agents. *Journal of biomedical materials research. Part B, Applied biomaterials* **96**, 152–91 (2011).
6. Maitra, A. Calcium phosphate nanoparticles: second-generation nonviral vectors in gene therapy. *Expert review of molecular diagnostics* **5**, 893–905 (2005).
7. Roy, I., Mitra, S., Maitra, A. & Mozumdar, S. Calcium phosphate nanoparticles as novel non-viral vectors for targeted gene delivery. *International Journal of Pharmaceutics* **250**, 25–33 (2003).
8. Khosravi-Darani, K., Mozafari, M. R., Rashidi, L. & Mohammadi, M. Calcium based non-viral gene delivery: an overview of methodology and applications. *Acta medica Iranica* **48**, 133–41 (2009).

9. Chu, S.-H., Feng, D.-F., Ma, Y.-B. & Li, Z.-Q. Hydroxyapatite nanoparticles inhibit the growth of human glioma cells in vitro and in vivo. *International journal of nanomedicine* **7**, 3659–66 (2012).
10. Palazzo, B. *et al.* Biomimetic Hydroxyapatite–Drug Nanocrystals as Potential Bone Substitutes with Antitumor Drug Delivery Properties. *Advanced Functional Materials* **17**, 2180–2188 (2007).
11. Cheng, X. & Kuhn, L. Chemotherapy drug delivery from calcium phosphate nanoparticles. *International journal of nanomedicine* **2**, 667–74 (2007).
12. Devanand Venkatasubbu, G., Ramasamy, S., Ramakrishnan, V. & Kumar, J. Nanocrystalline hydroxyapatite and zinc-doped hydroxyapatite as carrier material for controlled delivery of ciprofloxacin. *3 Biotech* **1**, 173–186 (2011).
13. Venkatasubbu, G. D., Ramasamy, S., Reddy, G. P. & Kumar, J. In vitro and in vivo anticancer activity of surface modified paclitaxel attached hydroxyapatite and titanium dioxide nanoparticles. *Biomedical microdevices* **15**, 711–26 (2013).
14. Meena, R., Kesari, K. K., Rani, M. & Paulraj, R. Effects of hydroxyapatite nanoparticles on proliferation and apoptosis of human breast cancer cells (MCF-7). *Journal of Nanoparticle Research* **14**, 712 (2012).
15. Iafisco, M. *et al.* Cell surface receptor targeted biomimetic apatite nanocrystals for cancer therapy. *Small (Weinheim an der Bergstrasse, Germany)* **9**, 3834–44 (2013).
16. Hasna, K. *et al.* Synthesis of chemically pure, luminescent Eu³⁺ doped HAp nanoparticles: a promising fluorescent probe for in vivo imaging applications. *Physical chemistry chemical physics : PCCP* **15**, 8106–11 (2013).

17. Panseri, S. *et al.* Intrinsically superparamagnetic Fe-hydroxyapatite nanoparticles positively influence osteoblast-like cell behaviour. *Journal of nanobiotechnology* **10**, 32 (2012).
18. Tampieri, A. *et al.* Intrinsic magnetism and hyperthermia in bioactive Fe-doped hydroxyapatite. *Acta biomaterialia* **8**, 843–51 (2012).
19. Doat, a., Pellé, F., Gardant, N. & Lebugle, a. Synthesis of luminescent bioapatite nanoparticles for utilization as a biological probe. *Journal of Solid State Chemistry* **177**, 1179–1187 (2004).
20. Russin, T. J. *et al.* Near-Infrared Emitting Fluorophore-for In Vivo Imaging of Human Breast. *ACS nano* **2**, 2075–2084 (2008).
21. Müller, K. H. *et al.* The effect of particle agglomeration on the formation of a surface-connected compartment induced by hydroxyapatite nanoparticles in human monocyte-derived macrophages. *Biomaterials* **35**, 1074–88 (2014).
22. Shi, Z., Huang, X., Cai, Y., Tang, R. & Yang, D. Size effect of hydroxyapatite nanoparticles on proliferation and apoptosis of osteoblast-like cells. *Acta biomaterialia* **5**, 338–45 (2009).
23. Ding, T., Xue, Y., Lu, H., Huang, Z. & Sun, J. Effect of particle size of hydroxyapatite nanoparticles on its biocompatibility. *IEEE transactions on nanobioscience* **11**, 336–40 (2012).
24. Zhao, X. *et al.* Cytotoxicity of hydroxyapatite nanoparticles is shape and cell dependent. *Archives of toxicology* **87**, 1037–52 (2013).
25. Cai, Y. *et al.* Role of hydroxyapatite nanoparticle size in bone cell proliferation. *Journal of Materials Chemistry* **17**, 3780 (2007).
26. Chen, L., Mccrate, J. M., Lee, J. C.-M. & Li, H. The role of surface charge on the uptake and biocompatibility of hydroxyapatite nanoparticles with osteoblast cells. *Nanotechnology* **22**, 105708 (2011).

27. Sokolova, V. *et al.* Mechanism of the uptake of cationic and anionic calcium phosphate nanoparticles by cells. *Acta biomaterialia* **9**, 7527–35 (2013).
28. Xu, Z., Liu, C., Wei, J. & Sun, J. Effects of four types of hydroxyapatite nanoparticles with different nanocrystal morphologies and sizes on apoptosis in rat osteoblasts. *Journal of applied toxicology: JAT* **32**, 429–35 (2012).
29. Qing, F. *et al.* Selective effects of hydroxyapatite nanoparticles on osteosarcoma cells and osteoblasts. *Journal of materials science. Materials in medicine* **23**, 2245–51 (2012).
30. Boanini, E., Gazzano, M. & Bigi, a Ionic substitutions in calcium phosphates synthesized at low temperature. *Acta biomaterialia* **6**, 1882–94 (2010).
31. Rey, C., Combes, C., Drouet, C. & Glimcher, M. J. Bone mineral: update on chemical composition and structure. *Osteoporosis International* **20**, 1013–1021 (2009).
32. Wopenka, B. & Pasteris, J. D. A mineralogical perspective on the apatite in bone. *Materials Science and Engineering: C* **25**, 131–143 (2005).
33. Castiglioni, S., Cazzaniga, A., Albisetti, W. & Maier, J. a M. Magnesium and osteoporosis: current state of knowledge and future research directions. *Nutrients* **5**, 3022–3033 (2013).
34. Iafisco, M., Ruffini, A., Adamiano, A., Sprio, S. & Tampieri, A. Biomimetic magnesium–carbonate-apatite nanocrystals endowed with strontium ions as anti-osteoporotic trigger. *Materials Science and Engineering C* **35**, 212–219 (2014).
35. Shepherd, J. H., Shepherd, D. V & Best, S. M. Substituted hydroxyapatites for bone repair. *Journal of materials science. Materials in medicine* **23**, 2335–47 (2012).

36. Aina, V. *et al.* Magnesium- and strontium-co-substituted hydroxyapatite: the effects of doped-ions on the structure and chemico-physical properties. *Journal of materials science. Materials in medicine* **23**, 2867–79 (2012).
37. Dasgupta, S., Banerjee, S. S., Bandyopadhyay, A. & Bose, S. Zn- and Mg-doped hydroxyapatite nanoparticles for controlled release of protein. *Langmuir : the ACS journal of surfaces and colloids* **26**, 4958–64 (2010).
38. Mostafa, N. Y., Hassan, H. M. & Abd Elkader, O. H. Preparation and Characterization of Na⁺, SiO₄⁴⁻, and CO₃²⁻-Co-Substituted Hydroxyapatite. *Journal of the American Ceramic Society* **94**, 1584–1590 (2011).
39. Sader, M. S., Lewis, K., Soares, G. a. & LeGeros, R. Z. Simultaneous incorporation of magnesium and carbonate in apatite: effect on physico-chemical properties. *Materials Research* **16**, 779–784 (2013).
40. Capuccini, C. *et al.* Interaction of Sr-doped hydroxyapatite nanocrystals with osteoclast and osteoblast-like cells. *Journal of biomedical materials research. Part A* **89**, 594–600 (2009).
41. Cox, S. C., Jamshidi, P., Grover, L. M. & Mallick, K. K. Preparation and characterisation of nanophase Sr, Mg, and Zn substituted hydroxyapatite by aqueous precipitation. *Materials Science and Engineering: C* **35**, 106–114 (2014).
42. Li, Y., Nam, C. T. & Ooi, C. P. Iron(III) and manganese(II) substituted hydroxyapatite nanoparticles: Characterization and cytotoxicity analysis. *Journal of Physics: Conference Series* **187**, 012024 (2009).
43. Adams, B. R., Mostafa, A., Schwartz, Z. & Boyan, B. D. Osteoblast response to nanocrystalline calcium hydroxyapatite depends on carbonate content. *Journal of biomedical materials research. Part A* 1–6 (2013).

44. Landi, E. *et al.* Biomimetic Mg-substituted hydroxyapatite: from synthesis to in vivo behaviour. *Journal of materials science. Materials in medicine* **19**, 239–47 (2008).
45. Landi, E. *et al.* Biomimetic Mg- and Mg,CO₃-substituted hydroxyapatites: synthesis characterization and in vitro behaviour. *Journal of the European Ceramic Society* **26**, 2593–2601 (2006).
46. LeGeros, R. & LeGeros, J. Dense hydroxyapatite. *An Introduction to Bioceramics* 139–180 (1993).
47. Landi, E., Celotti, G., Logroscino, G. & Tampieri, a. Carbonated hydroxyapatite as bone substitute. *Journal of the European Ceramic Society* **23**, 2931–2937 (2003).
48. Barralet, J., Best, S. & Bonfield, W. Carbonate substitution in precipitated hydroxyapatite: an investigation into the effects of reaction temperature and bicarbonate ion concentration. *Journal of biomedical materials research* **41**, 79–86 (1998).
49. Diallo-garcia, S., Laurencin, D., Kra, J., Casale, S. & Smith, M. E. Influence of Magnesium Substitution on the Basic Properties of Hydroxyapatites. 24317–24327 (2011).
50. Cazalbou, S., Combes, C., Eichert, D. & Rey, C. Adaptive physico-chemistry of bio-related calcium phosphates. *Journal of Materials Chemistry* **14**, 2148 (2004).
51. Leeuwenburgh, S. C. G., Ana, I. D. & Jansen, J. A. Sodium citrate as an effective dispersant for the synthesis of inorganic-organic composites with a nanodispersed mineral phase. *Acta Biomaterialia* **6**, 836–844 (2010).
52. Gunawan, C., Lim, M., Marquis, C. P. & Amal, R. Nanoparticle–protein corona complexes govern the biological fates and functions of nanoparticles. *Journal of Materials Chemistry B* **2**, 2060 (2014).

53. Albanese, A. & Chan, W. C. W. Effect of gold nanoparticle aggregation on cell uptake and toxicity. *ACS nano* **5**, 5478–89 (2011).
54. Pedraza, C. E. *et al.* The importance of particle size and DNA condensation salt for calcium phosphate nanoparticle transfection. *Biomaterials* **29**, 3384–92 (2008).
55. Tang, W., Yuan, Y., Wu, Y. & Lu, X. Differential cytotoxicity and particle action of hydroxyapatite nanoparticles in human cancer cells. *Nanomedicine* **9**, 397–412 (2013).
56. Yuan, Y., Liu, C., Qian, J., Wang, J. & Zhang, Y. Size-mediated cytotoxicity and apoptosis of hydroxyapatite nanoparticles in human hepatoma HepG2 cells. *Biomaterials* **31**, 730–40 (2010).

Chapter 4

Effect of minority ions doping in HA nanoparticles: Strontium, Zinc, Silicon and Iron

In **Chapter 3**, magnesium and carbonate ions were introduced to synthesize ion-doped HA nanoparticles and their impact on different cell types was investigated. The results were very promising and they proved that ion doping could be used as a strategy to modulate cell behaviour. This finding has been the motivation to explore a new series of ion doped HA nanoparticles but this time using as doping ions elements present in bone mineral at very low concentrations. Would still ion doping affect cell behaviour? And, how differently would each NP behave?

4.1 Introduction

As it was already proved in **Chapter 3**, ionic substitutions in HA NPs can influence cell behaviour and this response is cell-specific. This was readily shown for Mg, where Mg ion-doped HA NPs were found to be cytotoxic to MG63 cells but not to rMSCs while CO₃ in HA NPs did not alter cell viability. However, aside from Mg and carbonate ions there are many other ions in biological apatite, such as strontium (Sr), zinc (Zn), silicon (Si) and iron (Fe) that are involved in several biological functions. Even though these ions have a negligible portion in bone tissue (see table 2.2; e.g. Zn making up 0.0039 wt % of bone) in comparison with Mg (making up ~1 wt % of bone) and CO₃ (making up 4.8% of bone), they also play very important roles in bone formation and metabolism as well as in human health. Sr for instance, has been indicated to promote bone formation *in vivo* by enhancing

pre-osteoblasts cell replication and osteoblasts differentiation. This fact, has attracted in the past a remarkable interest and has been used as candidate for enhancing bone healing due to its therapeutic effect on osteoporotic bone¹⁻³. Zn ions were also found to stimulate bone growth by inhibiting osteoclast differentiation and promoting osteoblast activity^{4,5}. In addition to the role in bone tissue formation, Zn ions are known to act as a cofactor for more than 300 enzymes and are involved in many biological processes including cell growth and DNA synthesis⁶. It has been reported that zinc ions promote the proliferation of several types of cells and severe depletion of zinc also has profound effects on cell physiology^{7,8}. Silicon is also known to be essential as a trace element in biological processes, and in particular, it has been reported to have a specific metabolic role connected to bone growth and osteoporosis prevention⁹. Regarding the role of iron in the human body, it has been generally recognized that iron is required for the production of red blood cells, but it's also part of haemoglobin (that is the pigment of the red blood cells) binding to the oxygen and thus facilitating its transport from the lungs throughout the body¹⁰. A few studies also showed that iron restriction had an inhibitory effect on the mineralization of osteoblasts *in vitro*, and experimental evidence also suggested that there may be some positive association between iron metabolism and the *in vitro* proliferation of bone or non-bone cell lines^{11,12}.

Up to date, there have been numerous studies with the aim of using ion substituted-HA bulk materials (i.e. Sr, Zn, Si and Fe) to improve bone regeneration¹²⁻¹⁹. For example, Capuccini *et al.*²⁰ suggested that Sr substitution in HA materials significantly increased the proliferation of osteoblast cells and enhanced cell differentiation. *In vitro* studies by Thian *et al.*⁴ showed that Zn-doped HA materials enhanced the growth of mesenchymal stem cells (MSCs) as well as the differentiation of MSCs to bone cells. Another study by Shepherd *et al.*⁵ showed that Zn-substituted hydroxyapatite inhibited osteoclast proliferation. In addition, Botelho and co-workers²¹ demonstrated that Si-doped HA increased the levels of osteoblast markers like collagen type I, alkaline phosphatase and osteocalcin when contrasted to the undoped samples. Patel *et al.* compared the performance of Si-substituted HA with undoped granules after being implanted in rabbits for a short

time period, proving that the bioactivity of HA was significantly improved with the incorporation of silicon²².

However, investigations targeting the effect of these ions in NPs for future use in gene/drug delivery are scarce, in spite of the promising–yet limited results–already available.

4.2 Objectives

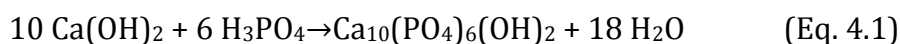
In line with the previous chapter, the goal in Chapter 4 is to synthesize hydroxyapatite nanoparticles doped with small amounts of minority metal elements relevant in the body and investigate their effect through *in vitro* cell culture studies. More specifically, this chapter tackles:

- Preparation and exhaustive characterization of NPs doped with various doses of strontium (Sr), zinc (Zn), silicon (Si) and iron (Fe) ions.
- Cell culture studies using two different cell types (osteosarcoma cells, MG-63 and rat mesenchymal stem cells, rMSCs) in the presence and absence of 10 v/v% of foetal bovine serum (FBS) in cell culture media

4.3 Materials and methods

4.3.1 Synthesis of ion-doped HA nanoparticles

All HA-NPs were synthesized by neutralization of $\text{Ca}(\text{OH})_2$ with H_3PO_4 (Eq. 4.1) at 40 °C in air atmosphere. The temperature was controlled by means of a thermal bath (Huber Kältemaschinenbau GmbH, Germany) and the reaction was performed on thermo-jacketed vessels connected to the bath. The pH was continuously monitored throughout the reaction.



The synthesis reaction of the non-doped NPs was carried out as follows. 100 mL of 0.334 mol/L $\text{Ca}(\text{OH})_2$ (Fluka, 96 wt% pure) was first prepared and then a 0.2 M H_3PO_4 (Panreac, 85 wt% pure) solution was added dropwise into the system at the constant rate of 1ml/min under constant stirring. The reaction was stopped when the pH reached 8. Next, the suspension was left stirring for 20-30 min and was then transferred into a glass bottle where it was left maturing overnight at room temperature. On the next day the suspension was rinsed with Milli-Q water till constant conductivity following cycles of 5 min centrifugation at 800 g (Beckman Allegra 21 Benchtop Centrifuge)/re-suspension. Afterwards the product was frozen at -80°C and lyophilized (Telstar Cryodos). Once lyophilized the powder was kept in a desiccator.

Ion doped nanoparticles were prepared using the same experimental procedure as that used for the synthesis of undoped HA but with pre-dissolving various concentrations of the salt of interest either in $\text{Ca}(\text{OH})_2$ (e.g. $\text{SrCl}_2 \cdot 6\text{H}_2\text{O}$ -Sigma, 99 wt%, ZnCl_2 and $\text{FeCl}_3 \cdot 6\text{H}_2\text{O}$ -Panreac, 98 wt%) or the H_3PO_4 (e.g. tetraethyl orthosilicate- $\text{Si}(\text{OCH}_2\text{CH}_3)_4$ (TEOS; Sigma, 99 wt%)) before titration. Various salt concentrations ranging from 1 to 20 wt% were explored. To get the desired weight percent of foreign ions in hydroxyapatite, the amount of reagents that needed to be mixed with $\text{Ca}(\text{OH})_2$ or H_3PO_4 was calculated according on the assumption that metal ions would substitute Ca sites and silicate would substitute phosphate.

The different NPs were designated as follows:

HA: non-doped NPs,

5Sr, 10Sr, 20Sr: strontium doped HA-NPs (5, 10 and 20 wt% respectively)

1Zn, 5Zn, 10Zn: zinc doped HA-NPs (1, 5 and 10 wt% respectively)

1Si, 2Si, 4Si: silicon doped HA-NPs (1, 2 and 4 wt% respectively)

1Fe, 5Fe, 10Fe: iron (III) doped HA-NPs (1, 5 and 10 wt% respectively)

4.3.2 Characterization of ion-doped HA nanoparticles

The phase composition was determined by X-ray powder diffraction (XRD), using a D8 Advance Diffractometer (Bruker, Karlsruhe, Germany) with CuK α radiation at 40 kV and 40 mA. XRD spectra were recorded in the range 10–80 $^{\circ}$, with a step size of 0.02 $^{\circ}$ and a counting time of 1 s. The crystallite size perpendicular to the (hkl) plane was calculated by Scherrer formula as follows:

$$X_{hkl} = K\lambda/\beta_{1/2}\cos\theta \quad (\text{Eq. 4.2})$$

Where X_{hkl} is the crystallite size (nm), λ is the wavelength of monochromatic X-ray beam (nm) ($\lambda = 0.15418$ nm for CuK α radiation), $\beta_{1/2}$ is the full width at half maximum (FWHM) for the diffraction peak under consideration (rad), ' θ ' is the diffraction angle (in degrees), and 'K' is a constant varying with crystal habit and chosen to be 0.9. With regards to the crystallinity degree of samples (X_c) which is defined as the fraction of the crystalline phase in a sample volume it was deduced according to the following equation:

$$X_c = (K/\beta_{1/2})^3 \quad (\text{Eq. 4.3})$$

Where K is a constant set at 0.24 and $\beta_{1/2}$ is the FWHM of the peak reflection (in degrees). Both, the crystallite size of the NPs as well as their corresponding crystallinity degree were evaluated using the line broadening of the (002) reflection, because this peak is well resolved and shows no interferences with nearby reflections.

Fourier transformed infrared spectroscopy (FTIR) in the ATR mode (Attenuated Total Reflectance mode, Nicolet 6700 spectrometer, Thermo Scientific) was used to check the typical functional groups present in apatite and, in particular, the presence of silicate bands in the powders. All the spectra were obtained by averaging 32 scans collected in the range 500–4000 cm^{-1} , with a spectral resolution of 4 cm^{-1} .

Quantitative inductively coupled plasma–optical emission spectrometry analysis (ICP-OES, Perkin Elmer Optima 3200RL), was applied to determine the overall content of Ca, P, Zn, Fe, Sr and Si. Samples were prepared dissolving 100 mg of powder in 5 mL of 10 wt% HNO_3 (Panreac, 69 wt% pure) which was then 10 or 20-fold diluted.

The specific surface area (SSA) of the NPs was determined from the nitrogen adsorption data in the relative pressure range (P/P_0) from 0.05 to 0.35 by using the Brunauer-Emmett-Teller (BET) method with the ASAP2020 physisorption analyzer (Micromeritics, Norcross, GA, USA). The sample was outgassed at 120 °C before analysis.

The skeletal density of nanoparticles was measured by helium pycnometry (Micromeritics' AccuPyc II 1340 Gas Pycnometer). Prior to measurement all NPs were dried in an oven at 120 °C for 8 hours to remove moisture.

The morphology of the NPs was assessed by transmission electron microscopy (TEM, JEOL 1010). Samples for TEM examination were prepared by soaking a 300 mesh carbon-coated copper grid in the solution of interest, blotted to remove the excess liquid and air dried.

The apparent solubility of the NPs was evaluated by monitoring the conductivity changes (Crison MM41) of a 0.1 mol/L acetate buffer solution (25 °C, pH=5.5) containing 1 mg/mL of NPs with time.

4.3.3 Preparation and characterization of NPs suspensions

For the preparation of the suspensions 0.1g of nanoparticles were suspended in 10 mL Milli-Q water with the help of an ultrasound probe sonicator (Branson Digital, Model 250W) using the following settings/conditions: 3 mm diameter tip, 40 % amplitude (~50 Watts) and 2 minutes of sonication (with cycles of 15 sec sonication followed by 10 sec pause to prevent excessive heating) in an ice bath. The surface charge of the NPs was determined by measuring the zeta potential (ζ -potential) in water with a Zetasizer Nano-ZS (Malvern Instruments Ltd., UK). The result was expressed as a mean \pm standard deviation of three measurements.

4.3.4 *In vitro* cell culture studies

4.3.4.1 Cell culture

Human osteoblast-like MG63 cell line and rat mesenchymal stem cells (rMSCs) were cultured in Dulbecco's modified Eagle medium (DMEM) and advanced-DMEM, respectively, supplemented 10v/v% fetal bovine serum (FBS), penicillin/streptomycin (50 U/mL and 50 μ g/mL, respectively), 2 mmol/L L-glutamine and 20 mmol/L HEPES buffer at 37 °C in an atmosphere of 5% CO₂. When the cells attained confluence, they were detached using 0.25% Trypsin and seeded onto standard polystyrene tissue culture plates (96 wells) at a cell density of 1×10^4 cells/well. The seeded cells were incubated overnight to allow cell adherence at 37 °C in 5% CO₂ atmosphere.

4.3.4.2 Exposure of cells to doped and undoped samples

Both MG63 and rMSCs Cells were exposed to all NPs (dispersed in water) in two different scenarios: in cell culture media supplemented with 10 v/v% FBS and without FBS. The appropriate volume of NPs from the stock (1 wt% NPs in water) was added to the corresponding cell culture media to make a final concentration of 100 μ g/mL. Before adding the suspensions of NPs to the cells the mixture was vortexed to homogenise it. The time period for cells incubated with NPs was set to 24 h. For selected compositions (i.e., HA and 10Zn NPs) the same experiment was performed with MG63 cells using transwells (6.5 mm Transwell with 0.4 μ m pore polyester membrane insert for 24 well plates from Sigma) by placing the NP

suspension in the transwells to prevent direct contact of the NPs with the cells but allowing any ionic exchange through the transwell membrane. The number of cells seeded on the 24 well plates was 2.5×10^4 cells/well and the concentration of NPs used was kept to 100 $\mu\text{g}/\text{mL}$. For comparison purposes NPs were also cultured in direct contact with the cells in the 24 well plates without the transwell system. The MG63 cells were also incubated for 1 day in the absence or presence of different concentrations of ZnCl_2 salts under the same conditions as above.

To study the effect of NPs dose on cytotoxicity both for MG63 and rMSCs cells, the amount of 10Zn NPs in cell culture media was increased following the concentrations: 100, 250, 500, 1000 $\mu\text{g}/\text{mL}$. And time-dependent cytotoxicity test was performed with MG63 cells with 100 $\mu\text{g}/\text{ml}$ of 10Zn NPs in the absence or presence of FBS at three time point: 1day, 2days and 3days. Non-doped HA was also included as control. For the 3 days cell culture with HA and 10Zn NPs, the MG63 cells were also incubated with NPs in the absence of FBS for the first 6 hours of incubation, afterwards, 10 v/v% FBS was supplemented.

4.3.4.3 Cytotoxicity test

For the cytotoxicity evaluation of the various NPs the cell culture medium was removed after the 24 h incubation time and then viable cells attached on the surface of polystyrene tissue culture plates were lysed adding 100 μL of mammalian protein extraction reagent (M-PER, Thermo Scientific Inc., USA). Upon lysis cells released lactate dehydrogenase (LDH) that was measured using a commercially available kit (Cytotoxicity Detection Kit^{PLUS}, Roche, USA) following the manufacturer instructions. The absorbance at 492 nm was quantified on a micro spectrophotometer (PowerWave XS, Bio-Tek Instruments, USA) and the percentage of viability was calculated by the following equation:

$$\text{viability}\% = \frac{\text{exp. value} - \text{negative control}}{\text{positive control} - \text{negative control}} \times 100 \quad \text{Eq. 4.4}$$

Where the 'positive control' was the absorbance value of cells incubated in cell culture medium under the same conditions of the experimental value but without

NPs and the 'negative control' corresponded to the absorbance of the well without NPs and without cells. The studies done in triplicate were expressed as mean \pm standard deviation. Statistical significance was accepted at a level of $p < 0.05$.

4.4 Results and discussion

4.4.1 Effect of ion doping on physicochemical properties

4.4.1.1 Phase characterization

The results from XRD characterization of the synthetic undoped and doped HA nanoparticles are presented in Figure 4.1a-d. All XRD patterns regardless of the type of NPs confirmed the presence of only one phase, i.e. hydroxyapatite that matched with the standard JCPDS reference (09-432) file for synthetic HA. Since no secondary phases were detected this proved that the NPs obtained were phase pure. However, in comparison with the control HA, the XRD patterns of the as-synthesized Zn-doped HA (Figure 4.1b) and Fe-doped HA samples (Figure 4.1d) exhibited broadening of all peaks becoming more obvious with the increase in Zn and Fe content (e.g., (002) (25.8°), (211) (31.7°), (112) (32.1°), (300) (32.9°), (310) (39.8°) and (004) (53.1°)). In fact, for Fe-doped NPs, besides peak broadening the intensity of the peaks became significantly lower with the increase in Fe. These features are associated to a loss in crystallinity.

Another interesting feature to observe is if there was any shift in the (002) reflection with the type of ion-doping and its dose (Figure 4.1). It is well known that the displacement of calcium by another metal ion produces changes in bond lengths, deforms the crystalline structure, and this in turn lead to peak shifting as often reported for the (002) reflection²³. The consequences of this crystal deformation results in a loss in the chemical stability of hydroxyapatite. A careful look at the (002) diffraction peak showed a gradual shift with the addition of ions depending on the type of ion. For example, the diffraction peaks of Sr-doped HA shifted to lower 2θ values with Sr addition (i.e. lattice expansion), which is explained by the result of larger ions substitution for Ca ions in the structure of HA; the ionic radius of Sr^{2+} and Ca^{2+} being 0.118 nm and 0.099nm, respectively^{24,25}. Moreover, a slight shift of the Si-doped HA peaks to lower 2θ angles compared to undoped HA (Figure 4.1c), is also ascribed to the substitution of PO_4^{3-} tetrahedra by SiO_4^{4-} tetrahedra resulting in a small increase in the lattice parameters of the unit cell^{26,27}. There was however no clear trend in the shifting of the (002) diffraction peak for Zn-doped HA and Fe-doped HA even if other authors clearly

reported it^{12,28,29}. This seemed to point that these two types of ions could not be incorporated inside the lattice of HA, and thus the lattice parameters were altered.

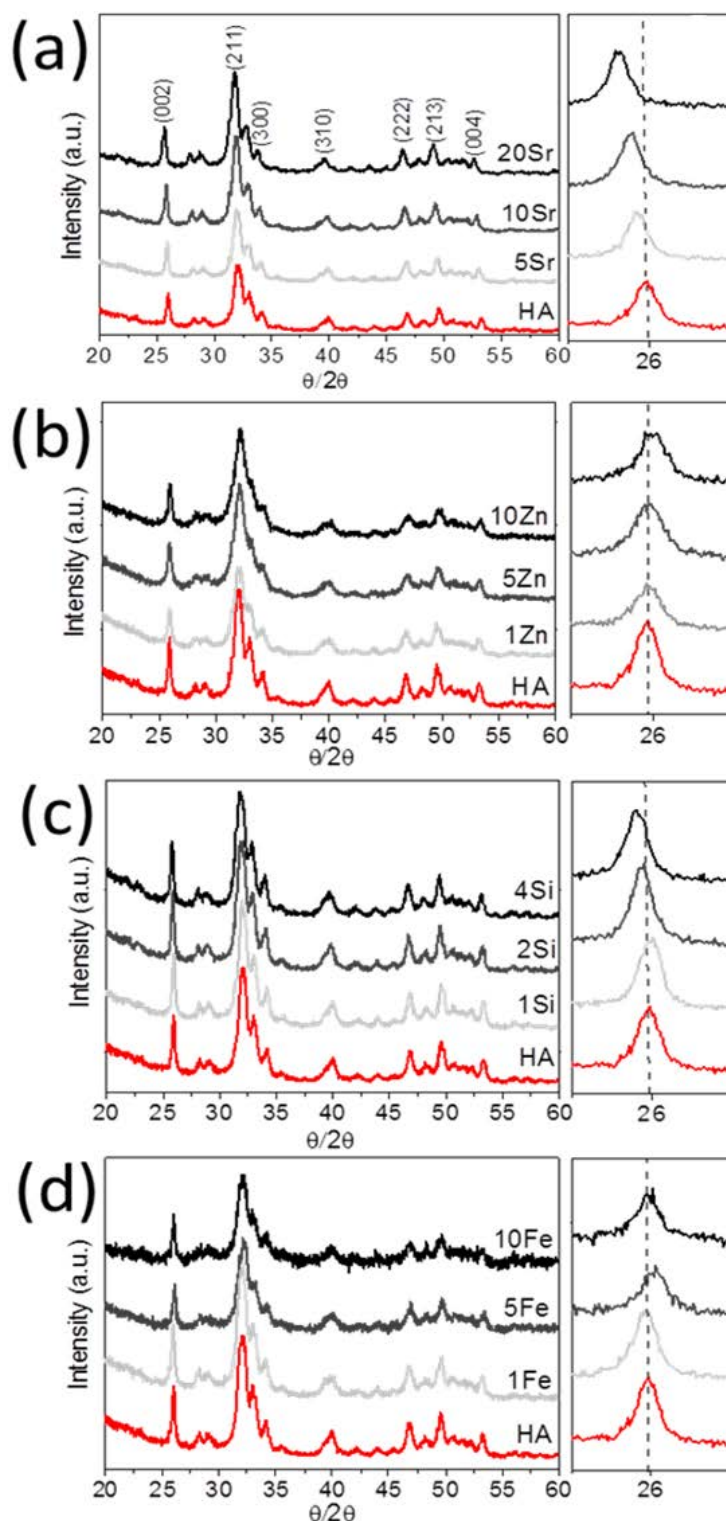


Figure 4.1 X-ray diffraction patterns of as-prepared HA and ion-doped HA over the range of 20° to 60° 2θ . (a) Sr-doped HA, (b) Zn-doped HA, (c) Si-doped HA and (d) Fe-doped HA.

The calculation of the crystallite size and crystallinity of undoped and doped hydroxyapatite NPs are shown in Table 4.1. It is interesting to note that even though Zn and Fe-doping did not seem to cause any distortion in the crystal lattice, these ions were found to cause a marked decrease in both, crystallite size and crystallinity of the nanoparticles with the content of the doping ion. No such an obvious trend could be ascribed to Sr and Si-doped NPs with ion dose although there was also a general decrease in crystallinity for these-doped HA NPs. This later observation for Sr-doped HA samples was in agreement with a reported study in which the addition of Sr caused a decrease in crystallinity when Sr substitution was lower than 50 at.%¹⁹.

Table 4.1 Crystallite size and crystallinity of all samples.

Samples	Line (002)FWHM (°)	width (002)FWHM (rad)	Average size (nm)	crystal Crystallinity (Xc)
HA	0.281	0,0049	29.0	0.623
5Sr	0.288	0.0050	28.3	0.579
10Sr	0.286	0.0049	28.5	0.591
20Sr	0.313	0.0055	26.1	0.451
1Zn	0.339	0.0059	24.1	0.355
5Zn	0.406	0.0071	20.1	0.206
10Zn	0.416	0.0073	19.6	0.192
1Si	0.304	0.0053	26.8	0.492
2Si	0.322	0.0056	25.3	0.414
4Si	0.318	0.0055	25.6	0.430
1Fe	0.343	0.0060	23.8	0.342
5Fe	0.388	0.0068	21.0	0.237
10Fe	0.427	0.0074	19.1	0.178

One aspect to take into account in the interpretation of these complex results is that there are different mechanisms that can intervene during NP precipitation in the presence of doping ions: on one hand the doping ion can be actively involved in crystal precipitation and could end up forming part of the crystal lattice but, on the other hand, the doping ion might simply adsorb on the crystal surface disturbing crystal growth but without “necessarily” becoming incorporated within the

structure. In both cases the presence of the doping ion either in the crystal structure or on the crystal surface could affect crystallite size and crystallinity. The well-known role of Zn ion inhibiting HA crystal growth could thus explain the marked decrease in crystallinity by ion adsorption²⁸, yet it is not clear why it did not get incorporated into the crystals lattice.

4.4.1.2 Functional group determination

The FTIR spectra collected for the undoped and doped NPs are shown in Figure 4.2. All characteristic bands of HA are readily visible in all of the spectra.

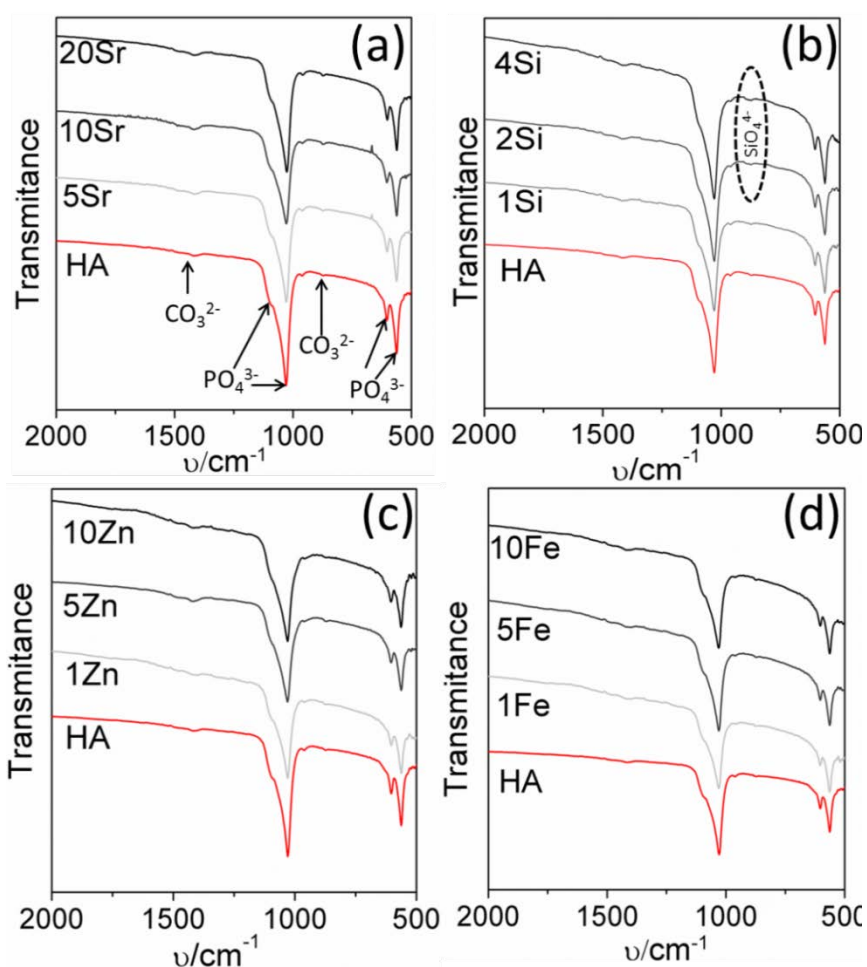


Figure 4.2 FTIR spectra of the ion-doped HA nanoparticles: a) Sr-doped HA, b) Zn-doped HA, c) Si-doped HA, d) Fe-doped HA.

Typically, vibration band for the symmetric stretching vibration (ν_1) of phosphate was centered at 962 cm^{-1} ; the bands at 1036 and 1091 cm^{-1} are the characteristic bands of asymmetric (P-O) stretching vibration of PO_4^{3-} ; and the peaks for the ν_4

bending of phosphate were observed at 603 and 562 cm^{-1} .³⁰ The band at about 1430 cm^{-1} was ascribed to the asymmetric stretch vibration of CO_3^{2-} group in B-type, and the out-of-plane bend vibration, ν_2 , close to 870 cm^{-1} .³⁰ The presence of traces of CO_3^{2-} may arise from the reaction between carbon dioxide in the reaction vessel and the impurities from the reagents during the synthesis process. It is quite evident that all of the samples show only the typical bands of a pure HA composition, with only trace amounts of CO_3^{2-} . Similarly to the broadening of the peaks that were observed by XRD, the poor crystallinity of the NPs results, in FTIR, in poorly resolved and broader bands.

Si-doped NPs were the only type of NPs that should show additional bands arising from the presence of silicate incorporation. As shown in the FTIR spectra of Si-doped HA NPs in Figure 4.2b, the band at around 870 cm^{-1} which is ascribed to the bend vibration of CO_3^{2-} became broader as the concentration of ion doping increased. This feature suggested the substitution of phosphate for SiO_4^{4-} as according to the literature Si-O vibration modes of SiO_4^{4-} groups appears at 870 cm^{-1} as well³¹.

4.4.1.3 Microstructural examination

It is well known that the shape, size and specific surface area of HA nanoparticles are very sensitive to the reactant addition rate, and to the reaction temperature when using wet chemical precipitation methods to prepare HA nanoparticles³². Moreover, it is not new that the incorporation of foreign ions during synthesis can further affect these features by virtue of e.g. adsorbing onto specific crystallographic planes altering crystal growth³³.

Figure 4.3 compiles the images for all the different synthesized NPs and it can be seen that regardless of the type and dose of doping ion incorporated in the NPs they all share the same morphology which is needle-like. It can thus be concluded that the doping ion had little influence on the morphology of NPs as in all cases they kept their needle-like structure. However, the dimension of the needle-like NPs differed depending on the type of ion and its dose. For Zn-doped HA and Fe-doped HA NPs, the needle-like NPs became shorter and thinner as the ion

concentration increased. Overall, TEM images indicated that the morphology of the apatite crystals was affected slightly by the ionic substitution into HA.

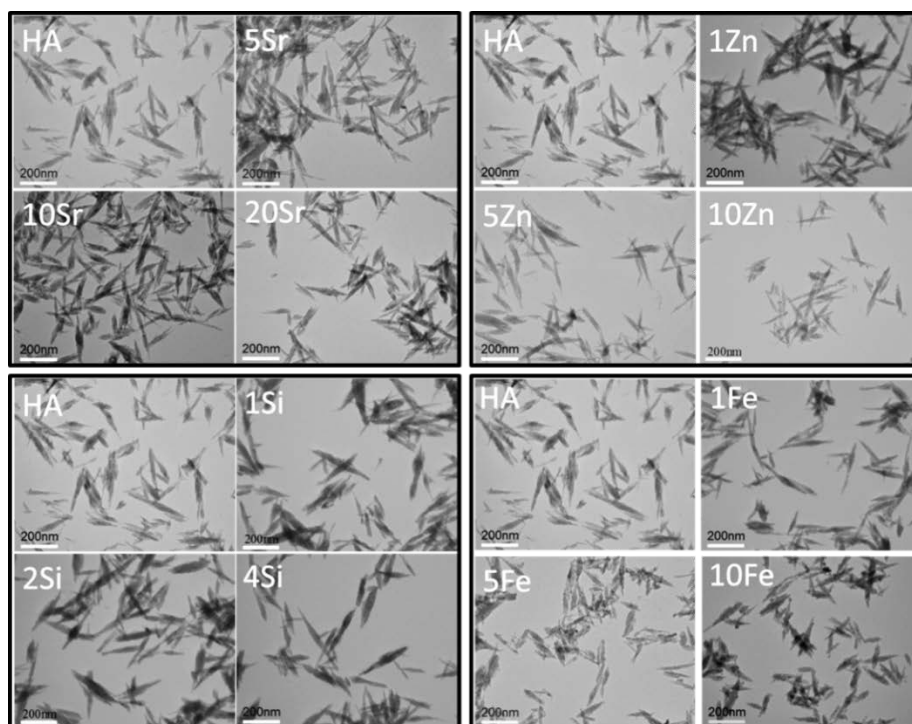


Figure 4.3 Morphologies of doped and undoped nanoparticles observed by TEM.

4.4.1.4 Specific surface area, surface charge and density of NPs

The results from determination of the specific surface area (SSA) of the NPs clearly confirmed the observations made by microstructural examination of the NPs (Table 4.2). By inspection of SSA data reported in Table 4.2, it is readily visible that the presence of Zn and Fe ions caused an increase in SSA of the NPs, and this was enhanced with dose. Thus, the SSA values of 10Zn ($138 \text{ m}^2/\text{g}$) and 10Fe ($145 \text{ m}^2/\text{g}$) are clearly greater than the value of undoped HA ($105 \text{ m}^2/\text{g}$). However, Sr-doped HA and Si-doped HA nanoparticles had similar SSA value regardless of the doping content (around $100 \text{ m}^2/\text{g}$) to that of HA. With regards to the skeletal density evaluated by He pycnometry it was shown that the density increased with Zn, Fe, Sr addition due to the replacement of a heavier ion for Ca in the crystal structure of HA (this should be the case for Sr-doped NPs) or simply to the adsorption of the heavier metal on the surface of the crystal (presumably for Zn and Fe-ion doped NPs), whereas the density of Si-doped HA kept unchanged compared to that of HA because of the similar atomic mass between phosphate and silicate.

Table 4.2 SSA and density of NPs

Samples	SSA (m ² /g)	Densities (g/cm ³)	ζ-potential (mV)
HA	105	2.80 ± 0.01	2.5±0.1
5Sr	104	2.82± 0.02	2.8±0.1
10Sr	95	2.88± 0.02	2.5±0.1
20Sr	106	2.91± 0.01	1.8±0.2
1Zn	128	2.81 ± 0.02	-0.3±0.1
5Zn	138	2.87 ± 0.02	-1.2±0.1
10Zn	137	2.95 ± 0.03	-4.7±0.2
1Si	95	2.81± 0.01	1.6±0.1
2Si	95	2.82± 0.03	2.0±0.1
4Si	92	2.82± 0.01	0.3±0.1
1Fe	108	2.79± 0.02	2.7±0.3
5Fe	134	2.86± 0.02	1.3±0.1
10Fe	145	2.94± 0.02	-1.7±0.1

The results from analysis of the surface charge (zeta potential) measured in water for all NPs revealed that all values lied close to neutral thus making difficult to ascribe any significant difference to ion doping. Since it is generally well established that particles with a high zeta potential exceeding ± 30 mV are needed to form stable suspensions, the close-to-neutral values that have been obtained point that agglomeration will occur in solution due to electrostatic attraction³⁴.

4.4.1.5 Elemental analysis

Analysis of the chemical composition of the various ion-doped HA nanoparticles determined by ICP-OES are shown in Table 4.3. The amount of doping ion measured for the different NPs showed two main trends: on the one hand it was observed that Fe and Zn doped NPs incorporated almost the whole amount of ions supplied during the synthesis, while Sr and Si had only incorporated half the amount supplied for the highest doping dose. Although a priori Fe³⁺, Zn²⁺, Sr²⁺ and SiO₄ could potentially be incorporated into the NPs, the results need to be analysed with care to explain the differences in “uptake”. It has been reported that Sr ions could replace Ca in the structure of HA over the whole range composition, while Zn

substitution for Ca ions occurs up to about 20 at.%¹⁹. For Fe³⁺ it is known that preferentially replaces Ca II from HA²⁹ and for silicate it has been reported that the maximum uptake is 5 wt%³⁵.

Table 4.3 Elemental Analysis for the Ions-Doped and Undoped HA Samples

Samples	Ca	P	Sr	Zn	Si	Fe	(M+Ca)/P or	
	(wt%)	(wt%)	(wt%)	(wt%)	(wt%)	(wt%)	Ca/P	Ca/(P+N) M=Sr,Zn,Fe; N=Si
HA	35.82±1.07	16.11±0.81					1.72	
5Sr	34.22	16.05	3.54				1.65	1.73
10Sr	31.78±0.87	15.08±0.34	5.70±0.28				1.63	1.76
20Sr	29.14	14.45	8.57				1.56	1.78
1Zn	36.48	17.02		0.73			1.66	1.68
5Zn	32.90±0.12	15.21±0.21		3.98±0.05			1.66	1.82
10Zn	30.09±0.77	14.15±0.12		8.04±0.37			1.60	1.96
1Si	36.94±0.86	16.13±0.52			0.77±0.12		1.78	1.69
2Si	36.48±0.47	15.16±0.18			1.4±0.39		1.86	1.70
4Si	39.03	16.42			2.34		1.85	1.58
1Fe	33.50±1.36	15.47±0.46				0.97±0.03	1.74	1.75
5Fe	33.45±0.30	14.98±0.84				4.98±0.30	1.76	1.94
10Fe	30.48±0.34	13.45±0.29				10.6±0.28	1.77	2.21

To gain some insights into the ion-incorporation mechanism, Table 4.3 compares the (Ca+Metal)/P ratio and the (Ca/P+Silicate) for the different ion-doses. For the case of Sr-doping it is clearly observed that increasing the amount of Sr did not alter the (Ca+Sr)/P ratio significantly, which pointed that all Sr ions were incorporated into the HA crystal lattice. These results were plausible with the observation by XRD diffraction of the shift of the (002) reflection which indeed pointed to the introduction of Sr into the lattice (Figure 4.1a). For the case of silicon, XRD also showed a clear shift in the (002) reflection, yet, ICP results were not easy to interpret. The reason for this could be the charge imbalance between PO₄³⁻ and SiO₄⁴⁻. Since it is mandatory to preserve the local charge neutrality, defects will need to be incorporated to compensate for the charge deficit which makes it more difficult interpretation of the Ca/P³⁶.

Interestingly NPs doped with Zn and Fe behaved differently. In fact, for Zn-doped HA NPs the Ca+Metal/P increased with ion doping meanwhile the Ca/P was decreased from 1.72 to ~ 1.66 in comparison with the control HA. This suggested that only parts of Zn ions were incorporated into the crystal lattice of apatite by replacing Ca ions sites, while the others could just adsorb on the crystal surface. However, for Fe-doped HA NPs the molar ratio of Ca+Metal/P increased but Ca/P maintained regardless of the content of doping ion incorporated. The preservation of the Ca/P pointed that Ca was not being substituted thus seeming to point that Fe ions were being adsorbed on the surface of the NPs. These results were consistent with the X-Ray diffraction results that did not show any displacement of the (002) reflection (Figure 4.1d).

One aspect worth mentioning is the deviation in stoichiometry (Ca/P=1.67) of the control HA NPs (Ca/P=1.72). This deviation is explained by the presence of CO_3^{2-} ions substituting phosphates in the crystal lattice of HA (evidenced by FTIR) that leads to higher Ca/P values than stoichiometric.

4.4.1.6 Apparent Solubility of NPs

One of the important consequences that ion doping can impart on the NPs is the change in the NPs solubility. Conductivity measurements are routinely used in many industrial and environmental applications as a fast, inexpensive and reliable way of measuring the ionic content in a solution. The conductivity curve of a water-based suspension of nanoparticles has been shown to be useful as a preliminary indirect evaluation of the solubility of the different apatites³⁷. Thus, in the present study, the apparent solubility of undoped and doped samples was measured by monitoring the conductivity change as a function of time in an acetate buffer solution. Figure 4.4 shows the results for three different batches of HA NPs in buffer solution. It is clearly shown that conductivity of HA increased with time at the beginning of incubation and kept stable once it reached equilibrium. The conductivity curves overlapped suggesting that this method to measure apparent solubility was applicable and reproducible.

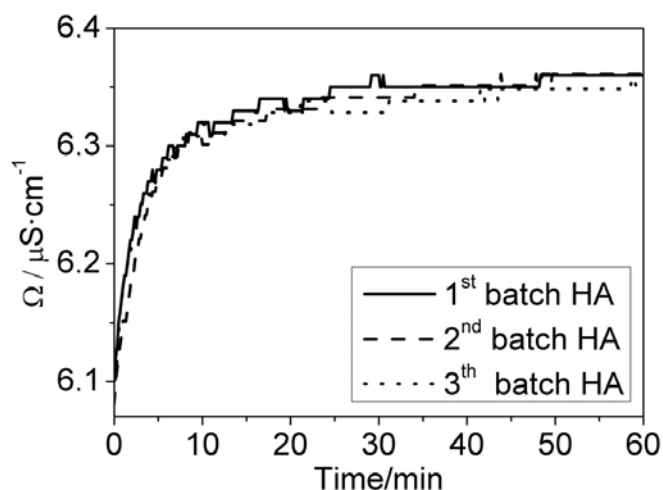


Figure 4.4 Conductivity curves of three different batches of HA changed over time in acetate buffer (pH=5.5, 25°C).

The results for the various ion-doped NPs are shown in Figure 4.5. It is clear that the apparent solubility of the Sr-doped HA and Si-doped HA increased with ion addition (Figure 4.5a and c), whereas the solubility of Zn-doped HA and Fe-doped HA decreased in comparison to that of the control HA NPs (Figure 4.5b and d) and in spite of their marked decrease in crystallinity (Figure 4.1 and Table 4.1).

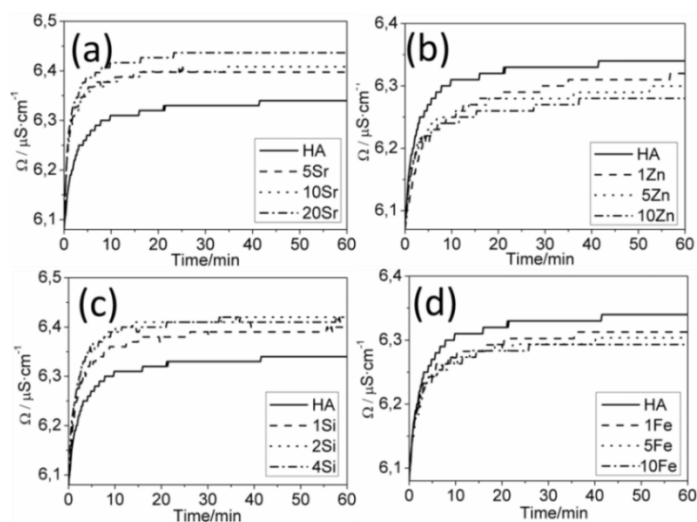


Figure 4.5 Conductivity curves of all doped and undoped NPs in acetate buffer (pH=5.5, 25°C) change with time, which represents apparent solubility of NPs.

The incorporation of Sr and silicon into the crystal structure of HA, evidenced by XRD (Fig. 4.1a), can easily lead to distortion of the crystal lattice which would explain the enhanced solubility of the doped NPs. In contrast, for Zn and Fe doped NPs it was believed that these ions were adsorbed on the NPs surface, probably

forming an amorphous dense layer, which might be the responsible for the decreased solubility. In fact, in HA powders with low crystallinity it has been confirmed the formation of a thin layer of disordered matter surrounding the NPs³⁸. Even though the surface composition of Fe and Zn doped NPs has not been investigated in depth, it is reasonable to think that their scarce crystallinity facilitates the formation of an amorphous layer surrounding the more 'crystalline' core as a result of ions absorption on the crystal surface of NPs. And this amorphous layer could dissolve very fast from NPs, leaving a more stable and less soluble core.

The variation tendency for the solubility of Sr-doped HA was in good agreement with other reports found in the literature where the solubility of Sr-substituted HA increased with the increase in strontium content³⁹. In addition, the decreased solubility for Fe-doped HA has also been ascertained in the study by Okazaki *et al*⁴⁰.

4.4.2 Effect of ion doping on cell behaviour

The potential of any of the ion-doped NPs as carriers of genes or drugs for future gene transfection and drug delivery applications needs to be assessed by a thorough *in vitro* characterization. Thus, similarly to what was done in the previous chapter, the cytotoxicity of all the NPs was assessed in view of analyzing if the nature of the doping ion has any effect in the cytotoxicity of cells. In spite of the fact that all the synthesized NPs were needle-like, features such as solubility, SSA and crystallinity varied between NPs thus, results were closely analyzed taking into account all these variations.

4.4.2.1 Cytotoxicity of NPs in MG63 cells

The viability of MG63 cells determined by LDH assay is shown in Figure 4.6. The results clearly showed that under physiological conditions, i.e. in the presence of FBS (+FBS), none of the NPs were cytotoxic to MG63 cells. However, similarly to what was already observed in the previous chapter, NPs exhibited different degrees of cytotoxicity in the absence of FBS (-FBS). This distinct behaviour is believed to be caused by the great affinity that proteins from the serum have for

hydroxyapatite. Routine cell culture studies are always supplemented with FBS, which contains essential nutrients and growth factors, to promote the proliferation of cells. Therefore when NPs are immersed into the cell culture medium containing FBS, proteins would rapidly adsorb on their surface and this could have a significant impact on cell behavior i.e. cellular uptake of NPs. In fact, in the previous chapter it was already disclosed that the negative charge that proteins confer to the NPs prevented internalization by MG63 cells. Thus, even if working without serum is far away from the physiological conditions, it serves as a tool for investigating the direct interaction of bare NPs with cells. Accordingly, cytotoxicity induced by nanoparticles can be explained by two possible mechanisms. Firstly, NPs can be taken up by cells and this could already cause cell damage by affecting cells functions⁴³. Secondly, in the event NPs could partly dissolve, either in the cell cytosol owing to the lower pH (5-6) or in the cell culture media, the dissolution products would increase the calcium, phosphate and the ion-doped concentrations either inside or surrounding the cells, which may influence the cellular behavior⁴⁴.

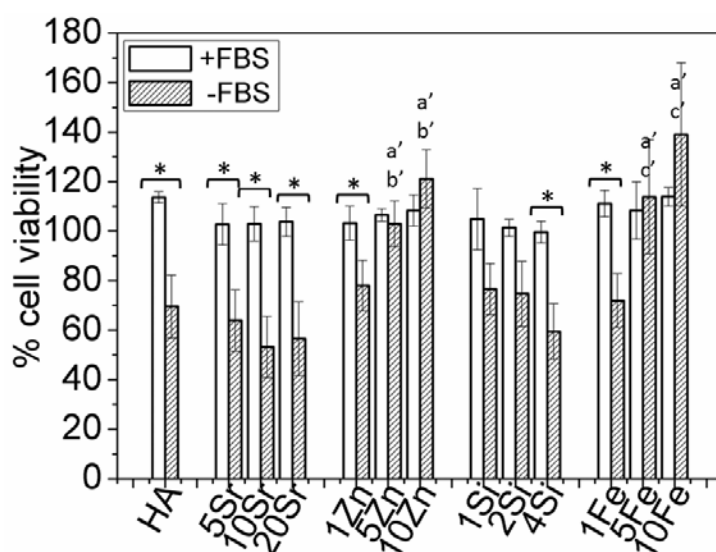


Figure 4.6 Viability of MG63 cells after the treatment with different ion-doped HA NPs at concentration of 100 µg/ml for 24 h. Letters in the graphs indicate significant differences among ion-doped HA NPs cultured without FBS: a -indicates differences with HA NPs, b -differences with 1Zn NPs, c -differences with 1Fe NPs ($P < 0.05$, $N = 6$). (*) indicates significant differences between the same pair of NPs cultured with or without FBS ($P < 0.05$, $N = 6$).

As it was presented in **Chapter 3** (see Table 3.2), under the serum-containing condition all NPs became negatively charged due to the adsorption of proteins.

Taking this into consideration, it is reasonable to think that under this condition the NPs were not cytotoxic because the cellular uptake of NPs was inhibited by the electrostatic repulsion between the negatively charged cell membrane and negatively charged NPs.

When FBS was excluded from cell culture media, the viability of MG63 cells was affected differently depending on the type of ion doping and its concentration. As shown in Figure 4.6, undoped HA nanoparticles showed 70% cell viability which is lower than the cell viability that was obtained when FBS was present. This, as already mentioned, could be due to the fact that nanoparticles are being internalized in cells, because the surface charge (zeta potential) of the NPs after incubation in serum-free conditions is around ± 2 mV and the electrostatic repulsion effect between NPs and cells membrane should be negligible (Table 3.2 in chapter 3). Furthermore, the effects of Si and Sr-doped HA NPs on MG63 cell cytotoxicity seem not to be significantly altered in comparison with the undoped HA NPs although there was a slight decrease in cell viability with ion concentration. Interestingly, Zn and Fe-doped HA NPs clearly stimulated cell proliferation under serum-free condition (Figure 4.6), as the viability of MG63 cells for 10Zn and 10Fe increased to 123% and 135% from $\sim 70\%$, respectively. Coincidentally, it seems that only the NPs having larger specific surface area (as shown in Table 4.2, SSA for 10Zn and 10Fe are 138 and 145m²/g, respectively) can stimulate the proliferation of MG63 cells. However, if the specific surface area would be the reason, one should expect similar cell proliferation ability for 5Zn and 10Zn as both have identical SSA. Since this is not the case, it points to the doping ion as the major role player.

To gain more insights understanding the mechanism/s by which Zn -doped NPs enhanced MG63 proliferation further studies were performed to confirm this effect on MG63 cells (Fe-doped NPs were not further investigated because they had too large dispersion in their values, Figure 4.6). Firstly, the effect of supplying Zn ions on MG63 cells was analyzed. For this purpose cells were cultured in media supplemented with different concentrations of Zn²⁺ (ZnCl₂) corresponding to the amounts of Zn doped in the NPs (up to 8.0 wt%). Figure 4.7 shows that after 1 day

of incubation the addition of $ZnCl_2$ did not cause appreciable changes in cell viability indicating that the eventual release of Zn by dissolution of the NP in serum free conditions was not responsible for the increased proliferation. Thus, internalization again seemed a requirement. In order to further prove that 10Zn NPs had to be internalized by cells to stimulate cell proliferation, 'indirect' cell culture studies were performed. For this purpose, MG63 cells were seeded in normal well plates and NP suspensions in the cell culture medium without FBS were placed in the inserts which have 0.4 μm pores allowing ionic exchanges between the culture medium and the NPs but prevented any direct contact of the NPs with the cells. The results showed that if 10Zn NPs were not in direct contact with the cells viability was preserved; and only when cells became exposed directly to the NPs higher proliferation was induced (Figure 4.7b). This again proved that the ions, even 'if' released in the cell culture medium from 10Zn NPs could not promote MG63 proliferation and, furthermore, it can be concluded that to achieve increased proliferation, 10Zn NPs has to interact directly with cells.

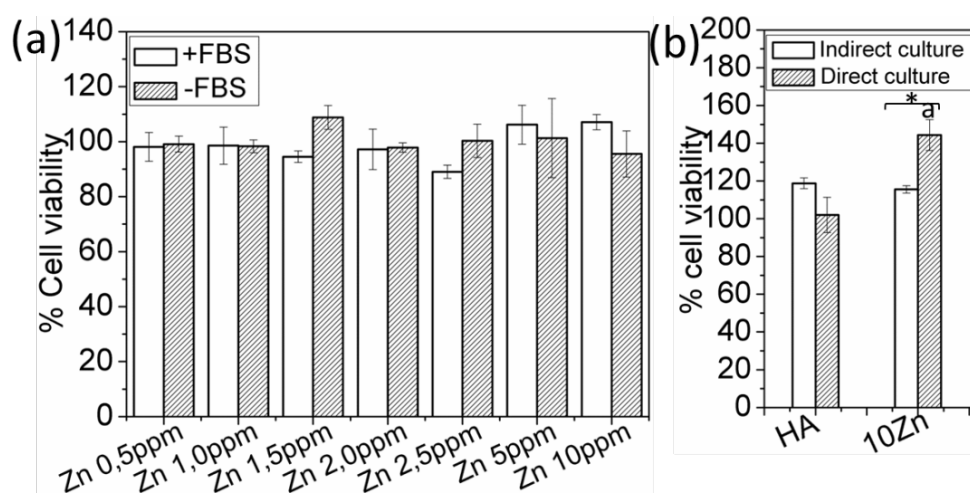


Figure 4.7 (a) Viability of MG63 cells exposed to cell culture media supplemented with various concentrations of $ZnCl_2$ for 24 hours, (b) Viability of cells exposed directly or indirectly to NPs suspensions in the absence of FBS using Transwell system. Letter a in graph (b) indicate significant differences with HA NPs cultured in direct contact of cell-NPs without FBS ($P < 0.05$, $N = 3$). (*) indicates significant differences for the same type of NPs cultured in indirect and direct way ($P < 0.05$, $N = 3$).

To determine the maximum dose of NPs that the cells could uptake without becoming cytotoxic, dose dependent experiments were performed using HA

(control) and 10Zn NPs under the conditions of serum-containing and serum-free conditions using MG63 cells (Figure 4.8). After 24 hours of incubation with the NPs at doses varying from 100 to 1000 $\mu\text{g}/\text{ml}$, it was observed that cell viability was preserved in the presence of serum regardless of the type of NPs and its dose. This still can be interpreted by the electrostatic repulsion effect between the negatively charged NPs upon protein adsorption and the cell membrane. In the absence of serum, 10Zn NPs stimulated cell proliferation at the lower concentrations of 100 and 250 $\mu\text{g}/\text{ml}$ yielding values up to 141% and 152% of cell viability, respectively. However, when the concentration of the NPs increased to 500 $\mu\text{g}/\text{ml}$, the positive effect of NPs on MG63 cells was compromised and viability began to decrease up to a 72% for 1000 $\mu\text{g}/\text{ml}$ of NPs. This behaviour was expected as an increased internalization should eventually become cytotoxic. In the case of the control HA NPs the dose dependent study showed a continuous cytotoxic response with NPs. Only $\sim 30\%$ of viability remained at the highest dose (1000 $\mu\text{g}/\text{mL}$).

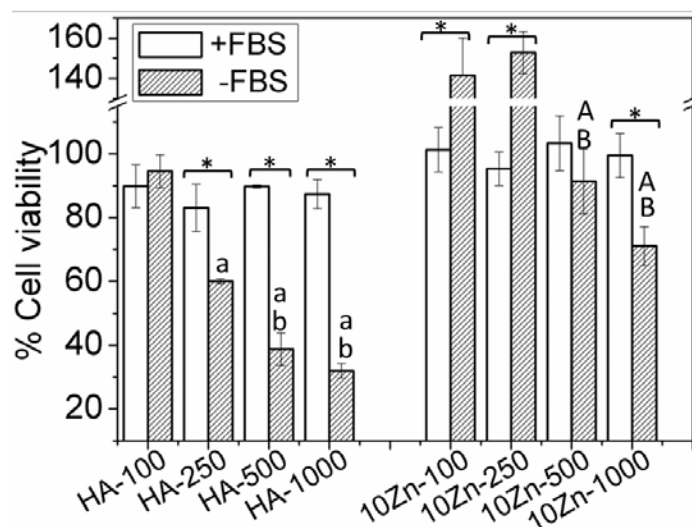


Figure 4.8 Dose dependent cytotoxicity of HA and Zn-doped HA (10Zn) on MG63 cells in the presence or absence of 10 v/v% FBS. The concentrations of NPs are from 100 to 1000 $\mu\text{g}/\text{ml}$ and incubation time is 24 hours. Letters in the graphs indicate significant differences between HA NPs doses cultured without FBS: a-indicates differences with 100 $\mu\text{g}/\text{mL}$, b-differences with 250 $\mu\text{g}/\text{mL}$, c-differences with 500 $\mu\text{g}/\text{mL}$ and, d-differences with 1000 $\mu\text{g}/\text{mL}$. Capital letters indicate significant differences between 10 ZN NPs doses cultured without FBS ($P < 0.05$, $N = 3$): A-indicates differences with 100 $\mu\text{g}/\text{mL}$, B-indicates differences with 250 $\mu\text{g}/\text{mL}$. (*) compares significant differences between the same pair of NPs cultured with or without FBS ($P < 0.05$, $N = 3$).

In addition to the dose-dependent studies, time-dependent cytotoxic studies were also performed to investigate the toxicity of NPs in a time frame longer than 24 h (conventional tests) without changing the cell culture media. The results are shown in Figure 4.9.

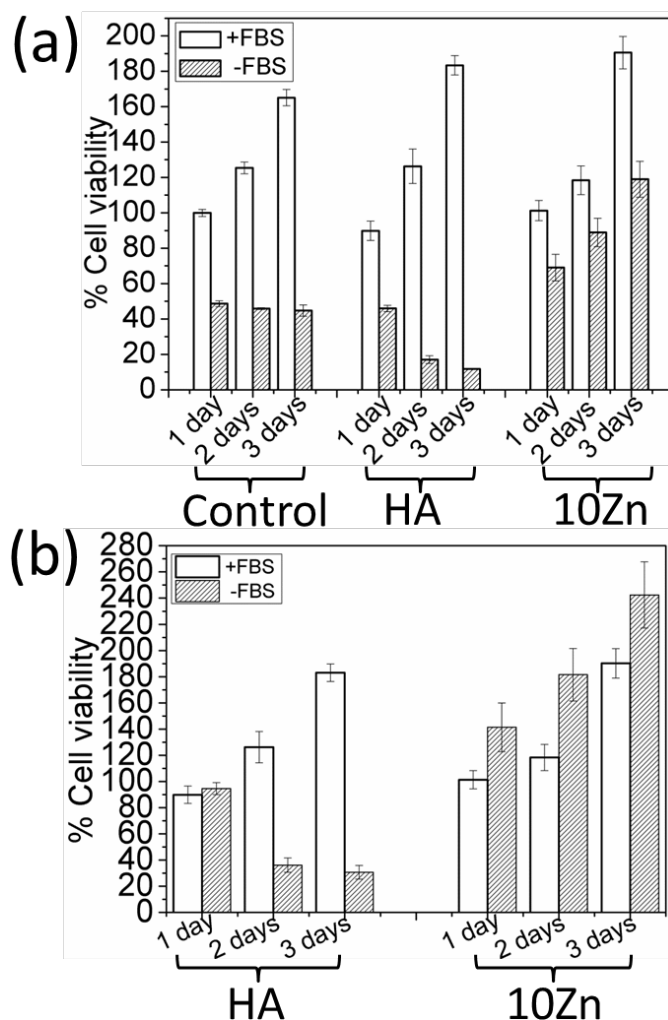


Figure 4.9 Cytotoxicity of HA and Zn-doped HA NPs(10Zn) in the presence or absence of 10 v/v% FBS on MG63 cells after 1, 2 and 3 days incubation time using 100 µg/ml of NPs. (a) Cell viability at each time point was calculated as the percentage of viable cells for every condition divided by the viability of cells cultured at day 1 in the presence of FBS and without NPs. (b) Cell viability at each time point was calculated as the percentage of viable cells for every condition divided by the viability of cells cultured at day 1 in the same conditions as the NPs (i.e. with/without FBS) but without NPs.

In Figure 4.9a, each bar represents the % in proliferation with regards to a control sample which corresponded to cells cultured for 1 day in the presence of FBS. Thus, in this representation the proliferation induced by the presence of NPs is plotted

relative to the proliferation that should exhibit cells in “normal” conditions. As shown in Figure 4.9a, cultured cells under serum-containing conditions proliferated over time and this was mainly attributed to the presence of growth factors in FBS which are required for normal cell growth. However, cells cultured without NPs under serum-free condition neither grow nor died as cell viability was kept at 45% regardless of incubation time. This meant that the absence of FBS kept MG63 cells in un-growing status and the population of viable cells was simply preserved. However, once cells were exposed to the NPs, cell viability varied with the type of NPs and became clearly cytotoxic for HA NPs but induced an increased proliferation with time for Zn-doped NPs. It is interesting to note that, in spite of the proliferative action of Zn NPs, cell population was never as high as for serum-containing condition proving how important is serum for cell growth. In fact, even if the percentage of cell population was not the same as in serum containing conditions it was already a great surprise to see that cells in the presence of Zn NPs keep on growing without FBS.

To better understand what represents the values obtained of cell proliferation for 10Zn NPs, the graph from Figure 4.9b was re-plotted in Figure 4.9a in a different manner. In Figure 4.9b, each bar represented the % in proliferation with regards to a control which corresponded to cells cultured for 1 day in identical conditions as the sample but without NPs. As expected, both, HA and 10Zn NPs did not compromise cell viability over time under serum-containing conditions because the negative charge conferred by the proteins adsorbed on the NPs prevented their internalization. But when FBS was excluded from the cell culture media, the cytotoxicity of HA NPs increased with the incubation time and after 2 and 3 days of incubation MG63 cells showed a significant loss in viability of about 60-70% (Figure 4.9b). However, after 3 days of exposure to 100 $\mu\text{g}/\text{mL}$ the 10Zn NPs led to a significant increase in cell growth as shown by a 240% of cell viability (Figure 4.9b). This confirmed that Zn-doped HA NPs can really make MG63 cells proliferate under the specific condition of serum-free culture media.

One of the major concerns from the experiments shown in Fig. 4.9 was whether the deprivation of growth factors for the three days assay in the serum free condition

could have masked the effect of the NPs as without FBS cells cannot function properly. For this reason an additional cell culture study was designed. The strategy was not to supply 10 v/v% FBS to MG63 cells for the first 6 hours of NPs incubation to allow nanoparticles internalization into the cells (as already discussed FBS absorption on NPs generates a negative charge that inhibits their internalization). After 6 hours incubation, 10 v/v% of FBS was supplemented to the cell culture media to allow cells to grow under the normal cell culture conditions up to 3 days. As shown in Figure 4.10b, cell viability for 10Zn NPs increased to 140% on the 3rd day of cell culture while cell viability of HA NPs remained close to that of the control (cells seeded without NPs).

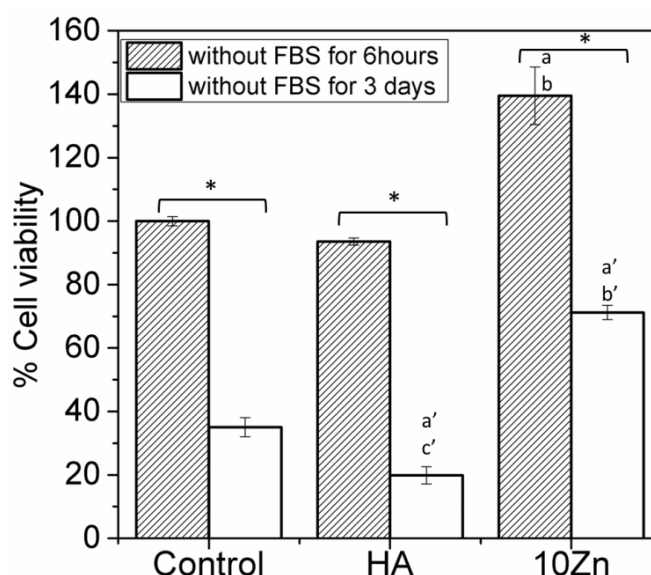


Figure 4.10 Cytotoxicity effect of HA and 10Zn NPs on MG63 cells after 3 days incubation using 100 $\mu\text{g}/\text{mL}$ under the following conditions: without FBS supplement throughout the whole culture period (3 days) and without FBS for the first 6 hours of NPs incubation, afterwards, 10 v/v% FBS was supplemented. As control cells were cultured without NPs in the presence of FBS for the whole 3 days. Cell viability per conditions was calculated as the percentage of viable cells for every condition divided by the viability of cells cultured at day 3 in the presence of FBS and without NPs. Letters in the graphs indicate significant differences between NPs cultured without FBS just for 6hours: a-indicates differences with cells alone, b-differences with HA NPs. Letters with (') in the graphs indicate significant differences between NPs cultured without FBS for 3days: a'-indicates differences with cells alone, b'-differences with HA NPs. (*) compares significant differences between the HA and 10Zn NPs cultured without 10 v/v% FBS for 6 hours and for the whole culture period, respectively ($P < 0.05$, $N = 3$).

Through this experiment it has been proved that working in conditions nearly close to physiological (FBS was only excluded for the six first hours of cell culture yet this was found not to alter cell viability) Zn NPs had a very positive impact in cell proliferation. These results can be very positive when thinking in the development of carriers for gene delivery.

4.4.2.2 *Cytotoxicity of NPs in rMSCs*

Besides the potential that has been observed for Zn-doped NPs, it is well known that cell-NPs interaction is cell dependent. In this regards this section aims at investigating how rat mesenchymal stem cells (rMSCs) respond to the various ion-doped HA NPs under the same cell culture conditions as those used for MG63 cells. Figure 4.11 demonstrates that cell viability was not altered significantly by the ion-doped NPs in the presence of FBS (cell viability was around 100% for all samples) except for Zn-doped HA NPs. As the concentration of Zn increased in NPs, cell viability increased (~150% for 10Zn NPs). When FBS was excluded, all ion-doped NPs seemed to induce slight cytotoxicity on cells with cell viability around 80%, but Zn-doped HA NPs seemed to stimulate the proliferation of rMSCs like it did for MG63 cells.

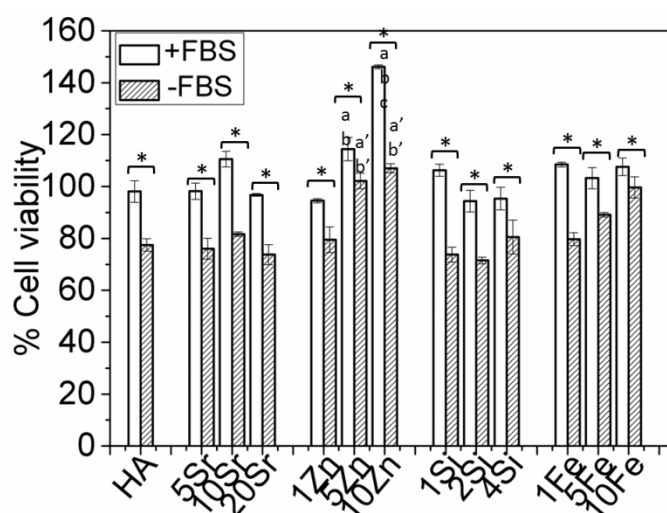


Figure 4.11 Viability of rMSCs after exposure to various ion-doped HA nanoparticles at the concentration of 100 µg/ml for 24 h. Data are presented as the average \pm SD for $n = 3$. Letters in the graphs indicate significant differences among NPs cultured with FBS: a -indicates differences with HA NPs, b -differences with 1Zn NPs, c -differences with 5Zn. Letters with (') in the graphs indicate significant differences between NPs cultured without FBS: a'-indicates differences with HA NPs, b'-differences with 1Zn NPs. (*) indicates significant differences between the same pair of NPs cultured with or without FBS ($P < 0.05$, $N = 3$).

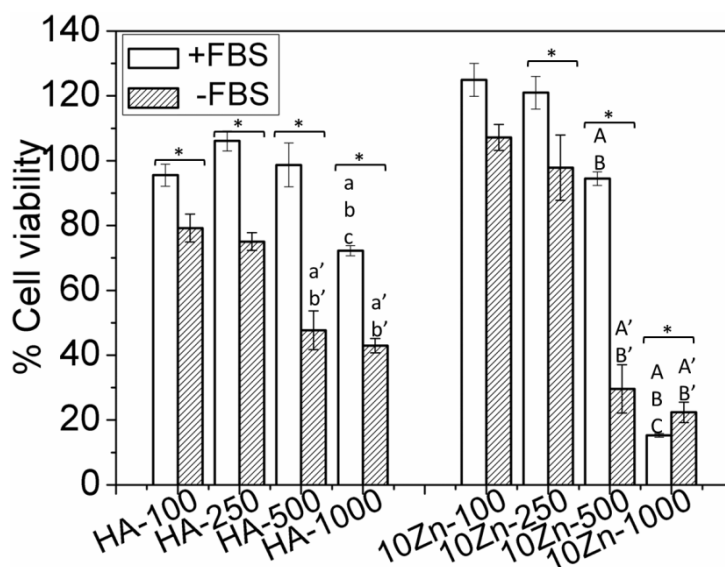


Figure 4.12 Dose dependent cytotoxicity of HA and Zn-doped HA (10Zn) NPs on rMSCs in the presence or absence of 10 v/v% FBS. The concentrations of NPs were from 100 to 1000µg/ml and the incubation time was set to 24 hours. Letters in the graphs indicate significant differences between HA NPs doses cultured with FBS: a- indicates differences with 100 µg/mL, b-differences with 250 µg/mL, c-differences with 500 µg/mL and, d-differences with 1000 µg/mL. Letters with (') in the graphs indicate significant differences between HA NPs doses cultured without FBS: a'- indicates differences with 100 µg/mL, b'-differences with 250 µg/mL, c'-differences with 500 µg/mL and, d'-differences with 1000 µg/mL. Capital letters without or with (') indicate significant differences between 10 Zn NPs doses cultured with or without FBS: A and A'-indicate differences with 100 µg/mL, B and B'-differences with 250 µg/mL, C and C'-differences with 500 µg/mL and, D and D'-differences with 1000 µg/mL ($P < 0.05$, $N = 3$). (*) compares significant differences between the same pair of NPs cultured with or without FBS ($P < 0.05$, $N = 3$).

In an attempt to highlight differences in the cytotoxic behavior of NPs, a dose-dependent experiment was performed in the concentration range from 100 to 1000 µg/ml for the HA and 10 Zn NPs. As it is shown in Figure 4.12, increasing the dose of HA and 10Zn NPs caused a decrease in cell viability, which could be taken as an indicator of a higher degree of internalization. Interestingly, this assay also revealed that for low NP doses (<250 µg/ml) and regardless of the presence of FBS, Zn-doped NPs increased (+FBS) or at least maintained (-FBS) the viability of cells as compared to HA NPs. Although further studies are ongoing to unveil the positive effects of Zn-doped NPs for this cell type, these are already out of the scope of the present thesis.

Overall the cytotoxicity results for rMSCs differ from those obtained for MG63 cells in which, viability was preserved under serum-containing conditions even at the highest NP dose (Figure 4.8). Remarkably, the negative charge conferred by FBS adsorption on the NPs did not seem to prevent rMSCs from internalizing NPs unlike for MG63 cells. This might be due to the different cellular metabolism and behaviour between these two different kinds of cells⁴⁵. In fact, already in the previous chapter it was put forward the particular selectivity of MG63 cells for NPs surface charge.

Although exploring the biological mechanisms that lead to cell proliferation for Zn-doped NPs is out of the scope of the present work, it is worth presenting the roles of Zn ions in cell metabolism to better understand how these NPs may operate. Zinc is involved in many biological activities including cell growth and DNA synthesis and it has been reported that zinc ions promoted the proliferation of several types of cells *in vitro*^{7,8,46,47}. In these works, the proliferative action of Zn ions in cells was assessed using Zn salts as supplement in the culture medium. In the present work, ZnCl₂ was also supplied into the culture medium for 24 hours as a control (Figure 4.7a). However, MG63 cell growth was only stimulated by the Zn-doped NPs and not when supplying Zn ions in the culture medium. This indicates that the proliferative effect reported in the literature when using Zn salts was either cell-dependent (cells used in the reported works: myogenic cells and neuronal, etc), or it could be due to the need of longer incubation times (up to 2 days were assayed for the mentioned works).

In the present study, Zn-doped NPs were confirmed to stimulate the proliferation of MG63 cells (and possibly also for rMSCs) in a time as short as 24 hours. It is assumed that once NPs are internalized, they dissolve in the cytosol owing to the low pH releasing Zn which can then stimulate cell proliferation. Although the mechanism is not well understood, it is important to point out that the pathways by which ions and NPs enter the cell are different (ions can permeate through cell membrane while NPs enter via endocytosis) which can explain the difference in the present work. Additionally, several studies have indicated that cellular uptake

of NPs is of crucial importance in governing a range of cellular behaviors including cell growth, apoptosis and adhesion^{43,48-50}. In the present study, through indirect cell culture study it has been indirectly proved that, to stimulate MG63 cells growth, Zn-doped HA nanoparticles have to be internalized by cells.

Overall this work proves that Zn ion doping in HA NPs could be used as a tool to stimulate cell growth. The most critical aspect is, however, to have the right surface charge to enable NPs internalization. Although the further studies with other cell types are required, it is expected that this positive effect of using Zn-doped HA NPs on cells could be applied in bone regeneration applications by stimulating cell growth during bone formation and also in gene delivery applications as potential carriers which could aid in the replication of DNA.

4.5 Conclusions

In the present chapter it has been proved that it is possible to synthesize phase pure Zn, Sr, Si and Fe-doped hydroxyapatite nanoparticles. Detailed investigation on the composition and the physicochemical properties of the NPs, pointed that Zn and Fe ions were adsorbed on the surface of the NPs while Sr and Si became incorporated in the crystal structure. All NPs shared the same morphology (needle-like) but varied in specific surface area and solubility

Cell culture studies for all ion-doped NPs revealed that they were non-cytotoxic to MG63 and rMSCs cells provided FBS was present in the cell culture media. It was believed that proteins from serum adsorbed on the NPs preventing their internalization (and cytotoxicity). Cell culture studies in the absence of FBS proved that Zn and Fe-doped HA nanoparticles could stimulate MG63 cells proliferation upon internalization. It was believed that the doping ion was responsible for this effect rather than the specific physicochemical characteristics of the NPs. Thus, the present findings provide useful information for the development of new strategies for the design of efficient gene/drug delivery HA nano-carriers. In addition, these results also showed that HA NPs should no longer be viewed as simple carriers for

biomedical applications, as they can also play an active role in mediating biological effects through changing their chemical composition by simply doping foreign ions.

4.6 References

1. Pors Nielsen, S. The biological role of strontium. *Bone* **35**, 583–8 (2004).
2. Reginster, J. Y. *et al.* Long-term treatment of postmenopausal osteoporosis with strontium ranelate: results at 8 years. *Bone* **45**, 1059–64 (2009).
3. Boanini, E., Torricelli, P., Fini, M. & Bigi, a. Osteopenic bone cell response to strontium-substituted hydroxyapatite. *J. Mater. Sci. Mater. Med.* **22**, 2079–88 (2011).
4. Thian, E. S. *et al.* Zinc-substituted hydroxyapatite: a biomaterial with enhanced bioactivity and antibacterial properties. *J. Mater. Sci. Mater. Med.* **24**, 437–45 (2013).
5. Shepherd, D. V, Kauppinen, K., Brooks, R. a & Best, S. M. An in vitro study into the effect of zinc substitutedhydroxyapatite on osteoclast number and activity. *J. Biomed. Mater. Res. A* **102**, 4136–4141 (2014).
6. Macdonald, R. S. The Role of Zinc in Growth and Cell Proliferation. *J. Nutr.* **130**, 1500–1508 (2000).
7. Ohashi, K. *et al.* Zinc promotes proliferation and activation of myogenic cells via the PI3K/Akt and ERK signaling cascade. *Exp. Cell Res.* **333**, 228–237 (2015).
8. Seth, R. *et al.* Zinc deficiency induces apoptosis via mitochondrial p53- and caspase-dependent pathways in human neuronal precursor cells. *J. trace Elem. Med. Biol.* **30**, 59–65 (2015).
9. Carlisle, E. M. Silicon: a possible factor in bone calcification. *Science (80-.).* **167**, 279–80 (1970).

10. Johnson-Wimbley, T. D. & Graham, D. Y. Diagnosis and management of iron deficiency anemia in the 21st century. *Therap. Adv. Gastroenterol.* **4**, 177–84 (2011).
11. Li, Y., Nam, C. T. & Ooi, C. P. Iron(III) and manganese(II) substituted hydroxyapatite nanoparticles: Characterization and cytotoxicity analysis. *J. Phys. Conf. Ser.* **187**, 012024 (2009).
12. Mohamed, K., Ereiba, T., Mostafa, A. G., Gamal, G. A. & Said, A. H. In vitro study of iron doped hydroxyapatite. *J. Biophys. Chem.* **4**, 122–130 (2013).
13. Turney, T. W. *et al.* Formation of Zinc-Containing Nanoparticles from Zn²⁺ Ions in Cell Culture Media: Implications for the Nanotoxicology of ZnO. (2012).
14. Balas, F., Pérez-Pariente, J. & Vallet-Regí, M. In vitro bioactivity of silicon-substituted hydroxyapatites. *J. Biomed. Mater. Res. A* **66**, 364–75 (2003).
15. Chandra, V. S. *et al.* Blood compatibility of iron-doped nanosize hydroxyapatite and its drug release. *ACS Appl. Mater. Interfaces* **4**, 1200–10 (2012).
16. Aina, V. *et al.* Sr-containing hydroxyapatite: morphologies of HA crystals and bioactivity on osteoblast cells. *Mater. Sci. Eng. C. Mater. Biol. Appl.* **33**, 1132–42 (2013).
17. Cox, S. C., Jamshidi, P., Grover, L. M. & Mallick, K. K. Preparation and characterisation of nanophase Sr, Mg, and Zn substituted hydroxyapatite by aqueous precipitation. *Mater. Sci. Eng. C* **35**, 106–114 (2014).
18. Shepherd, J. H., Shepherd, D. V & Best, S. M. Substituted hydroxyapatites for bone repair. *J. Mater. Sci. Mater. Med.* **23**, 2335–47 (2012).
19. Boanini, E., Gazzano, M. & Bigi, a. Ionic substitutions in calcium phosphates synthesized at low temperature. *Acta Biomater.* **6**, 1882–94 (2010).

20. Capuccini, C. *et al.* Interaction of Sr-doped hydroxyapatite nanocrystals with osteoclast and osteoblast-like cells. *J. Biomed. Mater. Res. A* **89**, 594–600 (2009).
21. Botelho, C. M. *et al.* Human osteoblast response to silicon-substituted hydroxyapatite. *J. Biomed Mater Res A* **79**, 723–730 (2006).
22. Patel, N. *et al.* A comparative study on the in vivo behavior of hydroxyapatite and silicon substituted hydroxyapatite granules. *J. Mater. Sci. Mater. Med.* **13**, 1199–1206 (2002).
23. Gutowska, I., Machoy, Z. & Machaliński, B. The role of bivalent metals in hydroxyapatite structures as revealed by molecular modeling with the HyperChem software. *J. Biomed. Mater. Res. A* **75**, 788–93 (2005).
24. Aina, V. *et al.* Magnesium- and strontium-co-substituted hydroxyapatite: the effects of doped-ions on the structure and chemico-physical properties. *J. Mater. Sci. Mater. Med.* **23**, 2867–2879 (2012).
25. Li, Z. Y. *et al.* Chemical composition, crystal size and lattice structural changes after incorporation of strontium into biomimetic apatite. *Biomaterials* **28**, 1452–1460 (2007).
26. Kim, S. R. *et al.* Synthesis of Si, Mg substituted hydroxyapatites and their sintering behaviors. *Biomaterials* **24**, 1389–98 (2003).
27. Padmanabhan, S. K., Ul Haq, E. & Licciulli, A. Rapid synthesis and characterization of silicon substituted nano hydroxyapatite using microwave irradiation. *Curr. Appl. Phys.* **14**, 87–92 (2014).
28. Hu, W., Ma, J., Wang, J. & Zhang, S. Fine structure study on low concentration zinc substituted hydroxyapatite nanoparticles. *Mater. Sci. Eng. C* **32**, 2404–2410 (2012).
29. Tampieri, A. *et al.* Intrinsic magnetism and hyperthermia in bioactive Fe-doped hydroxyapatite. *Acta Biomater.* **8**, 843–51 (2012).

30. Koutsopoulos, S. Synthesis and characterization of hydroxyapatite crystals : A review study on the analytical methods. *J Biomed Mater Res* **62**, 31–34 (2002).
31. Leventouri, T. Neutron powder diffraction studies of silicon-substituted hydroxyapatite. *Biomaterials* **24**, 4205–4211 (2003).
32. Sadat-Shojai, M., Khorasani, M.-T., Dinpanah-Khoshdargi, E. & Jamshidi, A. Synthesis methods for nanosized hydroxyapatite with diverse structures. *Acta Biomater.* **9**, 7591–621 (2013).
33. Ichiro Sunagawa. Growth and Morphology of Crystals. *Forma* **14**, 147–166 (1999).
34. Müller, K. H. *et al.* The effect of particle agglomeration on the formation of a surface-connected compartment induced by hydroxyapatite nanoparticles in human monocyte-derived macrophages. *Biomaterials* **35**, 1074–88 (2014).
35. Gasquères, G. *et al.* Revisiting silicate substituted hydroxyapatite by solid-state NMR. *Magn. Reson. Chem.* **46**, 342–6 (2008).
36. Gibson, I. R., Best, S. M. & Bonfield, W. Chemical characterization of silicon-substituted hydroxyapatite. *J. Biomed. Mater. Res.* **44**, 422–428 (1999).
37. Prakash, K. H., Kumar, R., Ooi, C. P., Cheang, P. & Khor, K. a. Apparent solubility of hydroxyapatite in aqueous medium and its influence on the morphology of nanocrystallites with precipitation temperature. *Langmuir* **22**, 11002–8 (2006).
38. Sprio, S. *et al.* Physico-chemical properties and solubility behaviour of multi-substituted hydroxyapatite powders containing silicon. *Mater. Sci. Eng. C* **28**, 179–187 (2008).
39. Pan, H. B. *et al.* Solubility of strontium-substituted apatite by solid titration. *Acta Biomater.* **5**, 1678–85 (2009).

40. Okazaki, M., Takahashi, J. & Kimura, H. Crystallinity and solubility behavior of iron-containing fluoridated hydroxyapatites. *J. Biomed. Mater. Res.* **20**, 879–86 (1986).
41. Hirsch, V., Salaklang, J., Rothen-Rutishauser, B. & Petri-Fink, A. Influence of serum supplemented cell culture medium on colloidal stability of polymer coated iron oxide and polystyrene nanoparticles with impact on cell interactions in vitro. *IEEE Trans. Magn.* **49**, 402–407 (2013).
42. Hails, L. a *et al.* Inhibition of hydroxyapatite nanoparticle-induced osteogenic activity in skeletal cells by adsorption of serum proteins. *Small* **6**, 1986–91 (2010).
43. Huang, X., Teng, X., Chen, D., Tang, F. & He, J. The effect of the shape of mesoporous silica nanoparticles on cellular uptake and cell function. *Biomaterials* **31**, 438–448 (2010).
44. Chen, L., Mccrate, J. M., Lee, J. C.-M. & Li, H. The role of surface charge on the uptake and biocompatibility of hydroxyapatite nanoparticles with osteoblast cells. *Nanotechnology* **22**, 105708 (2011).
45. Qing, F. *et al.* Selective effects of hydroxyapatite nanoparticles on osteosarcoma cells and osteoblasts. *J. Mater. Sci. Mater. Med.* **23**, 2245–51 (2012).
46. McClung, J. P., Tarr, T. N., Barnes, B. R., Scrimgeour, A. G. & Young, A. J. Effect of supplemental dietary zinc on the mammalian target of rapamycin (mTOR) signaling pathway in skeletal muscle and liver from post-absorptive mice. *Biol. Trace Elem. Res.* **118**, 65–76 (2007).
47. Adamo, A. M. *et al.* The role of zinc in the modulation of neuronal proliferation and apoptosis. *Neurotox. Res.* **17**, 1–14 (2010).
48. Albanese, A. & Chan, W. C. W. Effect of gold nanoparticle aggregation on cell uptake and toxicity. *ACS Nano* **5**, 5478–5489 (2011).

49. Duan, X. & Li, Y. Physicochemical characteristics of nanoparticles affect circulation, biodistribution, cellular internalization, and trafficking. *Small* **9**, 1521–32 (2013).
50. Bauer, I. W., Li, S.-P., Han, Y.-C., Yuan, L. & Yin, M.-Z. Internalization of hydroxyapatite nanoparticles in liver cancer cells. *J. Mater. Sci. Mater. Med.* **19**, 1091–5 (2008).

Chapter 5

Co-/effect of Organic Molecules and Ions in Calcium Phosphate Precipitation

In **Chapters 3** and **4**, the interaction of ion doped hydroxyapatite (HA) nanoparticles (NPs) with cells was investigated. *In vitro* results demonstrated that cell behavior had been affected differently with the various types of NPs and it turned out that HA NPs should no longer be viewed as simple carriers for gene/drug delivery, but can also be considered a potential tool to mediate biological effects *via* doping ions. Essentially, biological apatite in bone tissue consists of ion-doped HA NPs which are formed with the help of organic molecules (e.g. proteins) in vertebrates. The process of formation of mineral phases in living organisms is named biomineralization. During biomineralization, living systems make use of organic molecules to elaborate complex biominerals with optimized properties for specific purposes. These strategies involved in biomineralization have enlightened researchers and a good wealth of studies has been focused on the regulation of calcium phosphate (CaP) precipitation using organic molecules. This has allowed not only to fabricate new functional materials but also to further understand the mechanisms of biomineralization. In this present chapter, the interests of investigation were therefore shifted to CaP precipitation in the presence of organic molecules.

5.1 Introduction

Biominerals created by living organisms always have unique morphologies which can only be understood from the interplay of inorganic building blocks with organic matter. The organic molecules modulate the precipitation and orchestrate

the assembly of the inorganic building blocks giving rise to biominerals with complex shapes, and such processes often occur at nearly ambient conditions^{1,2}. Thus, the strategy of developing complex materials at nearly ambient conditions with the help of specific organic molecules is becoming a very promising route not only in the understanding of biomineralization processes, i.e. mineral formation by living systems, but also in the design of new functional materials^{3,4}.

One system of particular interest is the calcium phosphate (CaP) system that governs the mineral formation of bone and teeth in vertebrates. In spite of the numerous studies existing in this field, there are fundamental aspects that still remain unclear. In particular, one key aspect still under debate is whether calcium phosphate bio-mineralization occurs *via* precursor phases such as amorphous calcium phosphate. The difficulty of detecting this phase at the early stages of mineralization is a real challenge and though some studies point to the presence of this phase^{5,6} still today there is no irrefutable proof of its presence.^{7,8} Although dealing with amorphous phases is a complex task owing to the unstable nature and continuous transformation that such phases undergo, they provide the most remarkable morphologies found in nature. Amorphous phases, being isotropic have no preferred form and can be easily moulded/assembled into any shape with the participation of organic structure directing molecules^{2,9}.

Several kinds of organic additives¹⁰⁻¹⁵ have been used for the control of nucleation and crystal growth of inorganic materials but among them double hydrophilic block copolymers (DHBCs) have been found most effective in the crystallization of various materials¹⁵⁻¹⁸. Particularly, Antonietti *et al.*¹⁹ reported in 1998 the stabilization of delicate neuron-like calcium phosphate structures with the help of a DHBC consisting of a long poly (ethylene oxide) block and a short poly (methacrylic acid) block partially alkylated with dodecylamine (PEO-block-PMMA-C₁₂). Afterwards, this neuron-like structure was reported several times again under various preparation conditions showing that they are indeed real features. For instance, in 2005 these structures were replicated by Tjandra *et al.* using a similar design of DHBC (PEO-block-PMMA) but with a longer PMMA chain. The need of the complex DHBC seemed mandatory for the formation of such structures,

and the mechanism of formation was believed to occur via formation of micelle aggregates of the copolymer²⁰. This conclusion was taken from the observation that the core of the neuron-like structures was of the same size than the primary polymer micelle aggregates. In the work of Antonietti, micelles could be readily created by the presence of the hydrophobic C₁₂ chain, and in the work of Tjandra *et al.* micelle formation was believed to take place by neutralization of the carboxyl groups in the longer PMMA chain by calcium ions, rendering the PMMA-Ca chain hydrophobic. Surprisingly, in 2001 a work by Peytcheva *et al.*²¹ showed that polyaspartate was also capable of creating similar structures under specific synthesis conditions but no details were given with regards to the need of forming aggregates. Although neuron-like structures have been fabricated using DHBCs and polyaspartate, the characterization of these structures remain complex owing to their nanostructured nature and their inherent instability.

Besides organic molecules, inorganic ions (e.g. Mg²⁺ and Sr²⁺) are also involved in biomineralization processes and play very important roles. For example, Mg ion is believed to be one of the most important cations which are highly relevant to biological apatite and has its own significance in bone formation²²⁻²⁴. The influence of Mg²⁺ on CaP mineralization has been investigated extensively *in vitro* indicating that the presence of Mg ions prolonged the transformation of amorphous calcium phosphate (ACP) phase to crystalline material^{25,26}. Additionally, Sr ions were also observed to behave the same way as that of Mg ions on the transformation of ACP into HA²⁷. In spite of the relevance of inorganic ions, investigation on the co-effect of organic molecules and inorganic doping ions on the precipitation of calcium phosphates is complex and there are very limited studies on this topic²⁸.

5.2 Objectives

The objectives of the present chapter are twofold:

- To investigate the effect of various organic molecules such as surfactants, anionic and cationic polymers on calcium phosphate precipitation and to perform in-depth characterization of the as-formed hybrid materials using several analytical techniques based on transmission electron microscopy

(TEM) studies such as energy filtered transmission electron microscopy (EFTEM) and energy electron energy loss spectroscopy (EELS).

- To perform CaP mineralization experiments in the presence of ions (Mg^{2+} and Sr^{2+} *etc.*) together with organic molecules and investigate how foreign ions affect the calcium phosphate precipitation process.

5.3 Materials and methods

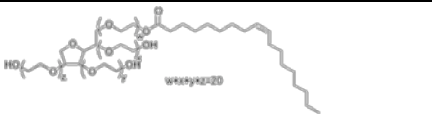
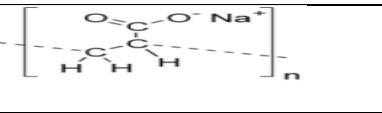
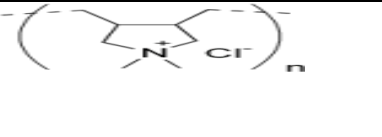
5.3.1 Setting up working system

The working system used to study the effect of organic molecules and ions on the nucleation and crystallization of CaP was set up in terms of type of reactants, concentration, temperature and pH. Synthesis of CaP was carried out by mixing calcium chloride (CaCl_2 , 98% purchased from Panreac) and disodium hydrogen phosphate (Na_2HPO_4 , 98% Panreac) rapidly. Before mixing both solutions, the pH of salts was adjusted to the values required. The concentration of Ca^{2+} and PO_4^{3-} varied from 5 to 100Mm. In order to determine the induction time at which amorphous calcium phosphate transforms into crystalline phases, the pH value and/or conductivity was monitored with a pH electrode and a conductivity electrode (Crison 5014 and MM41, respectively) during the crystallization experiments. All reactions were carried out in polypropylene tubes at a constant temperature of 25°C and under magnetic stirring. The temperature was controlled by means of thermo jacketed vessels coupled to a thermostatic bath (Huber CC2).

5.3.2 CaP precipitation in presence of organic molecules

Surfactant Polysorbate (Tween 80, TW), sodium polyacrylate (PA) with a molecular weight of 1200 g/mol and polydiallyldimethylammonium chloride (PDMAC) of 100000-200000 g/mol were purchased from Sigma Aldrich and introduced to regulate calcium phosphate mineralization. All organic molecules with their chemical formula are summarized in Table 5.1.

Table 5.1 List of organic molecules along with their chemical formula.

Tween 80 (TW) Polysorbate 80	
Sodium polyacrylate (PA)	
Polydiallyldimethyl- ammonium chloride (PDMAC)	

5.3.2.1 Surfactant: Tween 80

The effect of Tween 80 was first investigated by adding different amounts of surfactant into the calcium chloride solution (mixing 20 min) prior to addition of the phosphate salt into the mixture (phosphate solution was added at once). The concentrations of TW explored ranged from 0.01-3.3 wt/v % in the final mixture. Stock solutions of 10 mM CaCl₂ and Na₂HPO₄ (pH 7.2-7.4) were used in experiments. Equal volumes (15mL) of both salts were mixed to make reactions with calcium to phosphorous (Ca/P) molar ratio of 1. This ratio was chosen to allow comparison of the present results with those available from literature¹⁰.

5.3.2.2 Anionic polymer: sodium polyacrylate

Synthesis of CaP in the presence of sodium polyacrylate (PA) were carried out in a similar manner as those reported with the addition of TW. The CaCl₂ solution was mixed with PA molecules (mixing 20 min) prior to addition of the phosphate solution. Various additional synthesis conditions were investigated: 1) two different calcium to phosphorous ratios were explored Ca/P= 1 and 1.67, 2) for the Ca/P= 1.67, different synthesis reactions were performed with increasing amounts of calcium concentrations with final molarity of ~5, 15 and 50 Mm in total 30 mL CaP solution, 3) two different concentrations of PA were explored to make a Ca/PA molar ratio of ~20 and 80 and 4) the effect of pH during the synthesis reaction was investigated by pre-adjusting the pH value of the calcium and phosphate salts as well as that of the PA solution to the pH of interest: pH 3, 7 or 10. Stock solutions of 100 mM CaCl₂, 100 mM/60 mM Na₂HPO₄ and 1 wt% PA (~10 mM) were prepared and the required volumes taken from the diluted solution of the stocks were mixed to carry out all the above mentioned synthesis reactions.

5.3.2.3 Cationic polymer: Polydiallyldimethylammonium chloride

Synthesis with polydiallyldimethylammonium chloride (PDMAC) was carried out by mixing the phosphate solution with the cationic polymer first, prior to addition of the calcium chloride solutions. For this purpose equal volumes of 60 mM Na₂HPO₄ salt of pH 7.4 and 100 mM CaCl₂ solution were used (Ca/P= 1.67) and two different PDMAC concentrations, to make a final concentration of 0.1 and 0.001 wt%, were investigated.

5.3.3 CaP precipitation in presence of organic molecules with foreign ions

To investigate the co-effect of foreign ions with organic molecules on the precipitation of calcium phosphate, synthesis reactions were carried out in a similar manner as those reported with the addition of organic molecules. The ions that were employed were Mg^{2+} ($MgCl_2 \cdot 6H_2O$, 98% Pnerac) and Sr^{2+} ($SrCl_2 \cdot 6H_2O$, 99% Sigma). Briefly, the salt containing the ion of interest was added to the calcium solution with the organic molecule (i.e. Tween or PA) and were mixed for 20 min prior to the addition of phosphate solution. The molar ratio of the foreign ion to that of Ca^{2+} varied from 0.1 to 1. Stock solutions of 10/100 mM $CaCl_2$, 10/60 mM Na_2HPO_4 , and 1 wt% PA (~10 mM), 10 wt% Tween, and 100mM/10mM $SrCl_2$ and $MgCl_2$ were prepared and the required volumes were mixed to carry out all the above mentioned synthesis reactions.

5.3.4 Characterization of biominerals

Characterization comprised transmission electron microscopic (TEM) observation and EDX analyses (Jeol JEM 2100, Jeol JEM 1010 and Hitachi 800MT) as well as field emission scanning electron microscopy observation (FIB/SEM Zeiss Neon 40). TEM samples were prepared by soaking a 300 mesh carbon coated copper grid in the solution of interest, blotted to remove the excess liquid and air dried. SEM examination was performed directly from the TEM grids without any kind of coating.

Additional TEM characterization consisting of annular dark field scanning transmission electron microscopy (ADF-STEM), energy filter transmission electron microscopy (EFTEM) and electron energy loss spectroscopy (EELS) were carried out on a dedicated Zeiss SESAM microscope (Zeiss, Oberkochen) in Max Plank Institute-Stuttgart (Enabling Science and Technology through European Electron Microscopy-ESTEEM Grant).

In TEM, the high-energy electron beam is transmitted through the thinned area of interest of the sample. As the electron beam is transmitted through the thin section,

a variety of beam-specimen interactions occur that yield transmitted electrons, elastically and inelastically scattered (energy-loss) electrons, secondary electrons, back-scattered electrons, and x-ray photons. In TEM-EELS, inelastically scattered (energy-loss) electrons are employed. The amount of energy lost depends on various inelastic scattering processes that occur within the sample and can be measured *via* an electron spectrometer. Among those inelastic scattering processes, the inner shell ionization process by which the electrons from the incident beam interact with the inner-shell electrons of atoms (e.g. K and L) within sample and lose energy, plays a very important role in detecting the elemental components of samples. It is because these energy-loss electrons appear as a step or an edge in EEL spectrum that are referred as to ionization edges and reflect the atomic structure of the element²⁹⁻³¹. In EFTEM, the parallel beam imaging mode in a TEM is coupled with principles of EELS to yield a filtered image. By placing an adjustable slit to allow only the energy-loss electrons contributing to ionization edges of elements through, EFTEM enables the rapid acquisition of elemental maps in TEM thin sections³².

Zeiss SESAM microscope was a 200 kV FEG TEM/STEM microscope equipped with an electrostatic Ω -type monochromator and a MANDOLINE filter to perform EELS measurements at high energy resolution. For EELS, stacks of 100 spectra for each element (Ca, P and O) were acquired within 0.5-3sec/spectra with an energy resolution of 0.3 eV. A series of EFTEM images was recorded at various energy losses with an energy-loss increment of 1.2 eV and an energy-selecting slit of 1.36 for different elements (Ca, P and O). TEM Samples were prepared following the same protocol which was discussed above.

5.4 Results and discussion

5.4.1 The calcium phosphate precipitation system

One first aspect that has to be considered when studying nucleation and mineralization events is the design of the system, i.e. the reaction conditions. Although the term biomineralization already narrows down experiments to those taking place in aqueous environments under mild temperatures and pH, the reactant concentration was carefully chosen in the present work so as to enable visualization of the amorphous to crystalline transition on an adequate time frame. Figure 5.1 displays the typical pH and conductivity profiles over time obtained when mixing equal volumes of a 10 mM calcium salt solution with a 10 mM phosphate salt solution previously adjusted to physiological pH.

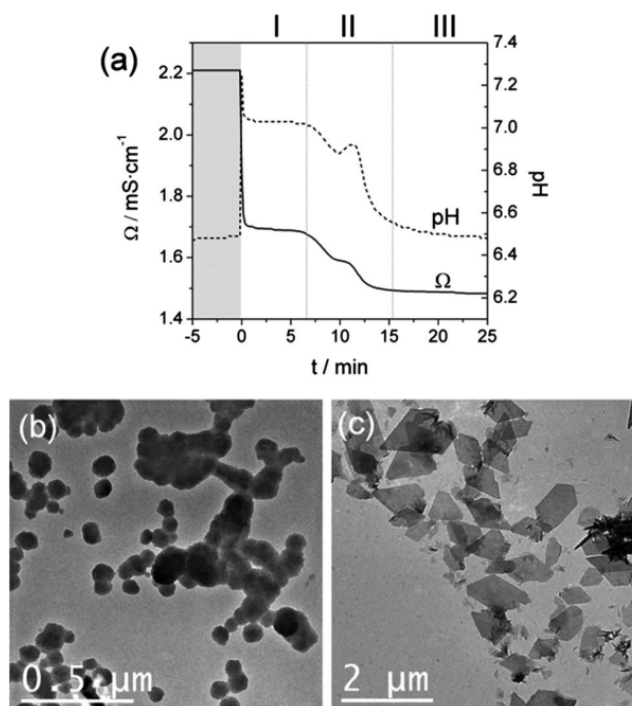


Figure 5.1 (a) pH and conductivity profile of a typical synthesis reaction. Before time zero corresponds to the monitoring of a 15 ml 10 mM calcium chloride solution. At time zero an equal volume of a 10 mM phosphate solution (pH 7.4) is added at once. **(b)** TEM image of the precipitates obtained within the amorphous regime in region I, i.e. 5min after phosphate addition. **(c)** TEM image of the crystallized product from region III.

Time zero corresponds to the time point at which the phosphate salt solution was added into the calcium solution. Both, the pH and conductivity profiles are alike

and, in agreement with other reported works, they can be described by three distinct regions.¹⁰ The first region (I), immediately after mixture of both salts, consists of a plateau and corresponds to the region where amorphous calcium phosphate (ACP) exists, this is followed by a steep decrease in pH/conductivity (region II) which depicts the transformation of the amorphous to the crystalline phase. This transition involves the temporary stabilization of another amorphous phase as observed from the hump in the pH and conductivity profile. The third region (III) is a plateau and corresponds to the final reaction stage, the crystallized product. Such phase transitions events are typical of kinetically driven crystallization processes and involve the continuous precipitation of phases of increasing stability. The macroscopic observation of the reaction starts with an almost transparent solution in region I that becomes turbid at region III corresponding to the bulk precipitation of calcium phosphate (CaP) crystals. Transmission electron microscopy (TEM) grids prepared from region I and III confirmed the presence of ACP and CaP crystals respectively (Figure 5.1).

5.4.2 Effect of organic molecules on CaP precipitation

5.4.2.1 Surfactant Tween 80

The addition of different amounts of non-ionic surfactant Tween 80 (polysorbate 80, TW) into the calcium solution before mixing the phosphate salt was revealed to prolong the transformation of ACP into the crystalline phase and this delay was found to be more pronounced with a lower TW content (Figure 5.2a) by monitoring the conductivities of reactions.

Such observations have also been reported using different molecules and the delay has been explained by the interaction of the organic molecules with the nascent nuclei^{10,11}. Although the impact of TW molecules on the conductivity profile was not pronounced, TEM investigation of the microstructures formed within the amorphous region were remarkable. For TW content below 0.1 wt %, neuron-like structures with a Ca/P ratio of ~ 1 as revealed by EDX analyses were created in addition to the typical globular amorphous structures. SAED in particular showed that both the core and filaments of the structures were amorphous as no lattice fringes could be detected (Figure 5.2c). Increasing the amount of TW above 0.1 wt %

caused the stabilization, within the amorphous region, of tiny rounded precipitates ($< 5\text{ nm}$, Figure 5.2d) which were assumed to be the initial amorphous calcium phosphate before they began aggregating to form larger particles. Thus, taking all these results altogether we can distinguish two different mechanisms of TW interaction: a) for a low amount of TW the surfactant acts as a structure directing agent leading to formation of calcium phosphate neuron-like structures, but b) an increase in the TW content quenches the surface of the initial amorphous nuclei delaying their subsequent growth/assembly.

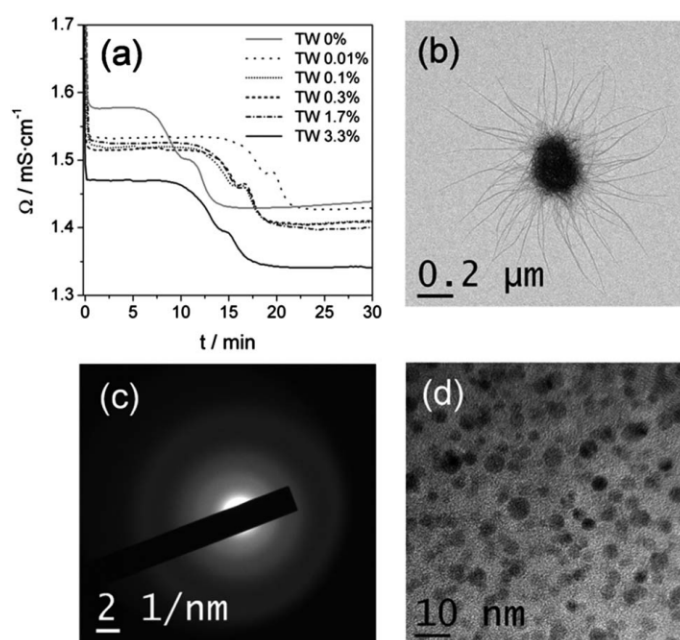


Figure 5.2 (a) Effect of the addition of various contents of Tween 80 (TW) in the conductivity profile. TW was first allowed to mix with the calcium chloride solution before the phosphate solution was added at time zero. The concentrations of the salts were identical as in Fig.1. (b) TEM image obtained for a TW content of 0.1 wt% after 5 min of addition of the phosphate salt. (c) Selected area electron diffraction (SAED) of the neuron-like structure revealing diffuse rings which accounts for the amorphous nature of these structures. (d) TEM image obtained for a TW content of 1.7 wt% after 5 min of addition of the phosphate salt.

Although the formation of these neuron-like structures bears some resemblance to the structures isolated during transformation of ACP to hydroxyapatite (HA) in purely inorganic systems, it is worth stressing that different mechanisms are likely to operate. In the crystallization process of HA, ACP serves as a seed in the nucleation of the crystalline phase. Instead, if we combine our results with those of

Antonietti *et al.*¹⁹ and Gower *et al.*³³ we could think of the formation of the neuron-like structures as the transformation of an inorganic/organic hybrid core consisting of amorphous micellar precursors (with a look identical to that of “ACP”, Figure 5.1b). This would be followed by the secondary nucleation of branches due to the limited feeds of reactants. Although this mechanism needs to be further investigated, the sequence of events proposed have been isolated from a synthesis reaction at the early stages of precipitation (i.e. 5 min after mixing of all reactants) and the most representative images are compiled in Figure 5.3. It is important to mention that during HR-TEM, these particular structures (the well-formed ones, Figure 5.3d) were not damaged which could otherwise cause misinterpretation of the results.

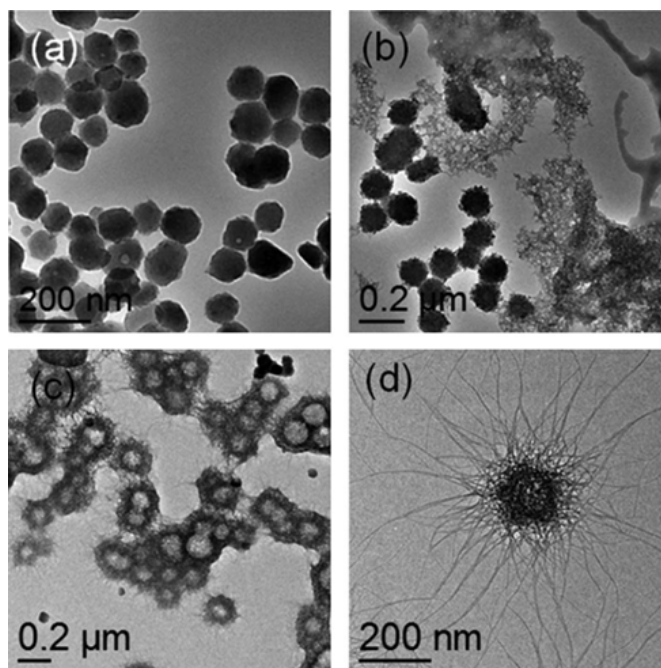


Figure 5.3 Morphological sequence of events that is believed to take place during development of the neuron-like structures. Synthesis conditions: $[Ca] = [P]_{\text{final}} = 5$ mM, TW content 0.01 wt% (a) formation of hybrid organic/inorganic clusters of amorphous precursors, (b) secondary nucleation of branches taking place on the surface of the amorphous structures, (c) further growth of the branches controlled by the diffusion of reactants and (d) a fully developed structure. Note that the hollow sphere shown in (c) is caused by excessive irradiation of the amorphous core with the electron beam. Once the whole structure is developed no irradiation damage was observed.

One aspect that should be born in mind in all the above experiments is that in spite of the remarkable structures TW can form, bulk crystallization does still take place and the coexistence of the stabilized amorphous neuron-like structure along with the crystallized phase complicates the interpretation of results.

One important question that may arise when looking at these neuron-like structures is whether they are real or they could be artifacts that formed during the preparation of TEM samples because sample isolation and drying prior to TEM imaging may induce structural changes in the samples. In spite of this, the fact is that these neuron-like structures have been reported several times under various preparation conditions showing that they are indeed real features. In the work of Antonietti *et al.*¹⁹ analytical ultracentrifugation (AUC) studies were performed to prove their existence. In our case field emission scanning electron microscopy (FE-SEM) was used to further corroborate their existence. Our hypothesis was that if these structures were artefacts, they would result from the assembly of filaments deposited on the grid upon drying, and they should form 2D structures, however, if the neuron-like structures would be real, filaments would be surrounding the whole structure forming a 3D assembly. Figure 5.4 clearly shows the 3D core of the structure and though filaments could not be seen standing up from the core, one can distinguish filaments that from the top of the structure they connect to the base (the flexible filaments upon drying stick to the structure).

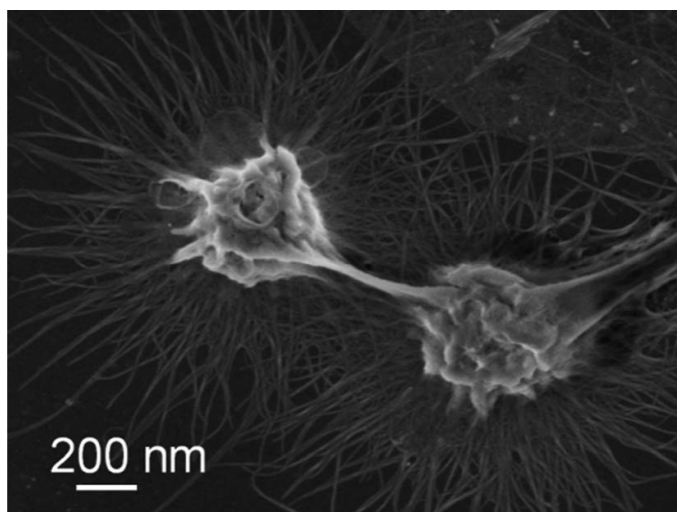


Figure 5.4 FE-SEM image of typical neuron-like structures viewed directly from a TEM grid without any preparation.

5.4.2.2 Sodium polyacrylate

Antonietti *et al.* proposed that the mechanism of formation of the neuron-like structures was tightly linked to the amphiphilic character of the organic molecule (DHBC-C₁₂).¹⁹ They observed that when the hydrophobic contribution (C₁₂ alkanes) was not present in the DHBC, the neuron-like structures could not form. The hydrophobic moieties were suggested to induce aggregation of the polymer. This simple step was however crucial as it was believed to allow sequestration/concentration of calcium ions thus serving as localized mineralization centers. A similar scenario might occur when using surfactants like TW where the hydrophilic head (e.g. that of a micelle or even that of a single molecule), rich in oxygen and thus carrying a negative density owing to the presence of electron pairs, can concentrate calcium ions and induce mineralization. The remarkably high anisotropy of the filaments suggests a strong interaction between the organic molecule and the mineral phase in the formation of the neuron-like structures³⁴ but the exact mechanism of formation still remains unclear. To prove that indeed the formation of the neuron-like structures requires of an amphiphilic molecule, sodium polyacrylate, a widely used synthetic polymer of anionic nature,³⁵⁻³⁹ was introduced in the calcium-phosphate precipitation system to replace the surfactant molecule. Presumably, with such a molecule which doesn't have an amphiphilic character, the neuron-like structures should not form as they lack of hydrophobic moieties. For this purpose a 0.06 wt% of sodium polyacrylate (PA) was first mixed with a 10 mM CaCl₂ solution onto which, an equal volume of 10 mM Na₂HPO₄ with pH adjusted to physiological value was added. Such reaction conditions were identical to those used for the TW system and served to highlight the strong impact that PA has on the nucleation of calcium phosphate. In the first place, the addition of a total of 0.03 wt% of PA into the precipitating system impeded the bulk precipitation of calcium phosphate crystals as was macroscopically observed from the clear solutions. This was also confirmed from the conductivity profile where no ACP to crystalline transition could be detected (Figure 5.5a). The reason for the inhibition of crystal formation is explained by the higher density of negative charge in the PA molecule when compared to that in the surfactant molecules which results in binding of many more calcium ions to the organic molecule thus impeding their contribution

towards bulk crystal precipitation. A TEM grid was prepared to prove whether any precipitate was formed at all and the results showed the presence of an entangled network of mineralized filaments throughout (Figure 5.5 b).

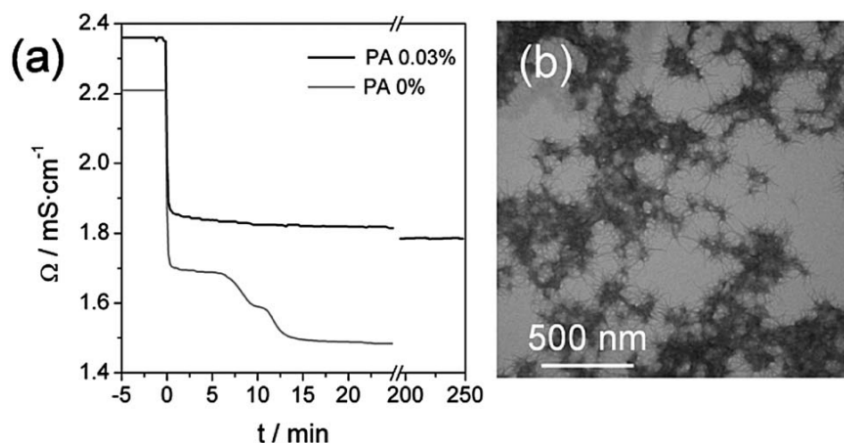


Figure 5.5 (a) Effect of the addition of sodium polyacrylate (PA) in the conductivity profile. PA was first allowed to mix with the calcium chloride solution before the phosphate solution was added at time zero. The concentrations of the salts were identical as in Fig.1. (b) TEM image resulting from the PA synthesis.

Such findings seemed to prove that indeed the lack of hydrophobic moieties could not stabilize the neuron-like structures but the striking similarity of these filament networks to the neuron-like structures suggest that the former could simply be an immature state of the later. Thus, to verify this point, several additional experiments were performed adjusting the reaction conditions. It was observed that the increase in the concentration of reagents while keeping Ca/PA and Ca/P ratio constant seemed to favour formation of the neuron-like structures (Fig. 5.6) but it was the increase in the Ca/PA ratio for a constant calcium concentration and Ca/P ratio that was critical in their stabilization (Fig. 5.7).

We believe that this increase in the Ca/PA ratio (which implies decreasing the PA content) favours the stabilization of the typically looking “ACP” globular clusters of hybrid nature which are in essence the central core of the neuron-like structures. Overall these are important results as they prove that organic molecules other than surfactants work alike. The question that follows is whether the hydrophobic moiety, so indispensable in the work of Antonietti *et al.*, is indeed necessary for the stabilization of such structures? Apparently it may seem that the answer is no, but

this would not be entirely true because upon binding of the calcium ions to the carboxylic groups from PA, neutralization of charges occurs thus rendering the molecule with a more hydrophobic character and causing their aggregation⁴⁰. This reasoning was used by Tjandra *et al.* to justify the formation of neuron-like structures with a DHBC that lacked a specially hydrophobic block.²⁰ Moreover, the same explanation might serve to justify why in the work of Peytcheva *et al.* polyaspartate was also capable of forming such structures.²¹

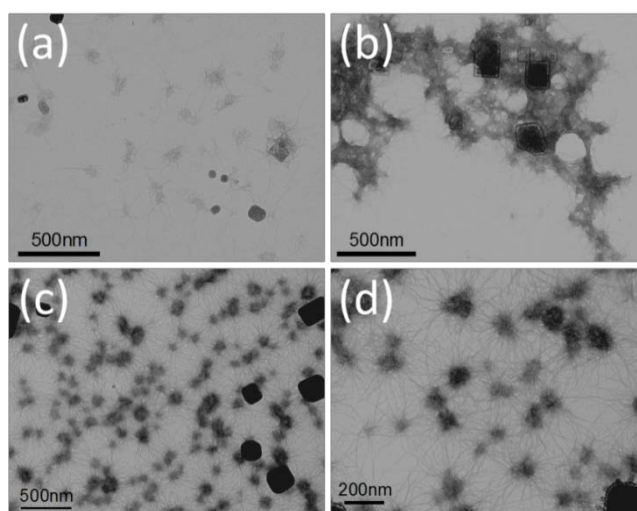


Figure 5.6 TEM images showing the effect of varying the synthesis conditions (salt concentration) in the microstructure of the precipitates. (a) and (b): $[Ca]_{\text{final}} = 15 \text{ mM}$, $Ca/PA = 20$ and $Ca/P = 1.67$; (c) and (d): $[Ca]_{\text{final}} = 50 \text{ mM}$, $Ca/PA = 20$ and $Ca/P = 1.67$.

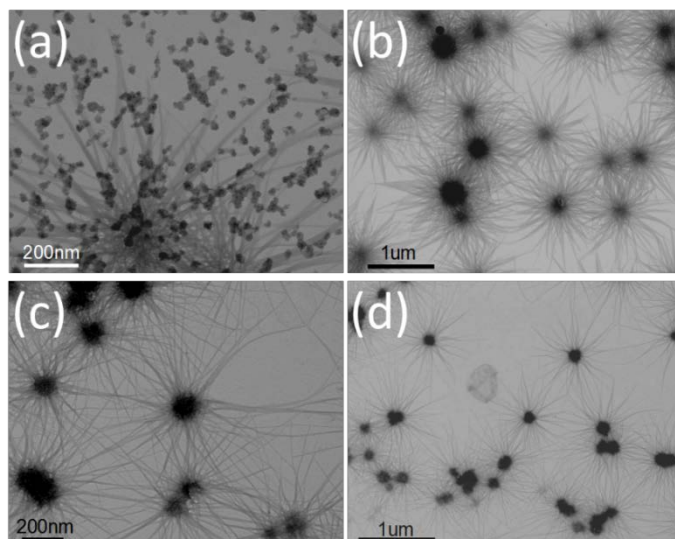


Figure 5.7 TEM images showing the effect on the microstructure of increasing the Ca/PA ratio to 80. Other synthesis conditions were: (a) and (b) $[Ca]_{\text{final}} = 15 \text{ mM}$ and $Ca/P = 1.67$; (c) and (d) $[Ca]_{\text{final}} = 50 \text{ mM}$ and $Ca/P = 1.67$.

One interesting aspect when working with ionic molecules such as PA is that tuning the pH causes different degrees of protonation of the carboxylic groups thus altering the binding ability towards calcium. This effect has been investigated with regards to the formation of neuron-like structures and the results are summarized in Figure 5.8.

Figure 5.8a represents the graphs obtained after titration of a 10mM calcium chloride with a 10mM sodium polyacrylate solution (1 wt %) added droplet by droplet into the system at a rate of 0.5 ml/min. The pH of both solutions was previously adjusted to: 3, 7 and 10. As can be observed from the pH 3 curve, since the moment of addition of the PA (time zero), the conductivity of the system rises gradually indicating that there is no interaction between the protonated carboxylic groups with calcium. At pH 7 and 10, the scenario changes as observed from the curves obtained. At the beginning, the addition of PA does not seem to alter the conductivity of the system and only after a specific time it starts rising. This apparently unperturbed behaviour at the beginning of the titration is an indication that the de-protonated carboxylic groups are binding calcium ions thus they do not contribute rising the conductivity of the system. After a specific time, however, the conductivity begins to increase indicating that all de-protonated carboxylic groups have already been calcium bound. Surprisingly, no significant differences were detected when comparing the profiles run at pH 7 and 10. We believe however, that this might be caused by the design of the experiment. The addition of PA droplet by droplet onto a calcium solution results in a huge amount of calcium ions that may force a fast coiling of the PA burying some unreacted carboxylic groups within the coiled structure. By simply performing the experiment vice versa, i.e. by adding droplet by droplet calcium ions into the PA solution (Figure 5.8b), this problem was solved and as can be judged from Figure 5.8b the profiles now revealed what one would have expected: that the fully de-protonated PA at pH 10 would be more efficient at neutralizing the calcium in solution than at pH 7.

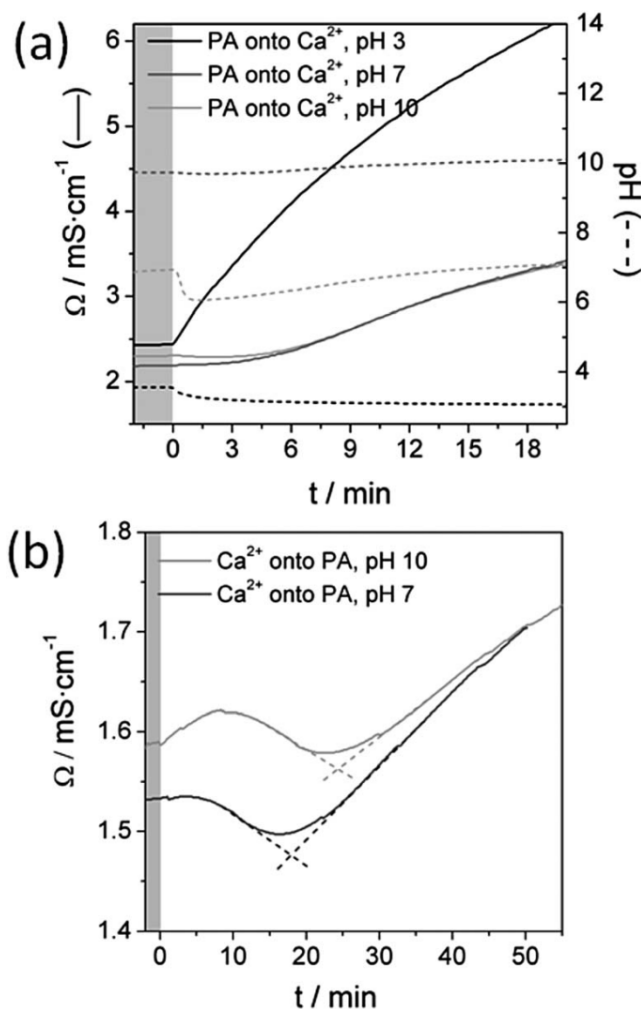


Figure 5.8 Changes in conductivity during titration of (a) 10 mM PA added at a 0.5 ml/min rate into 15 ml of 10 mM CaCl₂ solution at various pH: 3, 7 and 10, and (b) titration profile of 10 mM CaCl₂ added at a 0.5 ml/min rate onto 15 ml of 2 mM PA at pH 7 and 10. The intersection points shown in (b) indicate the Ca/PA ratio needed to neutralize the carboxylic groups available in PA (Ca/PA = 4 at pH 10 and Ca/PA = 3 at pH 7).

To validate if these different scenarios affected the formation of the neuron-like structures, TEM grids were prepared upon mixing Ca+PA with the Na₂HPO₄ at the various pH. Regardless of the Ca/PA ratio and the concentration of reactants, the pH of the reaction had a strong impact in the formation of the neuron-like structures. Working at pH 3 macroscopically yielded clear solutions (with no bulk CaP precipitation) but microscopically revealed the presence of the typical neuron-like structures of various sizes along with the formation of long twisted bundles as can be observed from Figure 5.9c. At first sight this result might seem surprising as one would expect that without interaction of the calcium ions with the protonated carboxylic groups in PA, there should not be formation of the neuron-like

structures. However we already proved that with organic molecules with non-bearing charges (anionic surfactants) it was already possible to form these structures. Thus working at pH 3 simply confirmed that the formation of the neuron-like structures can take place via weak electrostatic forces of ion-dipole (Ca^{2+} -COOH) nature and not necessarily through ion-ion bonding (Ca^{2+} -COO⁻).

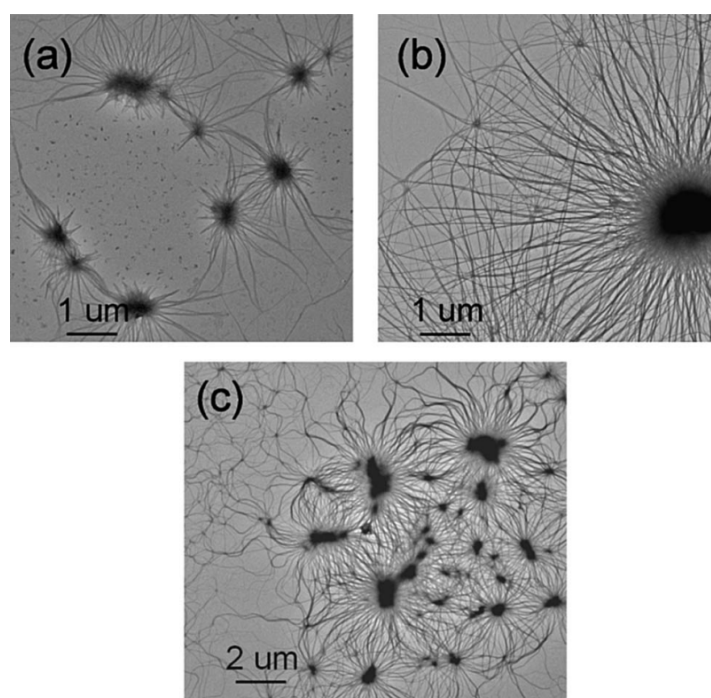


Figure 5.9 TEM images obtained from synthesis reactions in the presence of PA at pH 3 and Ca/PA= 80. (a) $[\text{Ca}]_{\text{final}} = 5 \text{ mM}$, (b) $[\text{Ca}]_{\text{final}} = 15 \text{ mM}$ and (c) $[\text{Ca}]_{\text{final}} = 50 \text{ mM}$. Ca/P= 1.67. Although figure (a) is representative of all conditions, other interesting microstructure has been selected in conditions (b) and (c).

At pH 10, and at a calcium concentration low enough to minimize $\text{Ca}(\text{OH})_2$ precipitation, there was no formation of the neuron-like structures and, instead, it was observed the bulk precipitation of HA. Macroscopically, this pH condition yielded an opaque solution evidencing HA crystallization. Working at neutral pH gave an intermediate condition in which the neuron-like structures coexisted with other amorphous structures. The apparently contradictory result from the lack of neuron-like structures in a condition where most of the carboxylic groups of PA were de-protonated (high pH), and therefore bound to calcium, can be explained by a too strong driving force towards HA precipitation at this particular pH¹⁸. The continuous formation of HA crystals would lead to the gradual depletion of the calcium bound to PA to further contribute to HA precipitation.

The various experiments performed with PA as growth directing unit have proven that such a molecule can form identical neuron-like structures than those obtained with the help of surfactants but with the additional advantage that under proper adjustment of the reaction conditions the product could be made practically pure. Although the mechanism of formation is not totally understood, the results with PA evidence that the need of working with organic amphiphilic molecules (hydrophobic-hydrophilic) is not compulsory and the formation of the neuron-like structures is rather a generic phenomenon. Whether this apparently simple mechanism of formation is particular of the cation/organic molecule system or not, will be explored in the next section by investigating the feasibility of inducing similar structures with the help of a cationic polymer. The goal would thus be to prove if the cationic polymer is capable of directing anion binding (phosphate group) towards formation of the neuron-like structures.

5.4.2.3 Polydiallyldimethylammonium chloride

As cationic polymer polydiallyldimethylammonium chloride (PDMAC), a strong polyelectrolyte, was chosen for this particular study. Being a strong polyelectrolyte the charge of this polymer is not affected by the pH; thus, all experiments were done at one pH condition only, i.e. close to neutrality. In a typical synthesis reaction PDMAC was first mixed with the phosphate salt to facilitate interaction of the anion with the molecule and then calcium chloride was added to precipitate the calcium phosphate. Two different concentration of PDMAC, 0.1 and 0.001 wt%, were explored. The concentration of the calcium and phosphate solutions used was the same as those chosen in the PA experiments, i.e. $[Ca^{2+}]_{final} = 50$ mM and $[P]_{final} = 30$ mM, to allow comparison of results. These high concentrations were purposely selected to favour neutralization (by charge screening) of the amine groups from the polyelectrolyte and induce coiling/aggregation of the polymer. The coiled structure should then act concentrating phosphate ions that would serve as nucleation center in the formation of the neuron-like structures. Regardless of the content of PDMAC the synthesis reaction followed the profile shown in Figure 5.10a in which amorphous and crystallized phases could be distinguished (refer to the pH profile). The most important fact was, however, that even after crystallization took place, amorphous structures resembling the neuron-like

structures were also formed in this particular setup (Figure 5.10). It should be mentioned however, that with this particular polymer the structures were not stable and after a few days they disappeared.

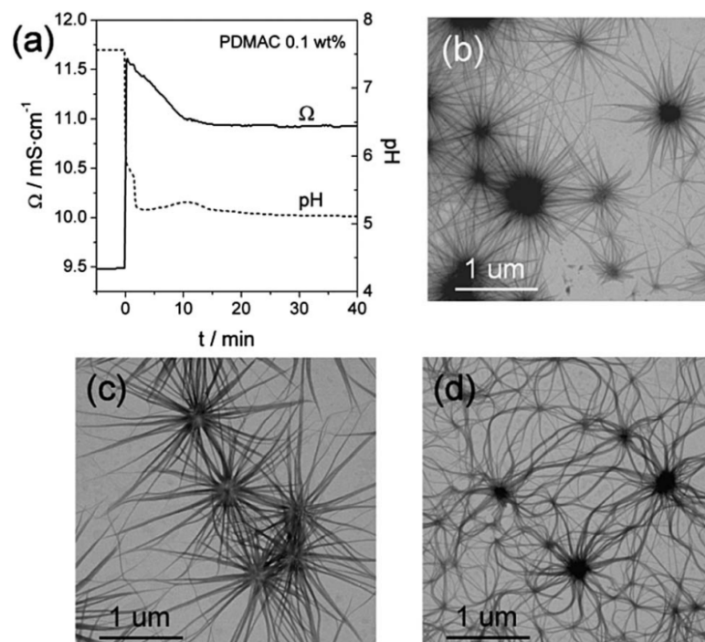


Figure 5.10 (a) Effect of the addition of polydiallyldimethylamino chloride (PDMAC) in the conductivity and pH profile. PDMAC was first allowed to mix with the phosphate solution before the calcium chloride solution was added at time zero. TEM images of structures stabilized with a 0.1 (b) and 0.001 wt% (c and d) of PDMAC. $\text{Ca/P} = 1.67$ and $[\text{Ca}]_{\text{final}} = 50 \text{ mM}$. The TEM grids were prepared from the supernatant (the large crystallized product was concentrated in the sediment).

The results thus far clearly demonstrate that formation of the neuron-like structures is governed by a generic mechanism in which the organic molecule serves as a substrate for CaP precipitation and at the same time directs the growth/assembly towards the final structure. Whether the organic molecule is negatively or positively charged, or does not have any charge at all does not seem to be critical in the stabilization of the structures as in all cases the neuron-like structure can form. An interesting aspect to note is that in spite of the high anisotropy of the filaments, which underlines a tight interaction between the organic molecule and the inorganic phase, these structures can form through weak electrostatic forces as was confirmed in the experiments with non-ionic surfactants and also PA at pH 3. Moreover, we have also proved that such structures can be stabilized regardless if the polymer associates first with the

anion (PDMAC with the phosphate ion) and then the cation is added, or vice versa (PA with the calcium ion). But in spite of their facile formation not all conditions allow their stabilization. Insufficient levels of calcium and phosphate can only stabilize a filamentous structure and a too high content of the organic molecule adversely affects their formation by quenching the mineralized nuclei and impeding their subsequent assembly. The need of high ionic strengths when dealing with polyelectrolytes (PA and PDMAC) we believe that is to ensure coiling of the molecule since in environments of low ionic strength the charged areas on the polymer chain repel each other and force the chain to uncoil.^{40,41} Instead, at high ionic strengths the small ions screen the charges from the polymer causing it to coil. Thus, the high content of calcium and phosphate ions required for the neuron-like formation in the case of PA and PDMAC seem to agree well with the fact that the polymer need to cluster/aggregate first prior to their formation but any further insight into the full development of the final structure is out of the scope of the work.

5.4.3 Neuron-like structures analysed by TEM-based techniques

As shown in the previous section, neuron-like structures can be synthesized not only with participation of double hydrophilic block copolymers during calcium phosphate precipitation, as reported in the literature, but also using more simple organic molecules such as surfactants (Tween 80) as well as anionic and cationic polymers (sodium polyacrylate and polydiallyldimethylammonium chloride). However, very limited chemical and structural characterization has been carried out on these structures due to the difficulty to isolate them (probably because of their limited amount in solution) and their poor stability resulting from the amorphous characteristic. In the previous section, to prove the presence of neuron-like structures in solution, bright-field TEM images were acquired. As shown, all neuron-like structures consisted of a dense core with filaments surrounding them. However, the details of the dense core were not clear owing to the high absorbance of the electron beam in the dense areas of the sample. In addition, selected area electron diffraction (SAED) was done proving that the

neuron-like structures were amorphous in nature. Besides these very basic features, nothing else was known and the need of gaining more understanding becomes crucial to elucidate their nature and the mechanism of formation. For this purpose several analytical TEM-based methods such as high angle annular dark field (HAADF)-STEM, energy filtered transmission electron microscopy (EFTEM) and electron energy loss spectroscopy (EELS) were employed in the characterization of these structures. The samples were prepared in the presence of sodium polyacrylate under the specific condition of pH=3, Ca/PA=80, $[Ca]_{\text{final}}=50$ mM and Ca/P=1.67, to favour only the presence of neuron-like structures without inducing any bulk crystal precipitation.

5.4.3.1 High angle annular dark field - scanning transmission electron microscopy

The neuron-like structure was first observed by scanning transmission electron microscopy (STEM) equipped with a high angle annular dark field (HAADF) detector. HAADF-STEM imaging results in Z-contrast images due to Rutherford scattering⁴², where the intensity is a function of the $Z^{1.7-2}$ (Z represents for atomic number). The contrast of HAADF-STEM images is strongly dependent on the average atomic number of the samples, thus, this technique provides an ideal method to image elements with high atomic number in a low Z background^{42,43}. Accordingly, regions containing heavy elements appear bright in HAADF-STEM.

Figure 5.11 displays the HAADF-STEM images acquired from the dense core as well as the filaments of neuron-like structures. Although HAADF-STEM does not allow the determination of calcium phosphate phase⁴⁴, this technique supports the earlier claims of calcium phosphate filaments formation. In our case, the high contrast between the neuron-like structure and the background should be assigned to the deposition of calcium phosphate. In comparison with bright-field TEM, the images acquired by HAADF-TEM clearly showed that the typical neuron-like structures consisted of a denser filamentous core and the interlaced thin filaments stretched out from the center in a circular form.

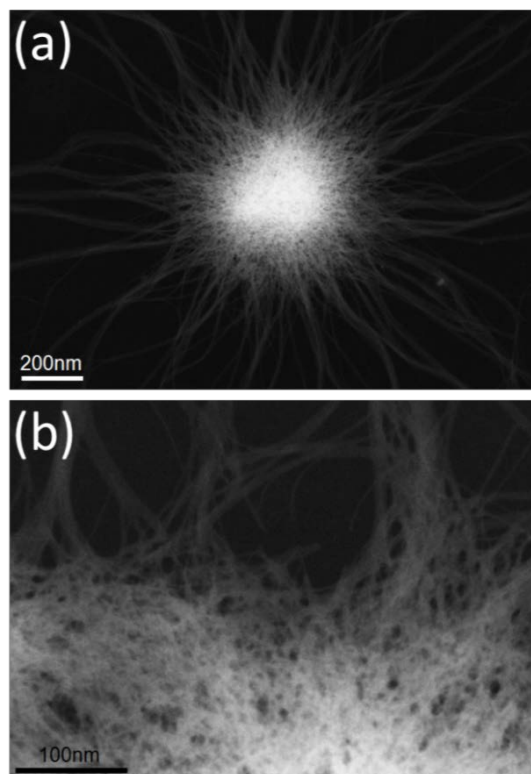


Figure 5.11 HAADF-STEM images of the typical neuron-like structures (a) view of the whole neuron-like structure, (b) detail of the core. The neuron-like structures were formed under the specific condition of pH=3, Ca/PA=80, $[Ca]_{\text{final}}=50$ mM and Ca/P=1.67.

5.4.3.2 Electron energy-loss spectroscopy

EELS of calcium $L_{2,3}$ edges, oxygen K edge and phosphorous $L_{2,3}$ edges acquired from the typical neuron-like structures are shown in Figure 5.12. EELS analysis of the neuron-like structures identified characteristic peaks of phosphorus $L_{2,3}$ edges and calcium $L_{2,3}$ edges (L_3 and L_2 edges representing excitation of $2p^{3/2}$ and $2p^{1/2}$ electrons, respectively). The positions of the main L_2 peak located at ~ 352.1 eV and L_3 peak located at ~ 348.9 eV proved the presence of calcium elements in the neuron-like structures, and the phosphorus $L_{2,3}$ edge contains characteristic double peaks at 138.1 and 146.2 eV followed by another intense broad peak⁶. In addition, the spectra also demonstrated the distinctive peak of oxygen K edge at 539.5 eV. In conclusion, the neuron-like structures were confirmed to consist of calcium, phosphorus and oxygen elements by EELS, which further proved the presence of calcium phosphate materials in neuron-like structures.

Moreover, it is important to note that various EELS spectra were acquired from different neuron-like structures and all gave very similar profiles indicating that the neuron-like structures were very reproducible in TEM-EELS.

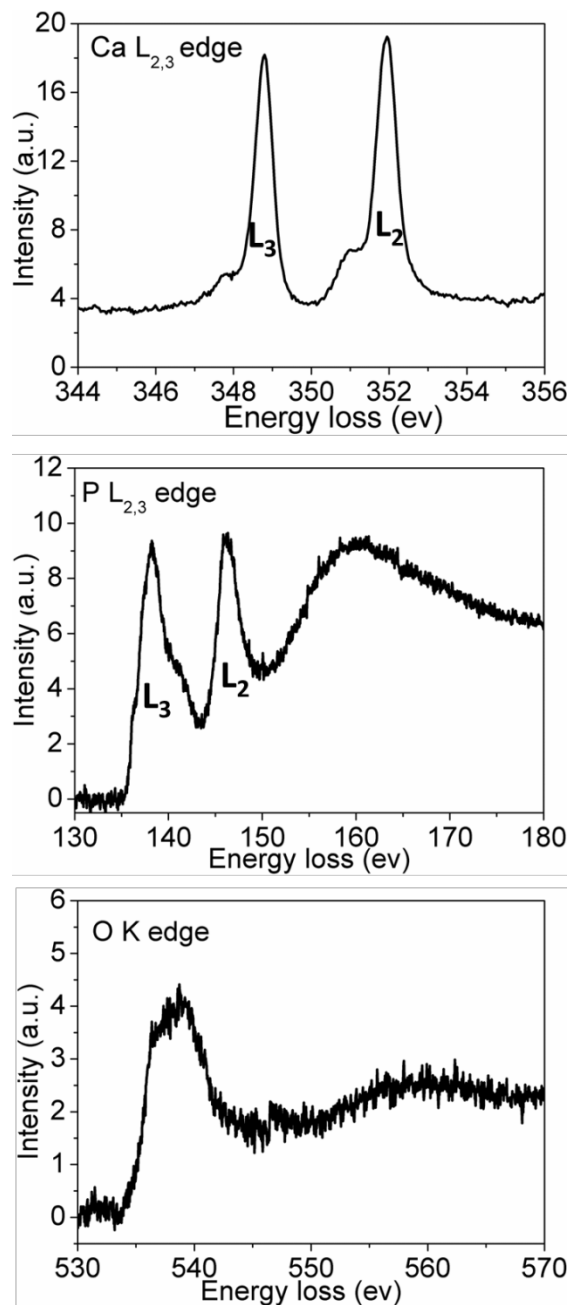


Figure 5.12 Representative EELS of Calcium L_{2,3} edges, Phosphorous L_{2,3} edges and Oxygen K edge of neuron-like CaP structures prepared under the specific condition of pH=3, Ca/PA=80, [Ca]_{final}=50 mM and Ca/P=1.67.

In order to further verify the calcium phosphate phase of the neuron-like structure, the calcium L_{2,3} edges of the neuron-like structures obtained by EELS were

compared with analogous X-ray adsorption near edge structure (XANES) spectra acquired for reference compounds from the literature (i.e. HA and ACP, Figure 5.13)⁶.

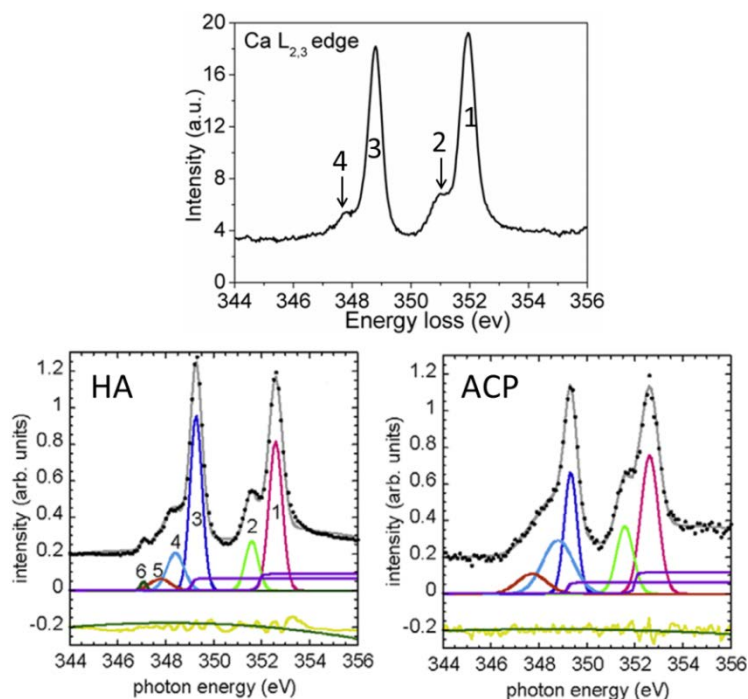


Figure 5.13 Energy loss of the calcium $L_{2,3}$ edge of the neuron-like structure compare with XANES spectra from literature acquired for the reference standard minerals hydroxyapatite (HA) and amorphous calcium phosphate (ACP) at the Ca $L_{2,3}$ edge.⁶

XANES is an absorption spectroscopy technique that indicates the features in the X-ray absorption spectra of samples due to the photon absorption for electronic transitions from an atomic core level to final states. This technique provides great power to specifically detect every element within the sample based on the fact that each element has different core level energies. XANES can also determine the chemical state of elements. By efficiently measuring XANES of samples at high spatial resolution, it produces information analogous to that delivered by EELS in a TEM⁴⁵.

As shown in Figure 5.13, the positions of the main L_3 and L_2 peaks of Ca L-edge spectra in the neuron-like CaP materials are similar to that of reference HA and ACP compounds from literature, thus it is very difficult to distinguish them just by looking at the main peaks $L_{2,3}$. However, looking carefully at the smaller peaks -

Figure 13 peaks 2 and 4- which are associated to the crystal field, they are quite distinct and enable further identification of the sample⁶. The intensities of peak 4 in ACP standard and neuron-like materials are lower than that in HA standard indicating lower crystallinity⁴⁶. This result suggested the amorphous phase of neuron-like structure being consistent with the SAED results in Figure 5.2.

5.4.3.3 Energy-filter transmission electron microscopy

As discussed in materials and methods section, EFTEM is coupled with principles of EELS to yield a filtered image. By placing an adjustable slit to allow only the energy-loss electrons contributing to ionization edges of elements through, EFTEM enables the rapid acquisition of elemental maps in TEM thin sections³². EFTEM technique is particularly efficient for light elements and, unlike HAADF-STEM, enables to separately determine the distribution of multiple elements within the same sample area. Figure 5.14 shows a representative bright field TEM image along with the corresponding calcium, phosphorus and oxygen distributions obtained using EFTEM mapping.

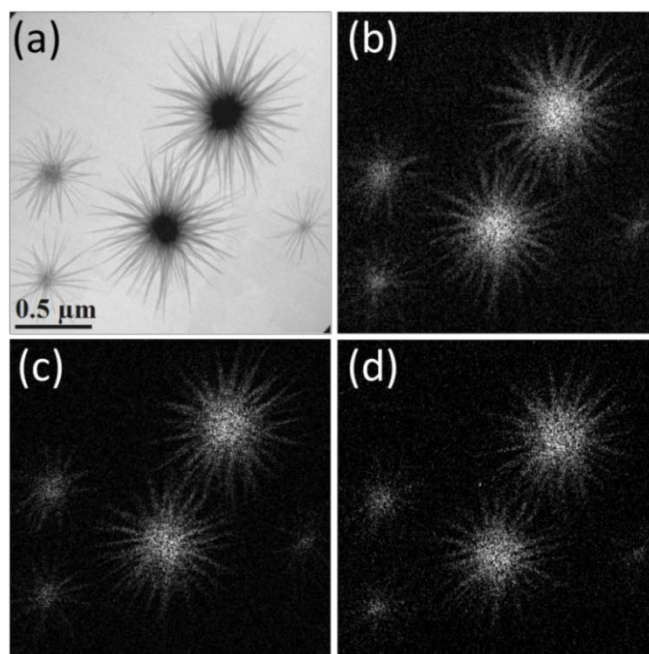


Figure 5.14 EFTEM images of the neuron-like structure. a shows the BF-TEM image; b, c and d show the elemental maps of calcium, phosphorus, and oxygen, respectively. Brighter areas indicate the presence of larger amounts of the respective element than the dark areas.

In spite of the low signal-to-noise ratio, the calcium, phosphorus and oxygen atoms distributions closely resemble each other and show the association of calcium phosphate in these dense cores and filaments.

5.4.4 Co-effect of ions and organic molecules on CaP precipitation

Besides organic molecules, ions other than Ca^{2+} and PO_4^{3-} in the physiological environment also play important roles in biomineralization as discussed in the introduction of this chapter. However, there are still very limited studies targeting the co-effect of ions with organic molecules on CaP mineralization²⁸. In the previous sections neuron-like CaP structures were synthesized with the help of organic molecules and were further analysed using TEM-based methods. In this section, ions like Mg^{2+} and Sr^{2+} will be introduced together with organic molecules into the calcium phosphate system to investigate whether foreign ions affect the formation of neuron-like structures.

5.4.4.1 Co-effect of magnesium with surfactant

It has been well known that Mg^{2+} ions are effective inhibitors of HA crystal nucleation and growth. In fact, the significant amounts of Mg^{2+} ions that are present in animal skeletons are believed to stabilize amorphous calcium phosphate (ACP) mineral phases^{25,27,28,47}. Since the typical neuron-like structure was determined to be amorphous calcium phosphate phase by SAED (Figure 5.2c), introducing Mg^{2+} into the system of CaP precipitation could prevent the conversion of HA and form neuron-like structures without inducing any crystalline phase precipitation. Although it was observed that working at pH 3 already helped “creating” pure neuron-like structures without inducing any precipitation, the idea was to assess if Mg^{2+} could also prevent crystallization while avoiding the “harsh” working environment from the acidic pH.

Thus, the effect of Mg^{2+} ions on the transformation of ACP into HA was first investigated by monitoring the conductivity profiles of CaP precipitation. As shown in Figure 5.15, the addition of Mg^{2+} delayed the induction time which appeared after 30 min when the Mg/Ca molar ratio was 1. Unfortunately, increasing the

amount of Mg^{2+} ions any further in CaP solution could not inhibit the conversion of crystalline phase totally.

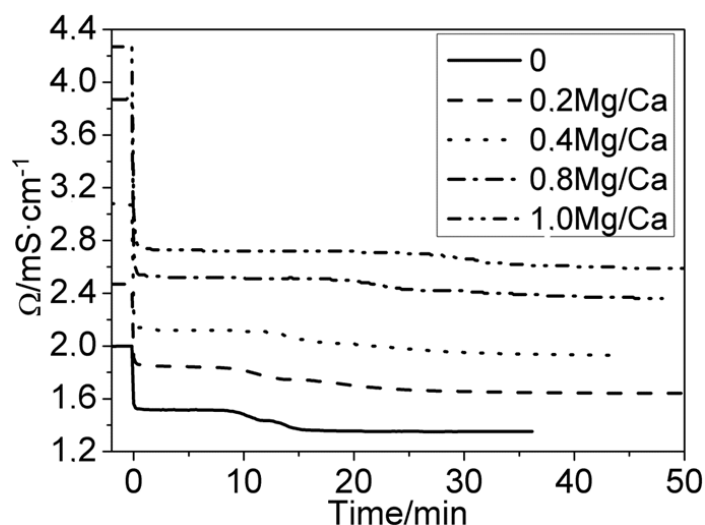


Figure 5.15 Conductivity profiles of calcium phosphate precipitation. (a) MgCl_2 salt was allowed to mix with the calcium chloride solution prior to the addition of phosphate solution at time zero. The experiments were performed under the conditions: Mg/Ca molar ratio varied from 0.2 to 1.0, $[\text{Ca}]_{\text{final}}=5\text{mM}$, $\text{pH}=7.4$, Ca/P molar ratio is 1. Control sample (without Mg ions) is labelled as 0.

Although Mg^{2+} was unable to completely prevent ACP conversion to the crystalline phase, it was still worthy to investigate the co-effect of Mg^{2+} and TW molecules on the CaP precipitation as well as on the formation of the neuron-like structures. The working conditions were as follows: molar ratio of Mg/Ca was 0.2 and the Ca/P molar ratio was 1, the concentration of TW was set to 0.1 wt% in the CaP solution, as it was already determined that this concentration could form neuron-like structures (Figure 5.2b). The co-effect of Mg and Tween on the conductivity profiles during CaP precipitation is shown in Figure 5.16a. Mg^{2+} together with Tween 80 molecules delayed the conversion towards the crystalline phase significantly as the induction period from ACP to the crystalline phase was increased by at least two times as compared to Mg^{2+} ions or Tween molecules alone.

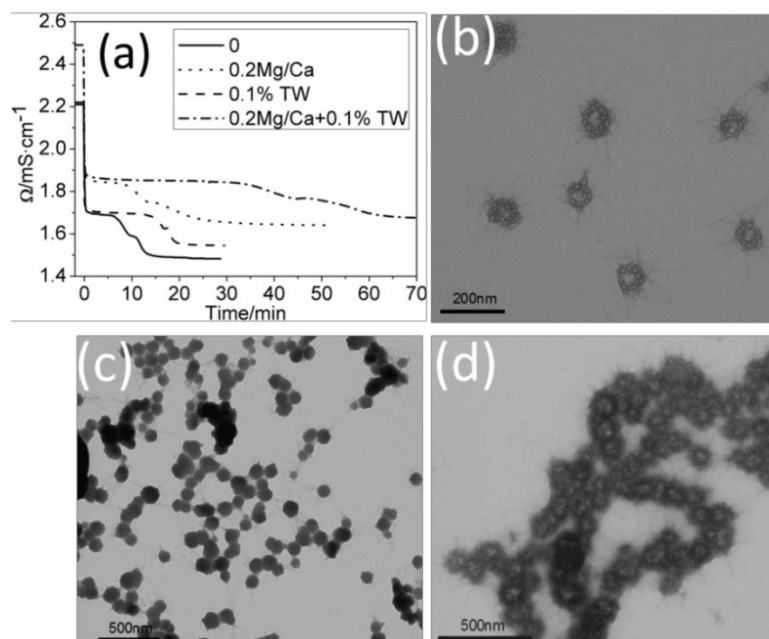


Figure 5.16 The co-effect of Mg ions with TW molecules on conductivity profiles (a) as well as on neuron-like structure (b, c and d) (Molar ratio Mg/Ca=0.2, the amount of TW in the solution is 0.1 wt%, $[Ca]_{final}=5mM$, Ca/P molar ratio is 1). $MgCl_2$ salt together with TW molecules were allowed to mix with the $CaCl_2$ prior to the addition of phosphate solution at time zero. TEM samples were prepared 20min after adding the phosphate solution.

The co-effect of Mg^{2+} and Tween molecules on neuron-like structure formation were determined by TEM (Figure 5.16 b, c and d). TEM samples were prepared 20min after the addition of the phosphate solution into the calcium solution containing Mg^{2+} and TW. At this time point, there was no crystal formation yet because the sample was prepared within the period of ACP stability (Figure 5.16a). The morphologies of the structures consisted of micelle aggregates (Figure 5.16b) having filaments surrounding them. These structures can form owing to the presence of TW molecules as a result of their amphiphilic properties. In addition, a few spheres that closely resembled ACP (Figure 5.1b) having thin filaments surrounding them were also formed as shown in Figure 5.16c. Figure 5.16d displayed the aggregation of typical neuron-like structures with morphology similar to that found in Figure 5.3. The influence of Mg^{2+} on neuron-like structure formation became evident from TEM analysis of the samples prepared a couple of hours after time zero. As shown in Figure 5.17 only a few ACP spheres, aggregated dots and clusters were found in the CaP solution. All formed neuron-like structures and filaments disappeared in a few hours suggesting that Mg ions had indeed a

strong impact in neuron-like structure formation and unfortunately rather than helping stabilizing the structure they un-stabilize them.

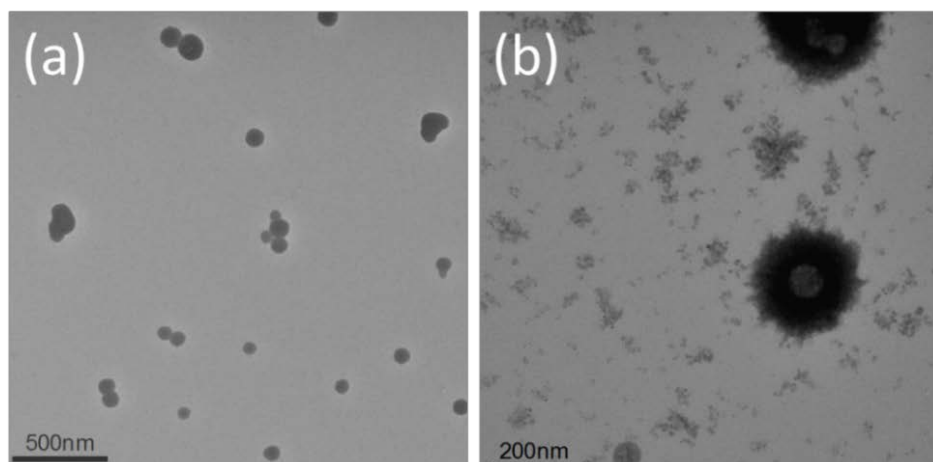


Figure 5.17 Co-effect of Mg ions with TW molecules on neuron-like structure formation. Samples (a) and (b) were prepared a couple of hours after time zero (Mg/Ca=0.2, the amount of TW in the solution is 0.1 wt%, $[Ca]_{\text{final}}=5\text{mM}$).

5.4.4.2 Co-effect of magnesium with sodium polyacrylate

As discussed in section “5.4.2.2” sodium polyacrylate had a remarkable effect on the precipitation of calcium phosphate neuron-like structures. Under the specific condition of $\text{-pH}=3$, $\text{Ca/PA}= 80$, $\text{Ca/P}= 1.67$, $[Ca]_{\text{final}}=50\text{mM}$ - pure neuron-like structures could be obtained without inducing any bulk precipitation. The effect of Mg ions was also explored under these specific conditions to assess if the neuron-like structures could be created using PA. TEM samples prepared at two different time points, one hour and one day after addition of the phosphate solution into the calcium solution (time zero), proved that formation of neuron-like structures was possible but the structures were not stable with time (Figure 5.18).

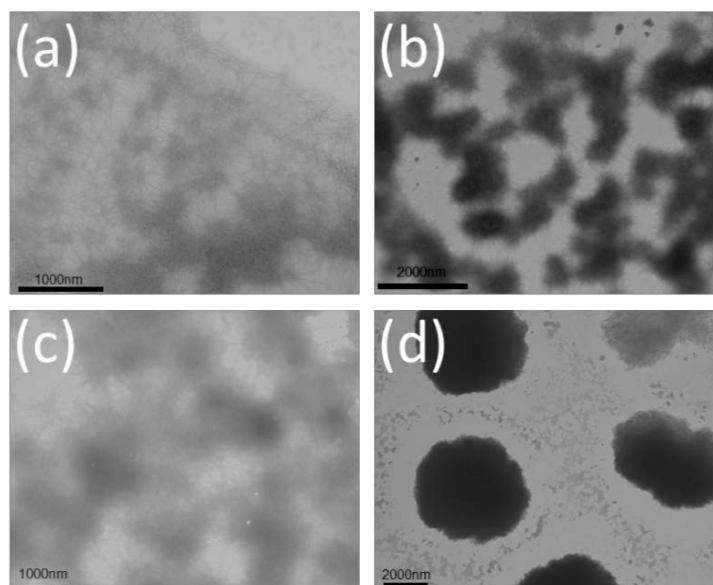


Figure 5.18 TEM images of samples that were obtained from CaP mineralization in the presence of PA and Mg^{2+} ions at pH 3 ($Ca/PA= 80$ $[Ca]_{final}= 50$ mM, $Mg/Ca=0.1$, $Ca/P= 1.67$). TEM samples (a) and (b) were prepared in 1 hour after time zero; (c) and (d) samples were prepared after 1 day.

As shown in Figure 5.18a and b, both filaments and the neuron-like structures were found after one hour of mixing the Ca and P salts, however, as time increased, these structures disappeared which is consistent with the results of TW. Again, a few big clusters were formed with small dots surrounding (Figure 18d) after one day and seemed to be formed by the fusion of many neuron-like structures along with the degradation of filaments. In conclusion, the presence of Mg^{2+} in the CaP solution destabilizes the neuron-like structures regardless of the nature of the organic molecule added in the CaP solution.

5.4.4.3 Co-effect of strontium ions with surfactant

Sr ions as trace elements in the human body play a very important role in bone metabolism and formation. Although the most extensively investigated metal ion inhibitor for ACP transformation is Mg^{2+} , Sr ions have been observed to behave the same way as that of Mg ions^{27,48}. The effect of strontium ions during CaP precipitation was assessed monitoring conductivity profiles as shown in Figure 5.19. Sr^{2+} , similarly to what was observed for Mg could not stop the conversion to HA even when the molar ratio of Sr/Ca was increased to 0.2. One aspect to note is that for Sr the molar ratio of Sr/Ca was not as high as that of Mg/Ca in the previous

section. The reasons were that on one hand, according to literature the ability of Sr as inhibitors of transformation of ACP is much weaker than Mg^{2+} stabilizing ACP²⁷, on the other hand, in the physiological environment in the human body, the content of Sr^{2+} was much lower than that of Mg^{2+} . However, it was very interesting to observe that unlike for Mg, the influence of Sr^{2+} on the neuron-like structure in the presence of 0.1 wt% TW molecules was positive. Thus, TEM samples prepared one day after time zero indicated that typical neuron-like CaP were still present and Sr ions did not destabilize them (TEM images were not shown). Using the same molar ratio but for Mg, the neuron like structures were unstable.

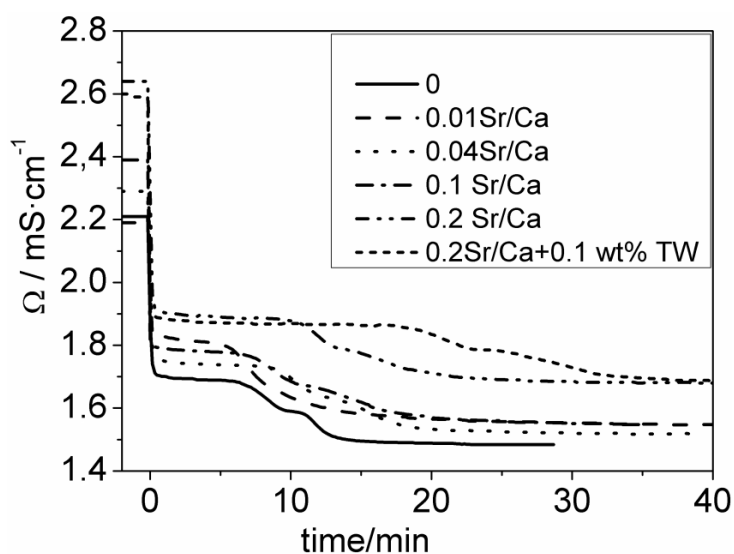


Figure 5.19 Conductivity profiles of calcium phosphate precipitation. $SrCl_2$ salt was allowed to mix with the calcium chloride solution prior to the addition of phosphate solution at time zero. The experiments performed under the conditions: Sr/Ca molar ratio varied from 0.01 to 0.2, molar ratio Ca/P=1, $[Ca]_{final}=5mM$, 0.1 wt% TW in the solution at pH 7.4. Control sample (without Sr) is labelled as 0.

5.4.4.4 Co-effect of strontium ions with sodium polyacrylate

The effect of Sr ions on PA-created neuron-like structure was also investigated following the same procedure as for Mg ions. As shown in Figure 5.20, unlike Mg^{2+} ions, Sr^{2+} ions in the CaP solution were not interfering in the formation of typical neuron-like structures, and as time increased the neuron-like structures remained stable in the CaP solution (Figure 20 c and d). In conclusion, Mg ions and Sr ions were shown to exhibit opposite impact on the neuron-like structures, while Mg ions destabilize them, Sr ions did not affect their formation and stability in solution.

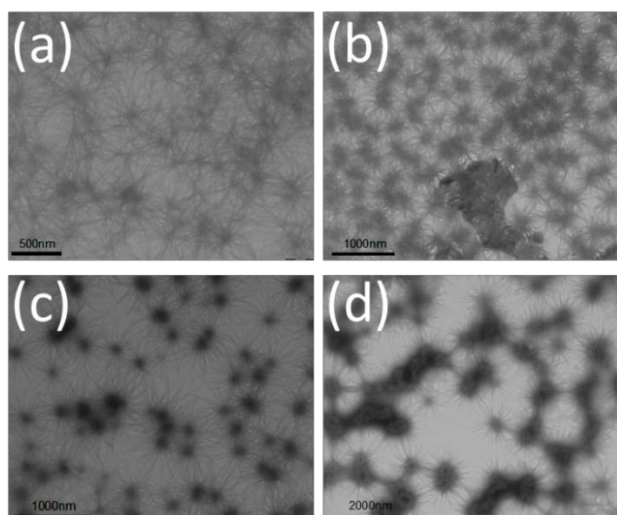


Figure 5.20 TEM images of samples that were obtained from CaP mineralization in the presence of PA and Mg^{2+} ions at pH 3 ($Ca/PA= 80$ $[Ca]_{final}= 50$ mM, $Sr/Ca=0.1$, $Ca/P= 1.67$). TEM samples a) and b) were prepared in 1 hour after time zero; c and d samples were prepared after 1 day.

The mechanism behind this distinct behaviour is not well understood but it could be interpreted from the different roles of Mg^{2+} and Sr^{2+} in CaP precipitation from supersaturated solutions. According to the literature, absorption of Mg on ACP are able to prevent the nucleation of HA in supersaturated Ca and PO_4 solutions by stabilizing ACP phases, however, Mg ions were not detected in either the ACP or final crystalline phase on the reported works²⁸. Based on the fact that in the presence of Mg^{2+} at the beginning of precipitation of CaP the neuron-like structures formed and was only afterwards that disaggregated, one possibility would be that at the beginning Mg ions could be incorporated in the neuron-like CaP structures and as time increased Mg ions could be released via “specific pathways” meanwhile damaging the neuron-like materials. On the other hand, Sr ions were also shown to stabilize or delay the transformation of the unstable ACP phase. However, unlike Mg ions, Sr ions were found to be incorporated into both ACP and the crystal lattice of HA crystals⁴⁸. Based on these studies, it was reasonable to assume that Sr ions could incorporate in ACP, and the so-formed neuron-like structures could be Sr-substituted CaP materials. Another possibility could also be that Sr ions have less competition than organic molecules when absorbing on ACP and the neuron-like structures could be formed with the organic molecules without incorporating any Sr ions. If this scenario occurred, the neuron-

like structures would also be stable in the solution. These assumptions about the different impact of Sr and Mg ions on neuron-like structure will be further confirmed in the near future.

5.5 Conclusions

The results presented in this chapter show that the formation of calcium phosphate neuron-like structures occur through a more generic mechanism than the one established with the help of complex double hydrophilic block copolymers. Identical structures were formed using simple amphiphilic molecules of non-ionic nature (Tween 80), anionic polymers (sodium polyacrylate) and cationic polymers (polydiallyldimethylammonium chloride) combined with calcium and phosphate salts at nearly ambient conditions. In spite of the high anisotropy of the resulting structures which accounts for a tight inter-digitation between the organic and inorganic phase, such structures can be stabilized by weak electrostatic forces of ion-dipole nature. The reaction conditions were found to be critical in stabilizing this particular type of structures and determined the purity of the product. Within the range of conditions investigated only with the addition of PA, and under specific conditions, the neuron-like structure could be obtained practically pure without any bulk crystal precipitation. In all other cases, the formation of these structures competed with the precipitation of CaP crystals. The facile stabilization of such structures under ambient conditions makes them potential candidates for biomineralization reactions but also offer the means of synthesizing a new class of structures with additional properties.

Detailed TEM investigation proved that the neuron-like structures were amorphous calcium phosphate as calcium, phosphorous and oxygen elements were found to distribute throughout the dense core as well the filaments. In addition, it was shown that the addition of different ions during the formation of these hybrid structures had a strong impact on neuron-like structure formation. The incorporation of Mg ions destabilized the neuron-like structures while Sr ions did not affect their formation and stability in solution.

5.6 References

1. Weiner, S., Israel, R., Dove, P. M., Tech, V. & Virginia, U. S. A. An Overview of Biomineralization Processes and the Problem of the Vital Effect. *Rev. Mineral. geochemistry* **54**, 1–29 (2001).
2. Meldrum, F. C. & Cölfen, H. Controlling mineral morphologies and structures in biological and synthetic systems. *Chem. Rev.* **108**, 4332–4432 (2008).
3. Kakizawa, Y., Miyata, K., Furukawa, S. & Kataoka, K. Size-Controlled Formation of a Calcium Phosphate-Based Organic-Inorganic Hybrid Vector for Gene Delivery Using Poly(ethylene glycol)-block-poly(aspartic acid). *Adv. Mater.* **16**, 699–702 (2004).
4. Chen, P.-Y., McKittrick, J. & Meyers, M. A. Biological materials: Functional adaptations and bioinspired designs. *Prog. Mater. Sci.* **57**, 1492–1704 (2012).
5. Mahamid, J., Sharir, A., Addadi, L. & Weiner, S. Amorphous calcium phosphate is a major component of the forming fin bones of zebrafish: Indications for an amorphous precursor phase. *PNAS* **105**, 12748–12753 (2008).
6. Beniash, E., Metzler, R. a, Lam, R. S. K. & Gilbert, P. U. P. a. Transient amorphous calcium phosphate in forming enamel. *J. Struct. Biol.* **166**, 133–143 (2009).
7. Combes, C. & Rey, C. Amorphous calcium phosphates: synthesis, properties and uses in biomaterials. *Acta Biomater.* **6**, 3362–78 (2010).
8. Grynopas, M. D. & Omelon, S. Transient precursor strategy or very small biological apatite crystals? *Bone* **41**, 162–4 (2007).

9. Gower, L. B. Biomimetic Model Systems for Investigating the Amorphous Precursor Pathway and Its Role in Biomineralization. *Chem. Rev.* **108**, 4551–4627 (2008).
10. Pazit Bar-Yosef Ofir, Ruti Govrin-Lippman, Nissim Garti, and H. F.-M. The Influence of Polyelectrolytes on the Formation and Phase Transformation of Amorphous Calcium Phosphate. *Cryst. Growth Des.* **4**, 177–183 (2004).
11. Sikirić, M. D. & Füredi-Milhofer, H. The influence of surface active molecules on the crystallization of biominerals in solution. *Adv. Colloid Interface Sci.* **128-130**, 135–158 (2006).
12. Bleek, K. & Taubert, A. New developments in polymer-controlled, bioinspired calcium phosphate mineralization from aqueous solution. *Acta Biomater.* **9**, 6283–321 (2013).
13. Song, R.-Q. & Cölfen, H. Additive controlled crystallization. *CrystEngComm* **13**, 1249–1276 (2011).
14. Fowler, C. E., Li, M., Mann, S. & Margolis, H. C. Influence of surfactant assembly on the formation of calcium phosphate materials—A model for dental enamel formation. *J. Mater. Chem.* **15**, 3317–3325 (2005).
15. Song, R., Co, H., Xu, A. & Antonietti, M. Polyelectrolyte-Directed Nanoparticle Aggregation: Systematic Morphogenesis of Calcium Carbonate by Nonclassical Crystallization. *ACS Nano* **3**, 1966–1978 (2009).
16. Block, D., Cölfen, H. & Qi, L. A systematic examination of the morphogenesis of calcium carbonate in the presence of a double-hydrophilic block copolymer. *Chem. Eur. J.* **7**, 106–116 (2001).
17. Qi, L. *et al.* Formation of BaSO₄ Fibres with Morphological Complexity in Aqueous Polymer Solutions. *Chem. Eur. J.* **7**, 3526–3532 (2001).
18. Xu, A.-W., Ma, Y. & Cölfen, H. Biomimetic mineralization. *J. Mater. Chem.* **17**, 415 (2007).

19. Antonietti, M. *et al.* Inorganic/Organic Mesostructures with Complex Architectures: Precipitation of Calcium Phosphate in the Presence of Double-Hydrophilic Block Copolymers. *Chme. Eur. j.* **4**, 2493–2500 (1998).
20. Tjandra, W., Yao, J., Ravi, P., Tam, K. C. & Alamsjah, A. Nanotemplating of Calcium Phosphate Using a Double-Hydrophilic Block Copolymer. *Chem. Mater.* **17**, 4865–4872 (2005).
21. Peytcheva, A., Cölfen, H., Schnablegger, H. & Antonietti, M. Calcium phosphate colloids with hierarchical structure controlled by polyaspartates. *Colloid Polym. Sci.* **280**, 218–227 (2002).
22. Landi, E. *et al.* Biomimetic Mg-substituted hydroxyapatite: from synthesis to in vivo behaviour. *J. Mater. Sci. Mater. Med.* **19**, 239–47 (2008).
23. Boanini, E., Gazzano, M. & Bigi, a. Ionic substitutions in calcium phosphates synthesized at low temperature. *Acta Biomater.* **6**, 1882–94 (2010).
24. Landi, E. *et al.* Biomimetic Mg- and Mg,CO₃-substituted hydroxyapatites: synthesis characterization and in vitro behaviour. *J. Eur. Ceram. Soc.* **26**, 2593–2601 (2006).
25. Abbona, F., Baronnet, A., Calabria, U. & Cs, R. A XRD and TEM study on the transformation of amorphous calcium phosphate in the presence of magnesium. **165**, 98–105 (1996).
26. Kibalczyk, W., Christoffersen, J., Christoffersen, M. R., Zielenkiewicz, a. & Zielenkiewicz, W. The effect of magnesium ions on the precipitation of calcium phosphates. *J. Cryst. Growth* **106**, 355–366 (1990).
27. Root, M. J. Inhibition of the amorphous calcium phosphate phase transformation reaction by polyphosphates and metal ions. *Calcif. Tissue Int.* **47**, 112–116 (1990).
28. Yang, X. *et al.* Influence of magnesium ions and amino acids on the nucleation and growth of hydroxyapatite. *CrystEngComm* **13**, 1153–1158 (2011).

29. Browning, N. D. *et al.* Scanning Transmission Electron Microscopy: An Experimental Tool For Atomic Scale Interface Science. *Rev. Adv. Mat. Sci.* **1**, 1–26 (2000).
30. Srot, V. *et al.* Microstructure, chemistry, and electronic structure of natural hybrid composites in abalone shell. *Micron* **48**, 54–64 (2013).
31. Egerton, R. F. Electron energy-loss spectroscopy in the TEM. *Reports Prog. Phys.* **72**, 016502 (2009).
32. Subramanian, S., Clark, G., Ly, K. & Chrasticky, T. Energy-Filtered Transmission Electron Microscopy (EFTEM) of Semiconductor Devices. *Electron. Device Fail. Anal.* **1**, 20–28 (2011).
33. Gower, L. B. Biomimetic model systems for investigating the amorphous precursor pathway and its role in biomineralization. *Chem. Rev.* **108**, 4551–627 (2008).
34. Mann, S. The Chemistry of Form. *Angew. Chem., Int. Ed.* **39**, 3392–3406 (2000).
35. Yu, S., Antonietti, M. & Co, H. Growth and Self-Assembly of BaCrO₄ and BaSO₄ Nanofibers toward Hierarchical and Repetitive Superstructures by Polymer-Controlled Mineralization Reactions. *Nano Lett.* **3**, 379–382 (2003).
36. Liou, S.-C., Chen, S.-Y. & Liu, D.-M. Manipulation of nanoneedle and nanosphere apatite/poly(acrylic acid) nanocomposites. *J. Biomed. Mater. Res. B. Appl. Biomater.* **73**, 117–22 (2005).
37. Wang, T. & Co, H. In Situ Investigation of Complex BaSO₄ Fiber Generation in the Presence of Sodium Polyacrylate . 1 . Kinetics and Solution Analysis. *Langmuir* **22**, 8975–8985 (2006).
38. Bigi, A., Boanini, E., Gazzano, M., Kojdecki, M. a. & Rubini, K. Microstructural investigation of hydroxyapatite-polyelectrolyte composites. *J. Mater. Chem.* **14**, 274–279 (2004).

39. Bigi, A., Boanini, E., Walsh, D. & Mann, S. Morphosynthesis of Octacalcium Phosphate Hollow Microspheres by Polyelectrolyte-Mediated Crystallization. *Angew. Chem. Int. Ed.* **41**, 2163–2166 (2002).
40. Adamczyk, Z., Bratek, A., Jachimska, B., Jasin, T. & Warszyn, P. Structure of Poly (acrylic acid) in Electrolyte Solutions Determined from Simulations and Viscosity Measurements. 22426–22435 (2006).
41. Jachimska, B., Jasiński, T., Warszyński, P. & Adamczyk, Z. Conformations of poly(allylamine hydrochloride) in electrolyte solutions: Experimental measurements and theoretical modeling. *Colloids Surfaces A Physicochem. Eng. Asp.* **355**, 7–15 (2010).
42. Kübel, C., Voigt, A., Schoenmakers, R., Otten, M. & Su, D. Recent Advances in Electron Tomography: TEM and HAADF-STEM Tomography for Materials Science and Semiconductor Applications. *Microsc. Microanal.* **11**, 378–400 (2005).
43. Friedrich, H., McCartney, M. R. & Buseck, P. R. Comparison of intensity distributions in tomograms from BF TEM, ADF STEM, HAADF STEM, and calculated tilt series. *Ultramicroscopy* **106**, 18–27 (2005).
44. Junginger, M., Kübel, C., Schacher, F. H., Müller, A. H. E. & Taubert, A. Crystal structure and chemical composition of biomimetic calcium phosphate nanofibers. *RSC Adv.* **3**, 11301 (2013).
45. Hitchcock, A. P., Dynes, J. J., Johansson, G., Wang, J. & Botton, G. Comparison of NEXAFS microscopy and TEM-EELS for studies of soft matter. *Micron* **39**, 741–748 (2008).
46. Srivastava, D. P. *et al.* Transformation mechanism of amorphous calcium carbonate into calcite in the sea urchin larval spicule. *PNAS* **105**, 17362–17366 (2008).

47. Feenstra, T., Hop, J. & De Bruyn, P. The influence of small amounts of magnesium on the formation of calcium phosphates in moderately supersaturated solutions. *J. Colloid Interface Sci.* **83**, 583–588 (1981).
48. Rokidi, S. & Koutsoukos, P. G. Crystal growth of calcium phosphates from aqueous solutions in the presence of strontium. *Chem. Eng. Sci.* **77**, 157–164 (2012).

Chapter 6

General Conclusions and Future Directions

6.1 General conclusions

In **Chapters 3** and **4**, the effect of various ion-doped hydroxyapatite (HA) nanoparticles (NPs) on cells behavior was evaluated. As shown, Mg-doped HA NPs induced osteosarcoma (MG63) cells death but did not affect viability of rat mesenchymal stem cells (rMSCs); Zn-doped HA NPs stimulated the proliferation of MG63 cells. All these findings are foreseen to have great potential in the design of new NPs with improved biological performance for biomedical purposes. In **Chapter 5**, neuron-like structure was created using simple organic molecules during calcium phosphate (CaP) precipitation and the co-effect of organic molecules with foreign ions on CaP precipitation were also investigated. These studies could be useful not only for the design of novel CaP/organic hybrids but also for a further understanding of biomineralization process in nature. The general conclusions for each chapter of the thesis are presented in below.

Mg and carbonate ion doping in HA NPs

1. As-synthesized HA and ion-doped HA NPs were phase pure and no secondary phase was present. Needle-like morphology was retained for Mg-doped HA NPs, while CO₃ ion-doped NPs presented more rounded morphologies with smaller aspect ratios. Solubility of doped samples increased with the addition of Mg and CO₃, due to their lower crystallinity.

2. Well-dispersed NPs suspensions were obtained by absorption of sodium citrate onto nanoparticles which provided NPs with negative surface charge. The dispersion was stable for a long time even at ambient temperature. In addition, serum adsorption resulted in negatively charged NPs protein.
3. All ion-doped NPs did not alter viability of both MG63 cells when NPs had negative surface charge which conferred by citrate molecules or serum adsorption. Once citrate and serum were removed from NPs, Mg in the NPs (>1.5 wt%) led to a marked cytotoxicity on MG63 cells, but did not have any major effect on the viability of rMSCs.
4. Negative surface charge of NPs provided by citrate molecules and/or serum adsorption could prevent cellular uptake of NPs by MG63 cells as increasing 10M NPs dose in cell culture medium in the presence of citrate and serum did not induce any cytotoxicity. However, this is not critical for rMSCs since the increase in NPs' dose decreased the viability of rMSCs cells under the same conditions.

Sr, Zn, Si and Fe ion doping in HA NPs

1. As-synthesized ion-doped HA NPs were phase pure. Ion doping had little influence on the morphology of NPs as in all cases needle-like structure was remained, but it had significant impact on the crystallinity of NPs. Sr ions were incorporated into the lattice of HA crystals by substituting Ca sites, however, only parts of Zn ions were incorporated into lattice of HA crystal and all Fe ions seemed to be just absorbed on crystal surface. The solubility of Sr-doped and Si-doped HA NPs increased, while Zn-doped and Fe-doped HA had a decreased solubility with ions addition.
2. Zn and Fe-doped HA NPs stimulated MG63 cells proliferation when FBS was not supplemented to culture medium. Zn-doped HA NPs stimulated the proliferation of MG63 cells in a time-dependent manner, but MG63 cell growth were inhibited by NPs at high doses (>250 µg/mL) under the

condition of serum-free. Cell viability was retained in MG63 cells under the condition of serum-containing by NPs. Zn-doped HA NPs with low NPs doses (<250 $\mu\text{g}/\text{ml}$) also enhanced the proliferation of rMSCs even in the presence of serum.

3. Only when cells became exposed directly to the 10Zn NPs higher proliferation was induced. The ions released in the cell culture medium from 10Zn NPs did not promote MG63 proliferation and, to achieve the stimulated proliferation for MG63 cells, 10Zn NPs has to interact directly with cells.

The effect of organic molecules and ions in CaP precipitation

1. Surfactants (Tween 80), anionic polymers (sodium polyacrylate) and cationic polymers (polydiallyldimethylammonium chloride) created neuron-like structures in CaP solution. The reaction conditions were critical in stabilizing this particular type of structure and determined the purity of the product. Within the range of conditions investigated, only with the addition of sodium polyacrylate and under specific conditions (pH=3), the neuron-like structure could be obtained practically pure. In all other cases, the formation of these structures competed with the precipitation of CaP crystals.
2. The neuron-like structures were formed by the deposition of calcium phosphate and according to TEM analysis they were indeed amorphous phase. EFTEM imaging showed that calcium, phosphorous and oxygen elements were distributed throughout the dense core as well as the filaments of the neuron-like structures.
3. Foreign inorganic ions also played important roles in the formation of neuron-like structure as proved by preliminary TEM investigation. The incorporation of Mg ions destabilizes neuron-like structure while Sr ions did not affect their formation and stability in the solution.

6.2 Future directions

The results obtained in **Chapters 3** and **4** are promising in the field of biomedicine as Mg-doped HA NPs have selective cytotoxic effect on cancer cells and Zn-doped HA NPs stimulated cell proliferation. In **Chapter 5**, neuron-like CaP structures were created using organic molecules, but the mechanisms of formation is still unclear to us. In order to increase the potential of ion-doped HA NPs as carriers for gene delivery and further understand the CaP mineralization in the presence of organic molecules, studies should be performed in the following directions in near future.

1. Since Mg-doped HA NPs had selective cytotoxicity on osteosarcoma MG63 cells (non-cytotoxicity to rMSCs), they could be introduced as anti-cancer “drugs” in cancer therapy. As only one type of cancer cells (MG63) were tried in our present work, to gain more information of using Mg-doped HA NPs to treat cancer, more types of cancer cells should be introduced for *in vitro* experiments.
2. The effectiveness of using ion-doped HA NPs to deliver genetic materials into cells as well as the transfection efficiency in various types of cells *in vitro* should be evaluated as well. This direction would first require investigation of the loading capacity and quality of the genetic material (plasmid DNA) onto the NPs. In this direction Zn-doped HA NPs should attract much more attention than other ion-doped HA NPs not only because of its non-cytotoxicity but also they stimulated cell proliferation so as to help gene replication.
3. HA NPs has tendency to agglomerate, representing a major problem associated with the conduct of delivering gene to cells *in vitro* or *in vivo*. Thus, stable colloids of HA NPs should be prepared. In our case, the positively charged polymers should be employed to disperse NPs and create stable NPs suspensions for gene delivery as the positive surface charge can improve the

affinity of negatively charged DNA molecules on NPs due to the electrostatic attraction.

4. Regarding the neuron-like CaP structures, they should be separated from aqueous solution using filter devices or ultracentrifugation methods for us to submit them to other analytical techniques such as XRD and FTIR. This could help us to gain more insights about their physicochemical properties and the mechanisms by which neuron-like structure formed.
5. More organic molecules should be introduced in the CaP precipitation system to investigate if this neuron-like structure can be created as a common intermediate for the biomineralization and biomimetic mineralization.